SEMICONDUCTOR NANOSTRUCTURES AND NANOASSEMBLIES: A NEW PERSPECTIVE ON THEIR SYNTHESES, PROPERTIES AND PHOTOPHYSICAL BEHAVIOR

A thesis submitted to the University of East Anglia in partial fulfillment
of the requirements for the degree of DOCTOR OF PHILOSOPHY

University of East Anglia

By

CHIRANJIB BANERJEE

School Of Chemistry

University Of East Anglia

Norwich, UK NR4 7TJ

-- JANUARY 2013 --

STATEMENT OF ORIGINAL WORK

Declaration

I, hereby declare that, the work described in this thesis has been carried out by myself, and to the best of my knowledge, is original. Where other people's work has been referred to, those have been cited by corresponding references. This thesis has not previously been submitted for any degree at this or any other university.

Chiranjib Banerjee

Signed: -------------------------------

(Chiranjib Banerjee)

Dated: January 22nd, 2013.

ABSTRACT

In the first part of this research, attempts have been made to use single-molecule precursors $[X_2In(\mu\text{-}PR_2)]_2$ (X = Me, CH_2Ph; R = CMe_3, $SiMe_3$) to generate nano-dimensional InP through thermal degradation. Thermolysis of the di-tert-butyl precursors always led to In^0, whereas, the trimethylsilyl precursors formed In^0 only in presence of hexadecylamine, but in the absence of the amine could form InP nanoparticles. Thermolysis of $[(PhCH_2)_2InP(SiMe_3)_2]_2$, a new precursor, gives either InP nanoparticles or nanowires, depending on the presence or absence of stearic acid. This provided a simple and rapid method for the synthesis of InP nanowires, for the first time, without the need of any protic co-reagents or surfactants. The wires were grown using the *hot injection technique* and their formation relies on the *SLS* mechanism. We also showed for the first time that the lengths of the nanowires can be conveniently controlled by adjusting only the injection temperature and were able to grow wires at a temperature as low as 160 °C. Finally, the indium metal at the base of each wire, an obvious outcome of the SLS mechanism, can be easily removed under mild non-corrosive conditions.

The second part of the thesis describes attempts to couple group II-VI (CdSe, ZnSe) quantum dots with subphthalocyanines (SubPcs) to form hybrid nanoassemblies. The SubPcs chosen, carried pendant pyridyl moieties for coordination to the nanoparticle surfaces. However, ZnSe did not show any ligand binding, whereas, CdSe formed a stable complex, with an association constant either larger than or comparable to previously reported values for other macrocycles. The QD : ligand ratio was determined by a number of independent experimental methods (UV, PL, NMR spectroscopy, quenching studies). The CdSe-SubPc formed an efficient donor-acceptor system in terms of photophysical properties, and energy flow within such systems was found to occur primarily through FRET mechanism.

ACKNOWLEDGEMENTS

It is a great pleasure for me to get this opportunity to express my sincere gratitude and appreciation to all those people, for whom a successful completion of this PhD degree is possible.

I am grateful to my supervisor, Prof. Manfred Bochmann, for his guidance, patience, encouragement and support during my time at UEA. My sincere gratitude also goes to my other supervisory committee members Prof. Thomas Nann, Prof. Andy Cammidge and Dr. Yimin Chao. My co-supervisor Prof. Nann provided the necessary nanoscience expertise while at UEA but after year 1 of my PhD project, moved to Australia. He taught me how to handle nanomaterials, different instrumental techniques and most importantly laid the foundation knowledge about nanoscience in me. I would also like to thank Prof. Nann for recording the XRD and HRTEM data of my samples in Australia. After Prof. Nann’s departure, Prof. Andy Cammidge and Dr. Yimin Chao helped continuously with my research work. Prof. Cammidge’s involvement was truly indispensable at that stage. He kindly provided me with the necessary SubPc compound and routinely checked my every experimental result, followed by his valuable comments and suggestions. I thank Dr. Chao for his advice and providing me with instrumental facilities and for unrestricted access to his lab.

I would also like to extend my thanks to other members of the department, especially, Dr. Andrew Mayes, Dr. Greg Wildgoose and Prof. David Russell for letting me use the instrumental facilities in their lab and frequent discussions on my research. My sincere acknowledgement also goes to Dr. David Hughes for recording single crystal X-ray data for me, Dr. Colin Mcdonald for helping me with TEM instrumentation.

I do hereby thank the UK government for providing me with the ORSAS award, UEA for the International Student Fellowship (ISF) award and the Department of Chemistry for the PhD studentship and Novartis award.

I would also like to express my heartfelt thanks to all my colleagues and friends Leo, Maria, Girgis, Paul, Nicky, Dragos, Anu, Chrisa, Abdi, Jayashree and many others for their time-to-time cooperation and for making my days at Norwich enjoyable. I want to specially thank Chrisa for providing her immense help in submitting this thesis, while I was in India and for being such a wonderful friend of mine always.

Last but not the least, my special thanks go to my dear parents and my wife, Prof. Oindrila Banerjee for their constant emotional support, a lot of sacrifice, encouragement and love to fulfill all my dreams and ambitions. Within one month of our wedding, I had to leave Oindrila back in India for more than a year and come back to England to continue my research. It was her great sacrifice and patience she showed during this period, without a single complaint but a smile on her face always.

My due regards, gratitude and thanks again to all of you for all the love and blessings you have given me and have shown tolerance to all my faults and short-comings.

TABLE OF CONTENTS

CHAPTER 2 THERMAL DEGRADATION OF PHOSPHIDO BASED SINGLE MOLECULE PRECURSORS TO FORM INDIUM PHOSPHIDE NANOSTRUCTURES

CHAPTER 3 SYNTHESES & CHARACTERIZATIONS OF II-VI SEMICONDUCTOR QUANTUM DOTS

CHAPTER 4 QUANTUM DOTS MEET SUBPHTHALOCYANINES: A SYSTEMATIC STUDY OF THE FORMATION OF AND ENERGY FLOW IN II-VI HYBRID NANOASSEMBLIES

CHAPTER 5 SIGNIFICANCE AND FUTURE SCOPE OF THE CURRENT RESEARCH: A CRITICAL ANALYSIS

LIST OF FIGURES

CHAPTER 1

CHAPTER 2

CHAPTER 3

CHAPTER 4

LIST OF SCHEMES

CHAPTER 2

CHAPTER 3

CHAPTER 4

LIST OF TABLES

CHAPTER 1

CHAPTER 2

CHAPTER 3

CHAPTER 4

LIST OF ABBREVIATIONS

QD	Quantum dot
NP	Nanoparticle
NC	Nanocrystal
NW	Nanowire
nm	nanometer
ca.	circa
et al.	et alii
e.g.	For example
i.e.	*it est* (that is)
etc.	*et cetera*
a.u.	Arbitrary units
w.r.t.	With respect to
No.	Number
h	hours
min	minutes
s	seconds
mol	moles
M	molarity
m	milli
L	Litre

g	gram
b.p.	Boiling point
m.p.	Melting point
tert.	Tertiary
ppm	Parts per million
HOMO	Highest occupied molecular orbital
LUMO	Lowest unoccupied molecular orbital
FWHM	Full Width at Half Maximum
FRET	Fluorescence (or Főrster) resonance energy transfer
TMS	Trimethylsilyl
TBP	Tri-n-butylphosphine
TOP	Tri-n-octylphosphine
TOPO	Tri-n-octylphosphine oxide
OA	Oleylamine
ODE	1-Octadecene
MeMy	Methyl myristate
SubPc	Subphthalocyanine
UsubPc	Unsubstituted subphthalocyanine
SLS	Solution-liquid-solid
ZnU	Zinc undecenoate
SA	Stearic acid
HDA	Hexadecylamine

DPE	Diphenyl ether
Me	Methyl
Bu	Butyl
OQD	Orange quantum dot
GQD	Green quantum dot
EDX	Energy Dispersive X-ray
UV-Vis	Ultraviolet-visible
PL	Photoluminescence
IR	Infrared
NMR	Nuclear Magnetic Resonance
SAED	Selected area electron diffraction
TEM	Transmission Electron Microscopy
HRTEM	High Resolution Transmission Electron Microscopy
XRD	X-ray diffraction

This Thesis is Dedicated to

My Parents

&

My Wife, Oindrila

CHAPTER 1 AN INTRODUCTION TO THE SCIENCE AND TECHNOLOGY OF SEMICONDUCTOR NANOMATERIALS

1.1 PREAMBLE

More than half a century ago (Dec' 1959), in his ground-breaking lecture, *There's Plenty of Room at the Bottom*, eminent physicist and Nobel laureate Richard Feynman was the first person to lay the foundation of modern day Nanoscience. He talked about the physical possibilities for 'making, manipulating, visualizing and controlling things on a small scale,' and imagining that, in decades to come, it might be possible to arrange atoms 'the way we want'.[1,2] The term *Nanotechnology* (Greek *Nanos* = dwarf) was then first coined in 1974 by Professor Norio Taniguchi at the University of Tokyo, Japan, to refer to the ability to engineer materials precisely at the nanometer level, driven by electronics industry needs.[3,4]

By the US National Nanotechnology Initiative (NNI) standards, nanotechnology involves research and technology development at the atomic, molecular or macromolecular levels, approximately 1-100 nm length.[4] The Royal Society and the Royal Academia of Engineering define nanotechnology as the design, characterization, production and application of structures, devices and systems by controlling shape and size at the nanometer scale.[5]

The field of nanoscience might initially appear to be a specialized field, but in reality it is the opposite. It involves the contributions and expertise of people from a vast number of areas, such as chemistry, physics, biology, materials science, engineering and so forth. Gary Stix, senior editor of Scientific American, described nanotechnology as "the field is a vast grab bag of stuff that has to do with creating tiny things and it borrows liberally from condensed-matter physics, engineering, molecular biology and large swaths of chemistry".[6] This in true sense is an interdisciplinary science, having a wide range of applications from photodynamic therapy to electronic devices.

Nano-sized materials in the form of dots or particles, rods, wires, pillars, flowers and other novel structures have been synthesized out of metals or non-metals or semiconductor materials. Among them the semiconductor nanomaterials are an important subset, due to their unique size-dependent opto-electronic properties and various applications. This thesis also involves the syntheses, characterizations, ligand binding chemistry and energy transfer mechanism of Group III-V (InP) and Group II-VI (ZnSe, CdSe) semiconductor materials. The organization of this dissertation is discussed in the last section of the current chapter.

1.2 ELECTRONIC BAND STRUCTURE OF MATTER AND QUANTUM CONFINEMENT EFFECT

In bulk solids, the electrons fill in the molecular orbitals (MO), starting from the one with lowest energy (closest to the nucleus) and the set of these filled orbitals is collectively called the valence band. Immediate to this valence band, there lies another set of molecular orbitals, which are higher in energy than the valence band and are devoid of electrons. This vacant band of energy levels is known as the conduction band. The energy gap between the valence band and the conduction band is referred to as the band gap. The metals or the conductors have a full valence band and a conduction band partially filled with electrons. The electrons in the conduction bands are mobile and delocalized over the entire metal lattice, which make the metals good conductors of electricity. By contrast, insulators have completely filled valence bands and the band gap is so wide that the electrons cannot be promoted to the conduction band at room temperature. The electrons in an insulator are thus immobile and localized. A semiconductor has a full valence band and an empty conduction band, but the band gap in a semiconductor is sufficiently narrow to allow excited electrons to be promoted from the valence into the conduction band. When the physical size of the materials decreases from the bulk to nano dimension, the electronic structure also changes and approaches that of an isolated atom/molecule. The continuous band structure becomes discrete and the band gap energy (E_g) increases with decreasing size of the nanocrystal (Figure 1.1).[7]

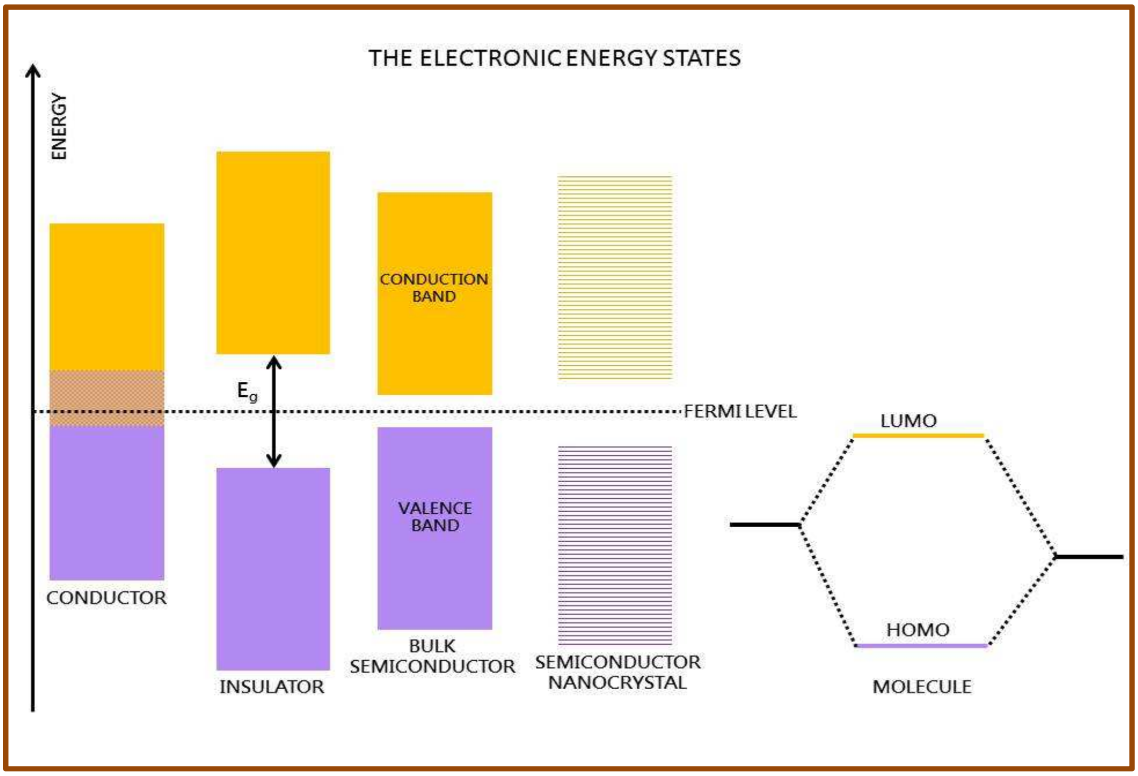

Figure 1.1. The energy states and the band gap diagram.

When an electron is excited from the valence band to the conduction band, it leaves a hole in the valence band and forms an electrostatically bound state of electron-hole pair, which is called an *exciton*. The exciton has a finite size within the crystal lattice defined by the Bohr exciton radius (a_B). If the size of a nanocrystal is less than this Bohr exciton radius, the charge carriers become spatially confined and this crowding leads to the splitting of the original energy bands further to form closely spaced discrete energy levels, a phenomenon called the *quantum confinement effect* and the nanocrystals are said to be in a strong confinement regime. Nanocrystals, that exhibit such quantum confinement effects, are popularly known as quantum dots. Due to this quantum confinement effect, the electronic and optical properties of quantum dots depend greatly on their size and vary significantly from their bulk size. With decreasing size of the nanocrystals, the band gap energy increases leading to an absorption or emission toward the blue end of the spectrum.

The band gap depends both on size and substance. It also varies with the shape of the crystal and nature of doping with a dopant molecule. Furthermore, quantum confinement can be along three-dimensional (quantum dots), two-dimensional (quantum wires) or one-dimensional (quantum wells), which are also known as zero-, one- and two-dimensional potential wells, respectively.

1.3 THEORIES OF NUCLEATION AND CRYSTAL GROWTH

The solution phase synthesis of nanocrystals undergoes two stages viz. *nucleation* and *growth* that determine the size and shape of the nanocrystals.[8] The first stage is the nucleation step, where a tiny nucleus or seed is either formed *in situ* (homogeneous nucleation) or externally supplied (heterogeneous nucleation). Since nucleation influences the size distribution of the final nanocrystals, a short and a very rapid sudden burst of nucleation phase, which is well separated from the growth phase, is always desirable. If the nucleation and the growth phase overlap with each other, then differently sized particles are formed, resulting in a broad distribution of size. Typically, a short sudden burst of nucleation is triggered by using active precursors and starting the reaction at a high temperature. The precursors either react with other co-reactants or are thermolyzed (in the case of single molecule precursors) at high temperature generating monomers of the nanocrystals. Nucleation is initiated when the monomers are supersaturated and the temperature is high enough to overcome the activation barrier of nucleation. To separate the growth phase from the nucleation phase, typically the particles are allowed to grow at a lower temperature.

According to the classical theory of nucleation, the growth or dissolution of a nucleus depends on its size, but the process which it undergoes should result in the decrease in the free energy of the particle.[8] When a nucleus of radius r, is formed from the homogeneous solution, the change in the free energy, ΔG is given by –

$$\Delta G = \Delta G_S + \Delta G_V$$

$$= 4\pi r^2\gamma + (4/3)\pi r^3\Delta G_v \ldots\ldots\ldots\ldots(1.1)$$

where, ΔG_S is the surface excess free energy and ΔG_V is the volume excess free energy;[8] γ is the surface free energy per unit area, and ΔG_v is the free energy per unit volume of crystal.[9] ΔG_v can be further expressed as the difference between the free energy of the monomer in crystal and solution and is given by[9,10] –

$$\Delta G_v = - (RT \ln S)/ V_m \ldots\ldots\ldots\ldots(1.2),$$

where, V_m is the molar volume of the monomer in crystal and S is the supersaturation and is the driving force for both the nucleation and the growth process.

In a homogeneous solution, nucleation is accompanied by the formation of an interface between the crystal and the solution, resulting in the increase in free energy, and the first term in the equation 1.1 is positive. On the other hand, the monomer in the crystal has a smaller free energy than that in solution for a supersaturated solution (S>1), i.e. a decrease in free energy occurs due to crystal formation, making the second term of equation 1.1 negative for S>1. Due to these two opposite sign terms, ΔG passes through a maximum. This maximum value, ΔG_{crit} (setting d ΔG/dr =0), corresponds to the critical nucleus r_c,

$$r_c = -2\gamma/\Delta G_v \text{..................} (1.3)$$

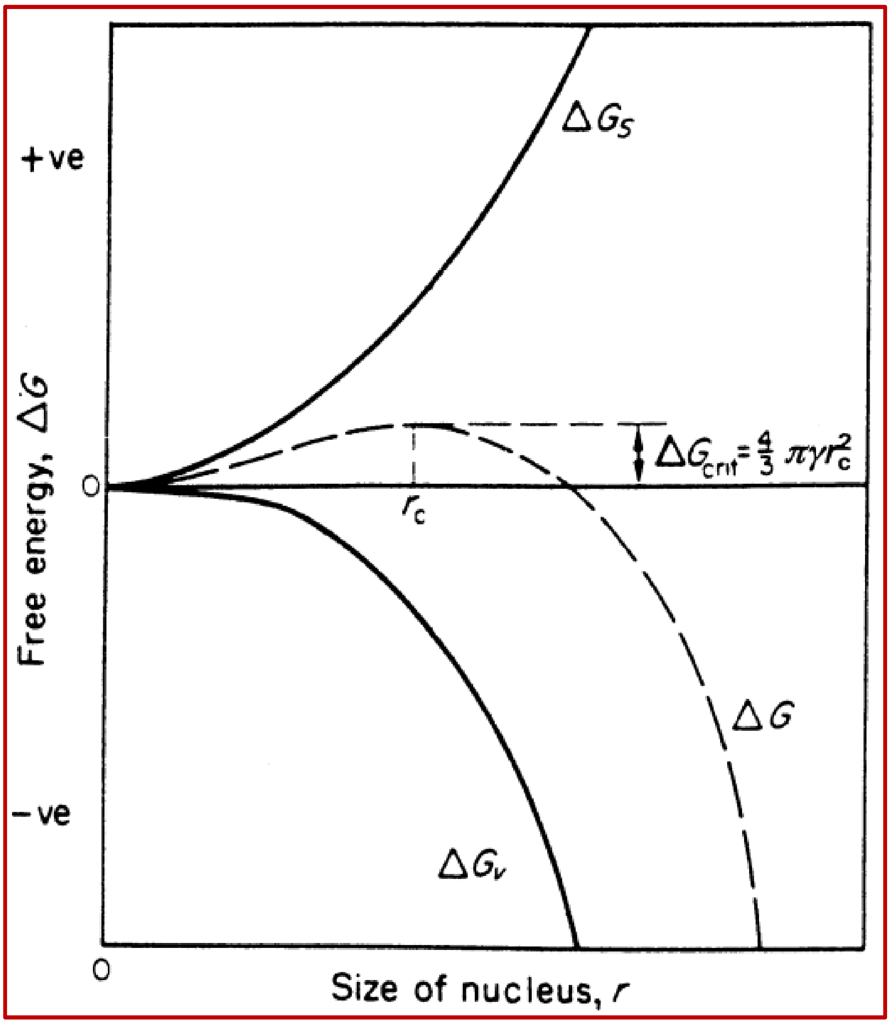

Figure 1.2. Free energy diagram for nucleation.[8]

Putting the value of ΔG_v from equation 1.2 into equation 1.3, we get

$$r_c = 2\gamma V_m / (RT \ln S)………(1.4)$$

From equation 1.1 and 1.3, we get, $\Delta G_{crit} = (4/3)\ \pi\gamma r_c^2$.

Figure 1.2 shows the diagram of free energy change of the nucleation process. From the figure, it can be said that when $r < r_c$, the only direction in which the free energy is decreased is toward the left, i.e. smaller value of r. As a result, any nucleus smaller than r_c, would spontaneously dissolve. Similarly, any nucleus larger than the r_c, would grow. The critical radius, therefore, represents the minimum size of a nucleus that is stable.

The next stage is the crystal growth phase. This is a slow and continuous process, which consumes the remaining reagents after the nucleation stage to form stable crystals. The crystal growth rate depends on temperature; faster growth is achieved at a higher temperature and the growth can be stopped by lowering the temperature sufficiently. The growth process occurs through two processes – (i) the diffusion of monomers from the bulk solution on to the crystal surface through a stagnant boundary layer, (ii) reaction of monomers on the surface i.e. incorporation of the adsorbed monomers into the crystal lattice. When the surface reaction is very fast, the growth process becomes diffusion controlled. At a fixed monomer concentration, assuming diffusion is the rate limiting step, the size dependent growth rate of nanostructures can be obtained by considering the Gibbs-Thomson equation:[11,12]

$$S_r = S_b \exp\left(\frac{2\sigma V_m}{rRT}\right)\text{, where,}$$

S_r and S_b are the solubilities of the nanocrystal and the corresponding bulk solid, σ is specific surface energy, r is the radius of the nanocrystal, V_m is the molar volume of the material, R is the gas constant and T is the temperature.

If, $\left(\frac{2\sigma V_m}{rRT}\right) << 1$, the diffusion controlled growth rate of the particle with radius r is:

$$dr/dt = K\,(1/r + 1/\delta)\,(1/r^* + 1/r)\text{, where,}$$

K is a constant proportional to the diffusion constant of the monomer, δ is the thickness of the diffusion layer. At a fixed concentration, r* is the critical radius for which the solubility of the nanocrystal is exactly the concentration of the monomers in solution (zero growth rate).

In Figure 1.3, the critical radius r* is the point at (1,0). Nanocrystals smaller than this r* has a negative growth rate, i.e. dissolves, while larger ones grow at a rate, strongly dependent on the size. The mass transport process allows the smaller particles to grow faster than larger ones, while

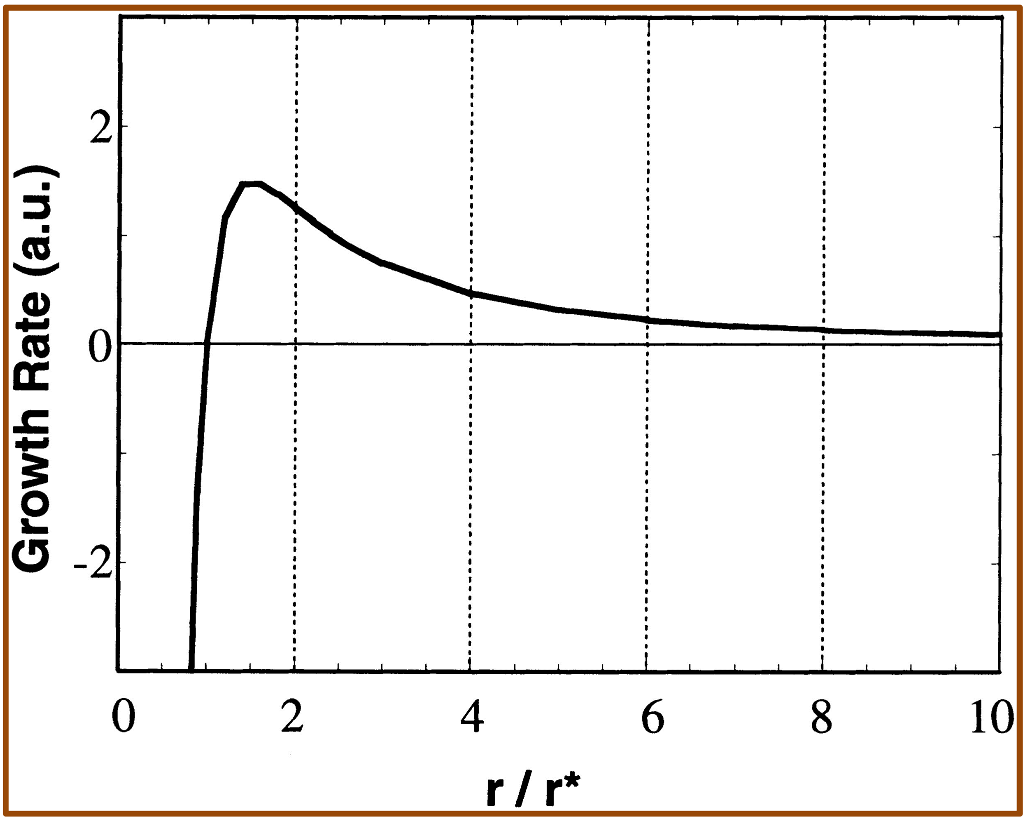

Figure 1.3. Variation of growth rate versus size, according to the model of Sugimoto.[11]

according to Gibbs-Thomson effect, smaller particles tends to dissolve rather than grow, because they are thermodynamically more unstable (have larger chemical potential value) than the larger particles. These two opposite effects make the growth curve have a maximum value.

At sizes below r*, the Gibbs-Thomson effect becomes overwhelming, and the sizes are too unstable to grow. At sizes larger than r*, the mass transport process becomes important and the crystals start growing. The smaller crystals grow faster than the larger ones. The chemical potential becomes smaller and the activation barrier of precipitation is lower than the barrier for dissolution. Since the smaller particles grow faster than the larger ones, they all tend to be of the same final size, a process called *focusing of size*. The growth curve at the focusing region is mainly in the steep negative portion (left side) of Figure 1.3. This size focusing can only occur when the growth process is diffusion controlled and a high supersaturation is the necessary driving force for such a process. However, due to the precipitation of the crystals, the monomer concentration gets exhausted and the growth mode is no longer in the diffusion-controlled regime. The supersaturation decreases, the critical radius increases and is larger than the average size of the particles actually present. This is the slow positive growth rate (right side) of Figure 1.3. Broadening of size distribution starts to occur at this point. The smaller crystals start to dissolve and the larger ones continue to grow. This is known as *Ostwald ripening* or *defocusing*. This distribution can be refocused by injection of additional monomer at the growth temperature, which shifts the critical size back to a smaller value. Size focusing lasts for a short period. Ripening is a slow process compared to size focusing. Therefore, the size distribution remains narrowed for a while even after size focusing ends. Usually, the synthesis of nanocrystals is terminated at this point in time.[11–13] One additional point to mention is that size focusing requires absence of any nucleation process occurring during the growth phase. The continuous generation of new nuclei disturbs the focusing effect. This means that the sooner the nucleation period ends, the more beneficial it is for size focusing. Thus it is highly desirable to separate the nucleation and the growth phases.

1.4 SURFACE DEFECTS AND PASSIVATION

Since surface is the termination of a bulk crystal, the surface atoms have fewer neighbors than the bulk atoms and a part of the chemical bonds, which constitute the bulk, are broken at the surface. These broken bonds at the surface are called *dangling bonds* and are formed at the cost of energy, called surface energy. Due to high surface to volume ratio, most nanocrystals have very high surface energy and numerous dangling bonds at the surface.[14] A substantial amount of surface reconstruction occurs in the atomic positions, leading to defects and the appearance of new energy levels within the band gap of the nanocrystals, which are known as surface states. These surface states act as traps for electrons and holes and degrade the optical and electrical properties of the nanomaterials. To eliminate these surface states, the surface of the nanocrystals needs passivation. Passivation is achieved either by epitaxial overgrowth of another inorganic semiconductor material, with higher band gap (shell) over the nanoparticle to be passivated (core) or by chemically bonding an organic ligand (capping or surfactant molecule) onto the surface of the nanocrystal. In either case, the surface atoms can pair, or the dangling bonds are removed and the surface states are removed from the band gap. The nanocrystal surfaces are also protected from any potential oxidation and reduction through such a passivation.

The core/shell approach is a powerful method for surface passivation and provides stability of quantum dots toward oxidation and photo degradation. In this method, the nanocrystal of interest lies in the core and on the outside, it is covered with a higher band gap semiconductor material, forming the shell. The larger band gap shell helps to confine the electrons within the valence band and the conduction band. The shell material also has to have as minimal as possible, a lattice mismatch with the core particle. For example, $ZnCdSe_2$ has a lattice constant, which exactly matches with that of InP and the bulk band gap of $ZnCdSe_2$ (2.2 eV) is also higher than that of InP (1.35 eV). Thus $ZnCdSe_2$ is an ideal shell material for InP quantum dots.[15]

Organic ligands for surface passivation or surface capping, such as fatty acids[16] and fatty amines,[17] called surfactants, generally contain a donating group. These groups can bind to the surface through coordinate bonds and increase electron density on the nanoparticle’ s surface and force the excitons to remain confined within the valence band and the conduction band, instead of letting the electrons of the nanocrystals flow to the surface trap states, created by the dangling bonds. The surfactant molecules also play a role in controlling the growth of the nanocrystals, colloidal stabilization, avoiding aggregation of particles and solubility of the nanocrystals. The weak coordinating bond of the surfactants can further be utilized to exchange the surfactants with other ligands and for further derivatization of the surface of the nanoparticles.[18,19]

1.5 THE HOT INJECTION METHOD

Between the two synthetic techniques, viz. the *hot injection* and *heating up* methods, which utilize homogeneous nucleation for the solution phase syntheses of monodisperse nanocrystals, the hot injection technique is more widely used for the synthesis of metal pnictogenides,[16] metal chalcogenides,[20] transition metals[21] and noble metals.[22,23] The work in this thesis also utilizes this hot injection method, and this approach is thus discussed in detail.

In 1993, the Bawendi group published a seminal paper in which the hot injection technique for the synthesis of monodisperse cadmium chalcogenides was introduced.[24] This pioneering work was later extended to the syntheses of nanocrystals of various other materials. In this method, typically first an excess precursor solution is rapidly injected into a preheated solution of surfactant in the desired solvent, followed by a growth of the crystals at a temperature lower than the injection temperature.

Thermodynamically, nucleation and crystal growth from a given solution of monomers are both favored by lower temperatures since the solubility of most crystals increases rapidly at higher temperatures, lowering supersaturation (S) drastically. However, kinetically, nucleation needs to overcome an activation barrier for the formation of nuclei with size r_c, which is favored by higher temperatures. Specifically, high temperatures favor faster monomer diffusion, reduce r_c (equation 1.4) and ΔG_{crit}, and increase the probability for successful nucleation.[10] Hot injection synthesis optimizes particle formation by combining these effects. The high reaction temperature, the reactive precursors, and the rapid injection cooperatively render the reaction system highly supersaturated at the start. Injection of cool reagents into the hot solvent leads to initial nucleation due to the local high supersaturation. Soon after the injection of cool precursor solution, the reaction cools due to mixing and the solubility of the free monomer rapidly decreases, which keeps the supersaturation (S) high enough to maintain nucleation for a brief period. Hence the nucleation is initially aided by the fast temperature reduction. During the nucleation process, the monomer concentration in the solution sharply decreases and because the activation energy for the nucleation reaction is much higher than that for the precipitation reaction, the nucleation stops at a supersaturation level that is still high enough for the precipitation reaction to occur. Consequently, the system evolves spontaneously from the nucleation period to the growth period at a lower temperature. In the growth period, there is no nucleation and the supersaturation level is high, which are exactly the conditions required for size focusing.[9] A numerical simulation reported by Park *et al.* also successfully reproduced the hot injection technique.[25]

1.6 A COMPARATIVE ANALYSIS OF GROUP II-VI AND III-V QUANTUM DOTS

The II-VI and III-V quantum dots are perhaps the most widely studied nanoparticles so far. In our research InP (III-V) and ZnSe, CdSe (II-VI) based materials were studied. There are quite a few significant similarities and differences between the properties of these two classes of semiconductor, and this would be the ideal point to compare them in brief.

II–VI materials are closely related to the III–V semiconductors in many respects. Like the III–Vs, most II–VIs are direct band gap semiconductors. They are also characterized by tetrahedral bonding geometries (wurtzite or zinc blende crystal habits), and the chemical nature of the unit cell has both ionic and covalent bonding contributions. The II-VI compounds are more ionic than the III-Vs. Percent ionic character of a bond between elements A and B (A being more electronegative than B) can be estimated from the following equation:[26]

$$\%\ \text{ionic character} = \{1 - \exp[-(0.25)(X_A - X_B)^2]\} \times 100$$

where, X_A and X_B are the electronegativity of the respective elements.

Table 1.1. Electronegativity values of elements (Pauling Scale)[27]

Element	Electronegativity
Cd	1.69
Se	2.55
In	1.78
P	2.19

Using the electronegativity values based on the Pauling scale (Table 1.1), percent ionic character calculated from the above equation are as follows:

CdSe =16.88% and InP = 4.12%

Moreover, the II-VIs have much smaller exciton diameter (CdSe 56 Å)[28] than the III-V semiconductors (InP 216 Å).[29] The exciton diameter is the most important length scale in determining at what particle diameter, the finite size effect or the quantum confinement effect becomes significant. When the size of the crystallite lattice is decreased below the exciton diameter, the quantum confinement effects appear in the room temperature electronic and optical properties. Since the III-V group has a much larger exciton diameter, the finite size effects are more pronounced in them than the II-VI ones. As discussed in Section 1.3, for the formation of small nanoparticles with a narrow size distribution, the temporal separation of nucleation phase from the growth phase is absolutely necessary. It is required to keep the nucleation phase as short as possible. Although this is easy to visualize, it can sometimes be extremely difficult to put into practice. For the II-VI compounds, Bawendi' s group showed that by employing the hot injection technique, it was possible to temporally separate the nucleation and the growth phase, and a very narrow distribution of monodisperse nanocrystals can be achieved in the size range of ~1.2-11.5 nm.[24] The chemical nature of the II-VI compounds, which are more ionic, allows for such a reaction scheme. Bare atoms or ions are directly reacted with each other at a high temperature via rapid injection of one reagent into another. There is a short nucleation burst right after the injection. Sufficient volume is injected so that the temperature drops to a value, which is enough for the growth process, but stops the nucleation within seconds. In a successively more covalent series of materials, for example, the III-V quantum dots, it becomes increasingly difficult to separate the nucleation and growth processes. This is due both to the nature of the reagents used to make the particles, and to the nature of the particles themselves. For the III-V system, bare atoms and ions are not chemically stable species, so the synthesis of the nanocrystals must be carried out with strongly complexed precursors.[30] Therefore, the nucleation and growth for such materials are both high temperature processes and separation of the two is rather difficult. Moreover, the structure for these materials is crystalline, but with increasing covalent character in the materials, the amorphous phase becomes increasingly important and tends to form easily at lower temperatures. Therefore, high temperature is required for more covalent compounds (such as, III-V materials) to achieve crystallinity. Comparing between the II-VI and III-V (with higher covalent character) materials, say for example, CdSe (II-VI) and InP (III-V), it is possible to grow CdSe nanocrystals at room temperature[31,32] or as low as 90 ℃.[33] InP, on the other hand, requires temperature in the range of 250 ℃ or so,[34,35] and such temperature must be maintained sometimes for several days for annealing[36] to obtain high quality nanocrystals. Because of the high temperatures and long time required for producing the III–V compounds, it is not possible to obtain a narrow distribution from a single synthesis, and size sorting must be done after the completion of the synthesis.

The nature of surface-trapped states is also different in case of III-V and II-VI nanocrystals. Increased ionic bonding character within a bulk crystal leads to successively shallower trap states.[30] According to Luth,[14] in II-VI compounds, due to greater ionic character, the effects of surface reconstruction are only weak perturbations when compared to the strong ionic (Coulombic) forces, which dominate the bonding. The surface states, thus, remain very shallow for II-VI. The nature of the surface states can play a determining role in the observed photoluminescence efficiency at room temperature. The activation barriers for detrapping are determined largely by the depth of the surface states with respect to the conduction band. The band edge luminescence quantum yields will decrease exponentially with increasing depth of the surface state energy levels.[30] Due to greater covalent bonding in III-V quantum dots, the surface states are deep traps and consequently, the barriers for detrapping limits the PL quantum yield in III-V semiconductors.[37]

The growth and stability of the nanocrystals also depend on the lattice energy of the material. Table 1.2 lists the lattice energy values of CdSe, CdS and InP and their common by-products CdO and In_2O_3.

Table 1.2. Lattice energies of II-VI and III-V crystals and their common by-products

Materials	**Lattice Energy (KJ/mol)**
CdSe[38]	3339
CdS[38]	3489
CdO[27]	3806
InP[39]	3326
In_2O_3[27]	13928

CdS, CdSe and InP have almost similar lattice energies and should show a comparable growth rate in a non-coordinating environment. However, in presence of an oxidizing agent, the by-products, CdO and In_2O_3 should predominate over CdSe and InP respectively. This is because CdO and In_2O_3 have higher lattice energy and it is expected that they should be formed more easily than CdSe and InP respectively. Due to the high In_2O_3 lattice energy, the synthesis of InP has more limitations in the choice of ligands and solvents. Indium precursors form oxide phases more easily, whereas, the cadmium precursors are more stable under the same conditions.

1.7 AN OVERVIEW OF THE THESIS

This thesis centers on the III-V and II-VI semiconductor nanomaterials, specifically InP, ZnSe and CdSe. The next chapter involves InP nanostructures, and the last two chapters deal with ZnSe and CdSe quantum dots. Understanding of the fundamental theories on nanocrystal nucleation, growth, quantum confinement effect and a comparative analysis of III-V and II-VI compounds help to start the investigation within a given range of reaction conditions. It should be mentioned that most theories and development in the field of semiconductor nanoscience are based on the experimental experiences of II-VI compounds.

The study started with the investigation of the potential of phosphido based organometallic compounds as single molecule precursor to InP. This part will be presented in Chapter 2 of this thesis. The second chapter also describes a hazard-free, fast and simple route to clean-surfaced InP nanowires from a single molecule precursor, using the hot injection technique. The wires can be grown without the addition of any strongly binding surfactant stabilizers and in the absence of protic reagents and carboxylic acids. The length of the nanowires could be easily controlled by adjusting the injection temperature. Chapter 3 discusses the syntheses of ZnSe and CdSe quantum dots and the effect of different synthetic parameters. The fourth chapter narrates the coupling of CdSe or ZnSe quantum dots with organic molecule subphthalocyanine to form a new class of hetero nanoassembly. The energy transfer mechanism within these nanoassemblies and other related properties, have been investigated thoroughly and is expected to contribute to the on-going work in our lab in the hierarchical synthesis of nano supramolecular architectures. Finally, in the last chapter (Chapter 5), a critical analysis of the overall research has been presented. The key findings, the significance and the future scopes of this research have been discussed. Several further research avenues have been proposed and potential applications have been mentioned.

REFERENCES

(1) Feynman, R. P. *There′ s Plenty of Room at the Bottom*; Annual Meeting of American Physical Society (Caltech), Dec 29th, 1959: http://calteches.library.caltech.edu/47/2/1960Bottom.pdf.

(2) Ozin, G. A.; Arsenault, A. C.; Cademartiri, L.; Royal Society of Chemistry (Gran Bretanya) *Nanochemistry : A Chemical Approach to Nanomaterials*; Royal Society of Chemistry: Cambridge, 2009.

(3) Taniguchi, N. *On the Basic Concept of "NanoTechnology"* ; Proc. Intl. Conf. Prod. Eng. Tokyo, Part II (Tokyo: Japan Society of Precision Engineering, 1974).

(4) Hunt, W. H. J. *JOM* **2004**, *56*, 13.

(5) *Nanoscience and Nanotechnologies: Opportunities and Uncertainties*; The Royal Society & The Royal Academy of Engineering, July 29th, 2004: http://www.nanotec.org.uk/finalReport.htm.

(6) Stix, G. *Little Big Science*; Scientific American, September 1st, 2001: http://www.scientificamerican.com/article.cfm?id=little-big-science-2001-09.

(7) Smith, A. M.; Nie, S. *Acc. Chem. Res.* **2010**, *43*, 190–200.

(8) Mullin, J. W. *Crystallization*; 4th. ed.; Butterworth-Heinemann: Oxford; Boston, 2001.

(9) Klabunde, K. J.; Richards, R. *Nanoscale Materials in Chemistry*, 2nd ed.; Wiley: Hoboken, N.J., 2009.

(10) Van Embden, J.; Mulvaney, P. *Langmuir* **2005**, *21*, 10226–10233.

(11) Sugimoto, T. *Adv. Colloid Interface Sci.* **1987**, *28*, 65–108.

(12) Peng, X.; Wickham, J.; Alivisatos, A. P. *J. Am. Chem. Soc.* **1998**, *120*, 5343–5344.

(13) Sugimoto, T. *Chem. Eng. Technol.* **2003**, *26*, 313–321.

(14) Lüth, H. *Solid Surfaces, Interfaces and Thin Films*, 5th. ed.; Springer-Verlag Berlin Heidelberg: Berlin, Heidelberg, 2010.

(15) Mićić, O. I.; Smith, B. B.; Nozik, A. J. *J. Phys. Chem. B* **2000**, *104*, 12149–12156.

(16) Battaglia, D.; Peng, X. *Nano Lett.* **2002**, *2*, 1027–1030.

(17) Pradhan, N.; Reifsnyder, D.; Xie, R.; Aldana, J.; Peng, X. *Journal of the American Chemical Society* **2007**, *129*, 9500–9509.

(18) Ji, X.; Copenhaver, D.; Sichmeller, C.; Peng, X. *J. Am. Chem. Soc.* **2008**, *130*, 5726–5735.

(19) Kalyuzhny, G.; Murray, R. W. *The Journal of Physical Chemistry B* **2005**, *109*, 7012–7021.

(20) Talapin, D. V.; Rogach, A. L.; Kornowski, A.; Haase, M.; Weller, H. *Nano Lett.* **2001**, *1*, 207–211.

(21) Hambrock, J.; Becker, R.; Birkner, A.; Weiß, J.; Fischer, R. A. *Chem. Commun.* **2002**, 68–69.

(22) Zhang, Q.; Xie, J.; Yang, J.; Lee, J. Y. *ACS Nano* **2009**, *3*, 139–148.

(23) Wang, C.; Daimon, H.; Onodera, T.; Koda, T.; Sun, S. *Angew. Chem. Int. Ed.* **2008**, *47*, 3588–3591.

(24) Murray, C. B.; Norris, D. J.; Bawendi, M. G. *J. Am. Chem. Soc.* **1993**, *115*, 8706–8715.

(25) Park, J.; Joo, J.; Kwon, S. G.; Jang, Y.; Hyeon, T. *Angew. Chem. Int. Ed.* **2007**, *46*, 4630–4660.

(26) Callister, W. D. *Fundamentals of Materials Science and Engineering*; 5th. ed.; John Wiley & Sons, Inc.: New York; Chichester, 2001.

(27) Lide, D. R. *CRC Handbook of Chemistry and Physics*; 90th. ed.; CRC Press, Boca Raton, Florida, 2010.

(28) Steiner, D.; Katz, D.; Millo, O.; Aharoni, A.; Kan, S.; Mokari, T.; Banin, U. *Nano Lett.* **2004**, *4*, 1073–1077.

(29) Jun, K.-W.; Khanna, P. K.; Hong, K.-B.; Baeg, J.-O.; Suh, Y.-D. *Mater. Chem. & Phys.* **2006**, *96*, 494–497.

(30) R. Heath, J.; Shiang, J. J. *Chem. Soc. Rev.* **1998**, *27*, 65.

(31) Wang, Y.; Lu, J. P.; Tong, Z. F. *Bulletin of Materials Science* **2010**, *33*, 543–546.

(32) Deng, D.-W.; Yu, J.-S.; Pan, Y. *J. Colloid Interface Sci.* **2006**, *299*, 225–232.

(33) Han, H.; Sheng, Z.; Liang, J. *Mater. Lett.* **2006**, *60*, 3782–3785.

(34) Xu, S.; Ziegler, J.; Nann, T. *J. Mater. Chem.* **2008**, *18*, 2653.

(35) Xu, S.; Kumar, S.; Nann, T. *J. Am. Chem. Soc.* **2006**, *128*, 1054–1055.

(36) Micic, O. I.; Curtis, C. J.; Jones, K. M.; Sprague, J. R.; Nozik, A. J. *J. Phys. Chem.* **1994**, *98*, 4966–4969.

(37) Kim, S.-H.; Wolters, R. H.; Heath, J. R. *J. Chem. Phys.* **1996**, *105*, 7957–7963.

(38) Ruberu, T. P. A.; Vela, J. *ACS Nano* **2011**, *5*, 5775–5784.

(39) Verma, A. S.; Sharma, D. *Phys. Stat. Sol. (b)* **2008**, *245*, 678–680.

CHAPTER 2 THERMAL DEGRADATION OF PHOSPHIDO BASED SINGLE MOLECULE PRECURSORS TO FORM INDIUM PHOSPHIDE NANOSTRUCTURES

2.1 INTRODUCTION

Indium phosphide, a member of III-V semiconductor family, has been maintaining its popularity in the form of nanostructures for the last two decades, due to its useful opto-electronic properties, large exciton diameter, covalent character and reduced toxicity. The nanostructures, especially in the form of quantum dots and nanowires have been widely used in nano-optics, nano-electronics, bio-imaging and photodynamic therapy.[1–6] In spite of their several applications, the syntheses of indium phosphide nanostructures, with a narrow size distribution, remained quite challenging due to difficulty in temporal separation of the nucleation and growth stages, both of which are high temperature processes. Nanowires with a clean surface, controllable aspect ratios and lengths are also difficult to obtain. Many post-synthetic treatments require removal of templates or surfactants either under harsh conditions or through multiple washing steps, which might cause damage to the nanowires. Therefore, a large volume of research has been devoted in developing synthetic methodologies to produce high quality InP nanoparticles and nanowires, which involve a wide range of precursors, surfactants, capping agents and solvents. Attempts were also made to reduce the time and temperature of reaction, since in general, InP requires a high temperature and a long time for synthesis (*vide*. Chapter 1). Thus, developing a clean, yet fast synthetic method is still in demand.

With this scenario in the background, we investigated the potential of organometallic indium phosphido compounds, viz. $[R_2InP^tBu_2]_2$ and $[R_2InP(SiMe_3)_2]_2$ (R=Me, Benzyl), as single molecule precursors to form InP nanostructures via β-Hydrogen elimination (alkene elimination) and dealkylsilylation (silane elimination) routes respectively when subjected to thermal degradation (Scheme 2.2). The main difference between our investigation and other work, involving phosphido ligands, is that, we avoided using any other co-reactant in the system and relied solely on thermal degradation of a single organometallic compound as the source of InP nanostructures. Initially, the precursors were subjected to microwave heating in the presence of hexadecylamine and stearic acid, which were included to avoid any potential reduction or oxidation of indium to In^0 or In_2O_3 respectively, as reported by Nann′ s group.[7] Later, due to the slow heating rate of our compounds under microwave conditions we switched to the hot injection technique. Furthermore, we reported a new member of the bis-trimethylsilyl phosphido indium family, viz. $[(PhCH_2)_2InP(SiMe_3)_2]_2$, and showed that this compound can lead to a hazard-free, fast and simple route to clean-surfaced InP nanowires at low temperature, using a hot injection technique, without the addition of any strongly binding surfactant stabilizers and in the absence of protic reagents and carboxylic acids.[8] The nanowire formation relies on the well-known *Solution-Liquid-Solid* (SLS) mechanism, which was first proposed by Buhro and coworkers in 1995 (see Section 2.3).[9] To the best of our knowledge, there are no previous reports on nanowires that can be grown at such low temperature under surfactant-free conditions and the length of which could be easily controlled by adjusting the injection temperature. Additionally, the new precursor would be one of a handful of precursors that thermally decompose directly to InP nanostructures and also generate indium metal catalyst, required for the growth of the nanowires *in situ*.

2.2 PRIOR ART INVOLVING SYNTHESES OF InP NANOSTRUCTURES

Numerous synthetic methodologies for InP nanostructures have been reported to-date, including the synthesis within a solid support, by solvothermal processes, and from inorganic, organometallic and single-molecule precursors. In many cases, the syntheses of InP followed from the syntheses of the II-VI congeners.

Agger *et al.* reported the MOCVD growth of InP quantum dots within a porous solid support, MCM 41, acting as a template, using pyrophoric trimethylindium and PH_3.[10]

Qian reported a solvothermal method to form InP nanocrystals of 12 nm size from the reaction of $InCl_3$ with Na_3P, where no post-synthetic treatment at high temperature was necessary.[11]

After Wells *et al.* first demonstrated the dehalosilylation reaction (Equation 1),[12]

$$(Me_3Si)_3As + MX_3 \longrightarrow MAs + 3\ Me_3SiX \quad \ldots\ldots\ldots\ldots\ldots\ldots(1)$$

where, M = Ga, X = Cl or Br; M = In, X = Cl

as an alternative to the metal alkyls-arsine/phosphine MOCVD routes to III-V nano-materials, numerous researchers started using the solution-phase synthesis of nanoparticles. A number of wet synthetic methods for the preparation of InP nanoparticles and nanowires have emerged ever since then. In 1989, Healy *et al.* were the first to extend the dehalosilylation method to synthesize InP, by reacting $InCl_3$ with $P(SiMe_3)_3$, but they obtained polycrystalline bulk InP.[13] Pioneering work on the successful synthesis of nanocrystals was reported by Micic *et al.* in 1994, where chloroindium oxalate was mixed with $P(SiMe_3)_3$ in acetonitrile in different molar ratios, followed by heating the mixture in

TOPO or TOPO/TOP at 270 °C for several days. The choloroindium oxalate was prepared by heating a mixture of anhydrous $InCl_3$ and sodium oxalate in acetonitrile at 70 °C for 15 h.[14] Indium chloride has also been widely used in the syntheses of InP nanostructures, since the indium is free for coordination with a variety of ligands to form complexes *in situ*, that are easily soluble in the reaction solvent.[7] Guzelian *et al.* used $InCl_3$ and $P(SiMe_3)_3$ in strongly coordinating TOPO, to form InP at 265 °C for six days. $InCl_3$ initially forms a complex with TOPO. The complex reacts with $P(SiMe_3)_3$ at elevated temperature over a period of several days to form TOPO capped InP.[15] Yan *et al.* obtained InP nanospherical grains (15-20 nm) and nanorod-like grains (150 x 1500 nm), by the reaction of $InCl_3$, KBH_4 and white phosphorus in ethylenediamine (en) at 120 °C and 160 °C respectively. The reaction proceeded through a metallic indium intermediate and a SLS mechanism is proposed for the one-dimensional growth.[16]

$$2\ InCl_3 + 6\ KBH_4 \xrightarrow{en} 2\ In^0 + 6\ KCl + 6\ BH_3 + 3\ H_2 \ldots\ldots\ldots\ldots(2)$$

$$4\ In + P_4 \xrightarrow{en} 4\ InP \ldots\ldots\ldots\ldots\ldots\ldots\ldots\ldots\ldots\ldots\ldots\ldots(3)$$

Though $InCl_3$ has been widely used in the synthesis of InP nanostructures, using a halogen-containing precursor also opens up the possibility of incorporating halogen impurities into the nanoparticles. Halide contamination has been proved to be detrimental in semiconductor materials, due to the introduction of charge carriers that leads to charge leakage, reduced capacitance, and eventually device failure. Thus developing a synthetic procedure that is not plagued by any halogen contamination is important from both academic and industrial points of view.

Peng and co-workers first adopted a non-coordinating solvent, 1-octadecene (ODE), for the synthesis of InP nanocrystals. Indium acetate and $P(SiMe_3)_3$ were used as the precursor.[17] Generally, in a non-coordinating solvent, either indium carboxylate is directly used, or an indium precursor is heated in the presence of a fatty acid.[6,18] The carboxylate group is believed to act as an *in situ* coordinating ligand that leads to a controllable nucleation and growth of the nanocrystals. Following these syntheses, Nann' s group reported the use of weakly coordinating solvents - methyl myristate and dibutyl sebacate for the synthesis of high quality InP quantum dots with trimethylindium and $P(SiMe_3)_3$ in the presence of protic reagents viz. amines and carboxylic acids.[19] Similarly Liu *et al.* used $InMe_3$ and $P(SiMe_3)_3$ to generate InP nanowires in octadecene (ODE) in the presence of myristic acid. Clean production of nanowires was observed at >280 °C, while at lower temperatures, a mixture of nanoparticles and nanowires was produced and no wire growth was observed at 260 °C.[20] By contrast, Weller and co-workers recently reported the growth of InP nanorods from $InMe_3$ and trioctylphosphine in the presence of TOPO at the much lower optimum growth temperature of 200 °C, while higher temperatures increased the size of the In droplets and led to multiple nanorod growth per droplet.[21]

Single molecule precursors have also gained a lot of attention since both the elements of the semiconductor compound comes from a single source and are already bonded together. Green and O′ Brien obtained InP quantum dots by heating $In(P^tBu_2)_3$ in 4-ethylpyridine at 167 °C for several days.[22,23] Organometallic In and Ga phosphides had initially gained popularity as single molecule precursors to InP and GaP thin films. For example, $[Me_2InP^tBu_2]_2$ has been used to grow InP films through molecular beam epitaxy.[24] Thermolysis of $[Me_2InP(SiMe_3)_2]_2$ has been reported to produce polycrystalline InP.[25] Later, attempts were made to use these compounds to grow crystalline III-V nanostructures through solution phase synthetic methods, but in every case one (or more) co-reactant was used. For example, Trentler *et al.* used the methanolysis of $[^tBu_2InP(SiMe_3)_2]_2$, to obtain polycrystalline InP fibers of

10–100 nm diameter. They demonstrated that the protic additive, methanol, cleaves the In–P and P–$SiMe_3$ bonds, generating $[^tBu_2In(OMe)]_2$ and $[^tBu_2In(PH_2)]_3$ as intermediates (Scheme 2.1).

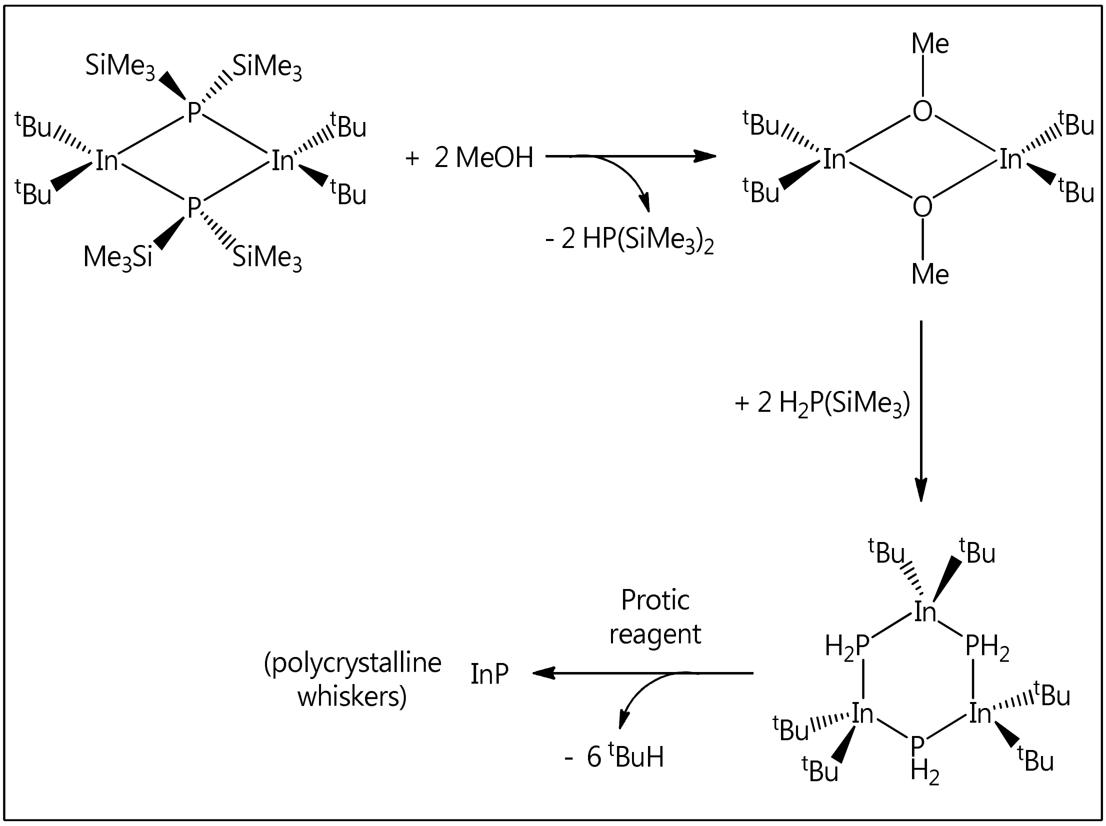

Scheme 2.1. Formation of polycrystalline InP whiskers from the methanolysis of $[^tBu_2InP(SiMe_3)_2]_2$, as reported by Trentler *et al.*[26]

Nanofiber growth occurred from indium metal nanodroplets formed by reduction of some of the precursor, and tert-alkyl substituents in particular were thought to be linked to this reductive decomposition pathway.[26] External addition of low-melting metal nanoparticles (In^0 or Bi^0), to act as seeds in the SLS growth of the nanowires, have been reported.[27–29] However, due to the high reactivity of In^0 nanoparticles, their synthesis and storage is rather difficult. To circumvent this problem, instead of using pre-prepared In^0 catalyst, Ahrenkiel et al. used a mixture of two molecular precursors, viz. $[^tBu_2InP(SiMe_3)_2]_2$ and $[Cl_2InP(SiMe_3)_2]_2$ together with donor surfactants such as dodecylamine and trioctylamine in the presence of trioctylphosphine (TOP), trioctylphosphine oxide (TOPO) and MeOH at temperatures of up to 250 °C. The $[^tBu_2InP(SiMe_3)_2]_2$ produced a large number of In^0 droplets *in situ* and less InP, whereas, the halogen containing compound, $[Cl_2InP(SiMe_3)_2]_2$, generated only InP but no In^0. Thus to increase the total InP concentration, they used a mixture of the above two compounds. These authors also found that $In(P^tBu_2)_3$ precursors at 330 °C gave tadpole-like InP fibers attached to large indium metal droplets.[30]

2.3 THE SLS MECHANISM

The formation of nanowires is quite different than that of the zero dimensional quantum dots, due to an unrestricted one-dimensional growth of the wires along one particular axis. Thus, other than precursor decomposition to a semiconductor compound of desired stoichiometry, there has to be a certain mechanism in operation, which can initiate and maintain this directed growth of the wires. Several methodologies have been developed for this purpose, including Vapor-Liquid-Solid (VLS),[31,32] Solution-Liquid-Solid (SLS),[9,20] Laser Catalytic Growth (LCG),[33,34] oxide assisted growth[35,36] and templating strategies.[37,38] Among these, the SLS mechanism operates in the solution phase, can be easily executed within a regular laboratory set-up, generates dimensionally well-controlled monocrystalline nanowires and thus, has become a nearly general method for the synthesis of semiconductor nanowires.

As mentioned earlier, the SLS mechanism was first proposed by Buhro and co-workers in 1995, when they found that on reacting In^tBu_3 and PH_3 in the presence of protic reagents, InP whiskers of 10-100 nm diameter are formed and at the tip of each whisker, a droplet of metallic indium is attached. As per Buhro, the strongest evidence of the proposed SLS mechanism is the quasi-one-dimensional growth morphologies and indium droplets attached to the nanowire tips in the materials.[9]

The SLS mechanism is very much analogous to the previously known VLS mechanism;[32] however, in SLS, the liquid flux droplets are fed from the solution instead of from the vapor phase. The mechanism comprises the following 3 steps-

Step I: Formation of nanosized In^0 liquid **(L)** flux droplets, acting as seeds.

Step II: Elements In and P are continuously fed into the flux from the solution **(S)**.

STEP III: One dimensional growth of the solid **(S)** crystalline InP nanowires after the flux droplet becomes supersaturated with In and P.

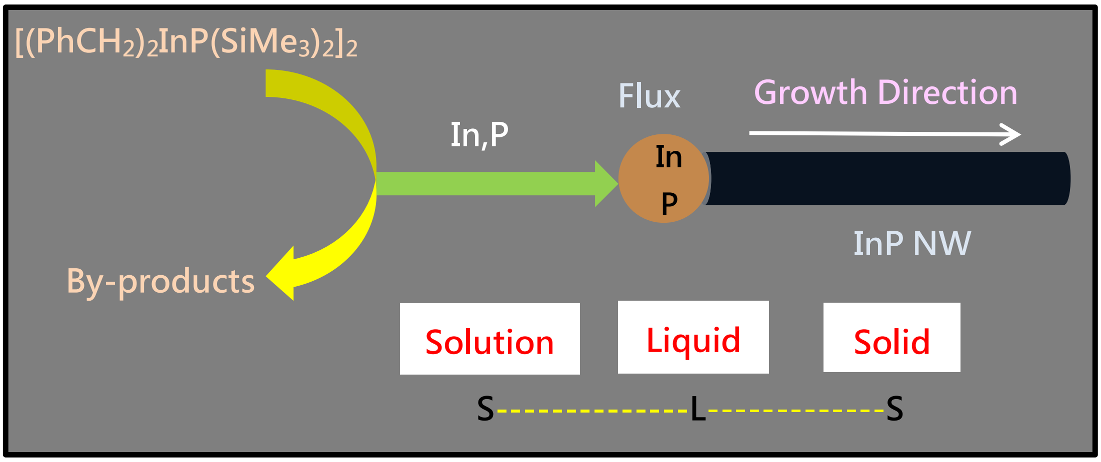

Figure 2.1. Schematic diagram of the Solution-Liquid-Solid mechanism.

2.4 SINGLE MOLECULE PRECURSOR SELECTION

The single molecule precursors used in the current research can be broadly divided into two general classes, viz. $[R_2InP^tBu_2]_2$, containing the di-tert. butylphosphido group ($^tBu_2P^-$) and $[R_2InP(SiMe_3)_2]_2$, containing the bis-(tri-methylsilyl)phosphido group $[^{-}P(SiMe_3)_2]$ attached to indium. R is methyl or benzyl group in each case (Figure 2.2).

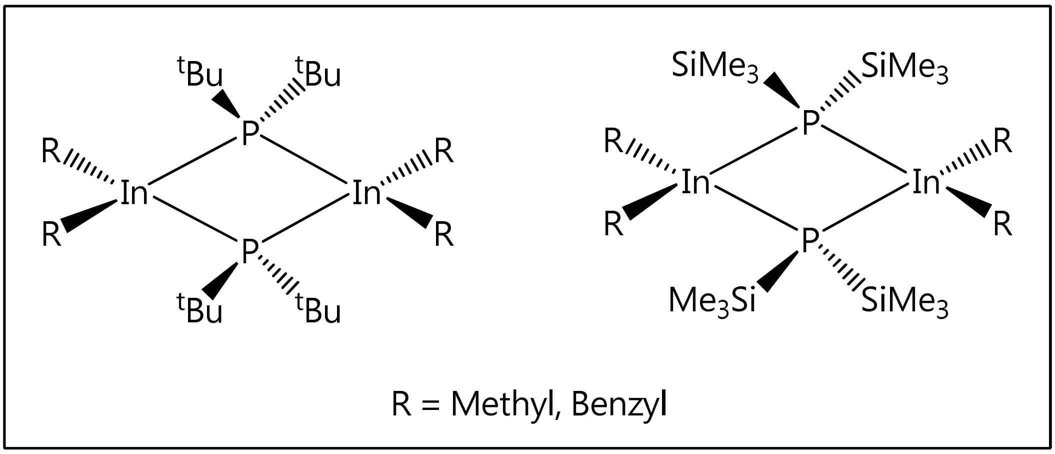

R = Methyl, Benzyl

Figure 2.2. Chemical structure of the two classes of phosphido precursors.

The primary reasons to select these two classes of precursors are –

(i) They do not contain any halogen atom.

(ii) They have an exact 1:1 stoichiometry in In and P.

(iii) Some InP MOCVD precursor adducts of the type $Me_3In.PR_3$ have been used in the past, [39] which are prone to dissociation. The In-P bonds in our precursors being covalent and stronger in nature than those in the adducts, are expected to remain intact during thermal decomposition, to form InP.

(iv) They have low decomposition temperature, so formation of nanostructures could be achieved at relatively low temperatures compared with that reported earlier.

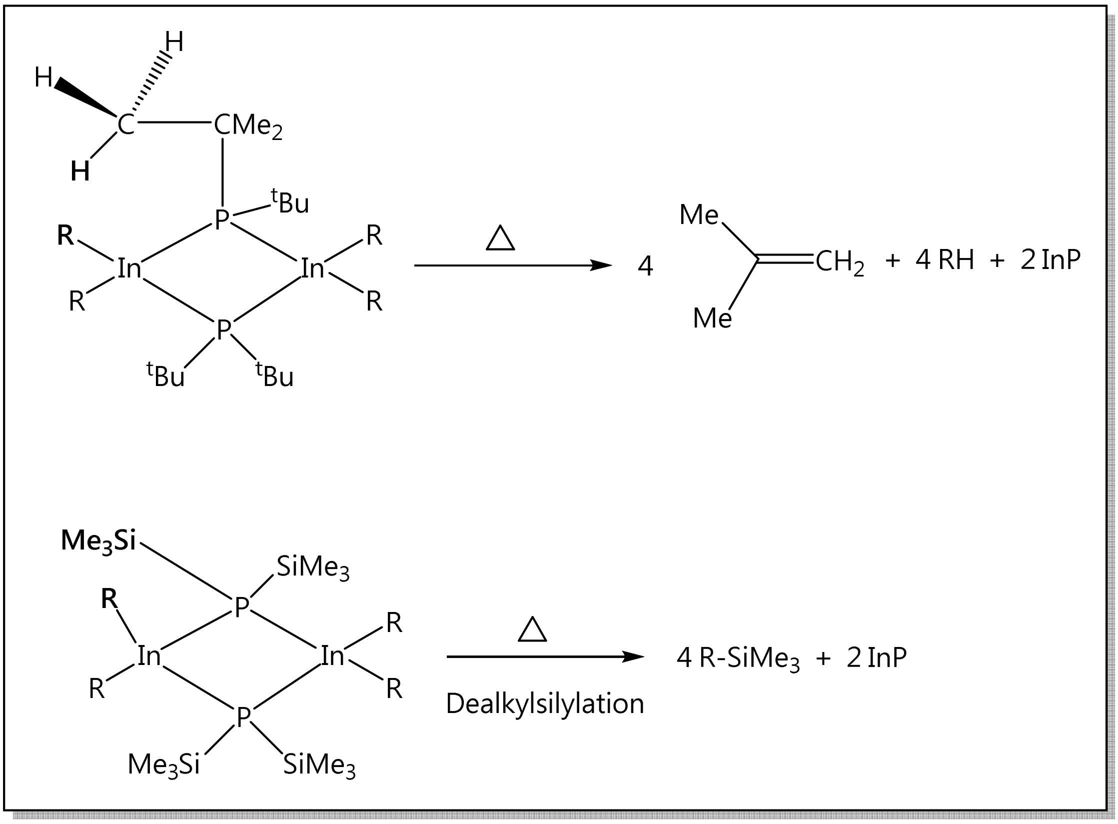

Scheme 2.2. Expected decomposition pathways of the precursors.

(v) The $[R_2InP^tBu_2]_2$ and $[R_2InP(SiMe_3)_2]_2$ have potential to undergo facile thermal degradation by the elimination of alkenes (via β-Hydrogen elimination) and silanes (via dealkylsilylation) respectively (Scheme 2.2).

To investigate the potential of these two classes of compounds in the formation of InP nanostructures, they were subjected to thermal degradation by either Microwave heating and/or by the Hot Injection method.

2.5 OTHER REACTION COMPONENTS USED

In our early attempts, along with the precursors, we also included some conventional stabilizing agents of nanocrystals, viz. hexadecylamine (HDA), stearic acid (SA) and zinc undecenoate (ZnU). The solvent used was diphenyl ether (DPE).

Nann′ s group reported that hexadecylamine, along with zinc carboxylates (zinc undecenoate) can reduce surface dangling bonds, thereby causing surface passivation and reduce defects. Amines can also act as stabilizing ligands and prevent any aggregation of nanocrystals. We have thus included hexadecylamine and zinc undecenoate into our systems.

It has been reported that indium compounds can be readily reduced by amines to indium metal.[7] Nozik' s group prepared In^0 nanoparticles by reduction of tributyl indium with HDA.[27] On the other hand, indium is also highly prone to oxidation to In_2O_3. It has been reported that an appropriate ratio of hexadecylamine and stearic acid has the ability to prevent any potential reduction or oxidation of indium in InP nanocrystals.[7] This balance of ratio becomes more subtle at high temperatures, since the electron accepting or donating ability of Lewis acids or bases usually increases with temperature. Therefore, stearic acid was also included along with hexadecylamine. As mentioned earlier, stearic acid was also expected to behave as a coordination ligand in the current work, which would lead to a controllable nucleation/growth process and also stabilize the nanocrystals from any aggregation after they are formed.

2.6 SYNTHETIC SCHEMES OF THE SINGLE MOLECULE PRECURSORS

A brief outline of the synthetic routes of the precursors, $[R_2InP^tBu_2]_2$ and $[R_2InP(SiMe_3)_2]_2$, is given here before starting to investigate their role in the formation of InP nanostructures. The detailed synthetic procedures have been placed in the experimental section at the end of this chapter.

2.6.1 Precursor $[R_2InP^tBu_2]_2$ (R = Me or $PhCH_2$):

In the syntheses of this class of precursor, lithium di-tert. butylphosphide ($^tBu_2PLi$) was used to introduce the In-P bond. The lithium derivative was made from di-tert. butylphosphine, which in turn was synthesized as outlined in Scheme 2.3.

The completion of the reaction to form $^tBu_2PCl$ (Step b) was confirmed by recording a ^{31}P NMR spectrum of an aliquot of the reaction mixture. The presence of a single peak confirms the completion of the reaction.

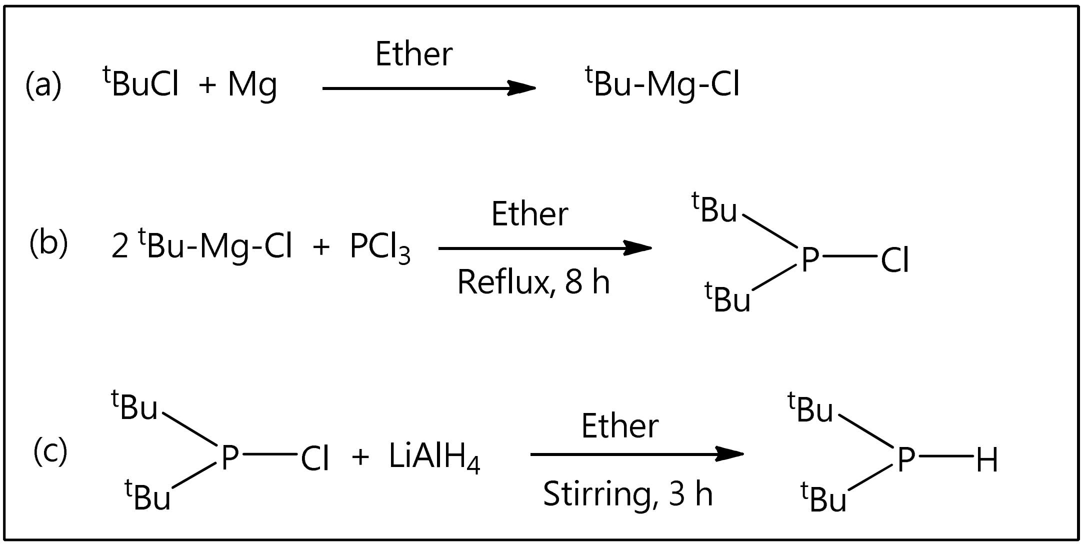

Scheme 2.3. Synthesis of di-tert. butylphosphine.

The di-tert. butylphosphine was lithiated by the action of ^{n}BuLi on the phosphine.

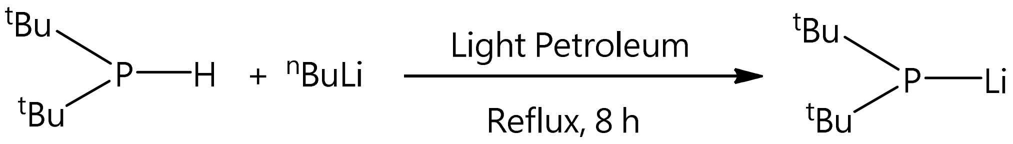

Scheme 2.4. Synthesis of ${}^{t}Bu_2PLi$ from di-tert.butylphosphine.

The ${}^{t}Bu_2PLi$ was a light-yellow solid, with a pungent smell and was extremely pyrophoric.

The syntheses of the di-tert. butylphosphido precursors followed previous literature methods.[40,41] Both the compounds were prepared through salt elimination reactions, which is a one-pot method and can be carried out at a very low temperature. The alkylating agent was either MeLi or benzyl Grignard (Scheme 2.5).

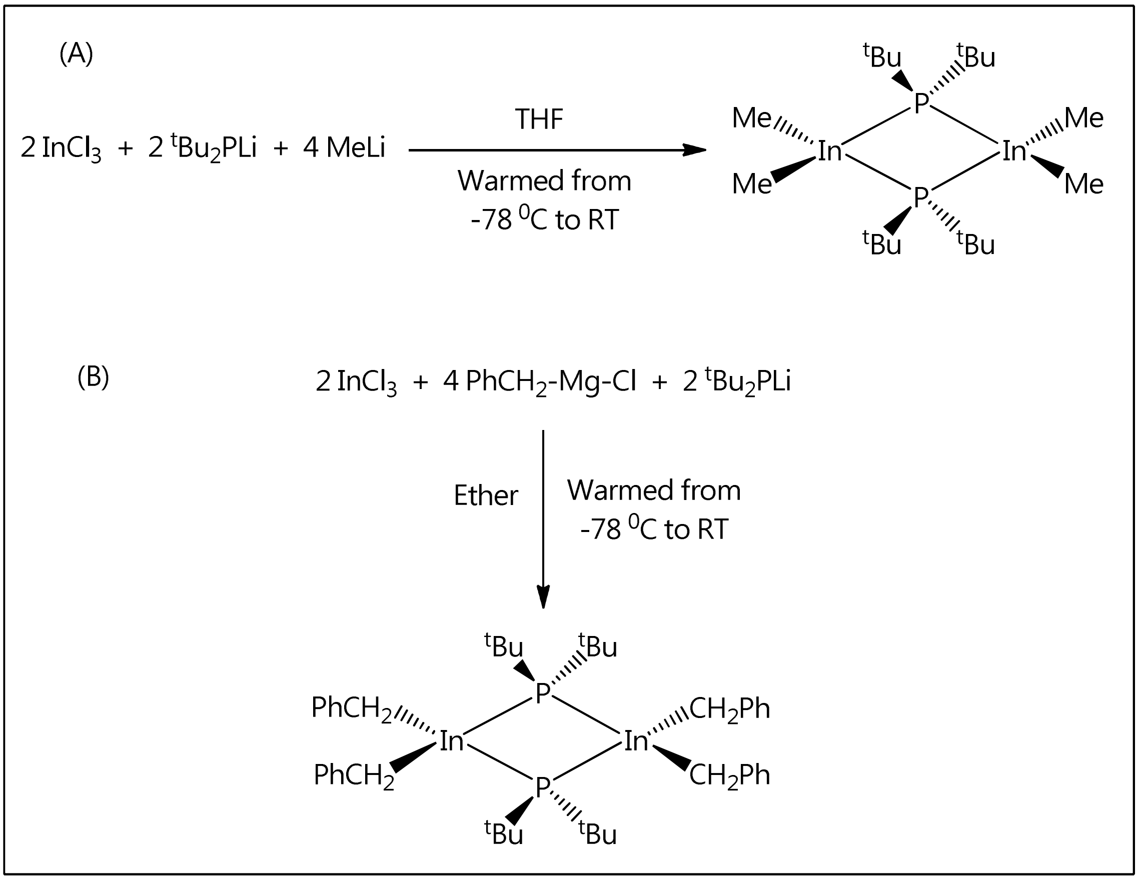

Scheme 2.5. Synthesis of the precursor $[R_2InP^tBu_2]_2$, where, R = (A) Me, (B) $PhCH_2$.

The compounds are obtained as colorless crystals and are air stable for a short period of time. They decompose at 280 ℃ (R=Me) and 225 ℃ ($R=PhCH_2$).

2.6.2 Precursor $[R_2InP(SiMe_3)_2]_2$ (R = Me or $PhCH_2$):

To form this class of precursor, $P(SiMe_3)_3$ was employed to form the In-P bond replacing the In-Cl bond in $InCl_3$ starting material.

From White Phosphorus:

(a) $$12\ Na + P_4 \xrightarrow[\text{THF}]{\text{Napthalene}} 4\ Na_3P$$

(b) $$Na_3P + 3\ Me_3SiCl \xrightarrow[\text{Reflux, 6 h}]{\text{DME}} P(SiMe_3)_3 + 3\ NaCl$$

yield: 60%

From Red Phosphorus:

(a) $$3\ K/Na + 1/x\ P_x \xrightarrow[\text{Reflux, 24 h}]{\text{DME}} 4\ (K/Na)_3P$$

(b) $$(K/Na)_3P + 3\ Me_3SiCl \xrightarrow[\text{Stir, 1 h}]{\text{DME}} P(SiMe_3)_3 + 3\ (K/Na)Cl$$

yield: 50%

DME = 1,2-Dimethoxyethane

Scheme 2.6. Synthesis of $P(SiMe_3)_3$ from white and red phosphorus.

$P(SiMe_3)_3$ was made both from white and red phosphorous, and was obtained as a colorless liquid (Scheme 2.6). The dimethyl derivative of the precursor was prepared following literature procedures, whereas, the dibenzyl derivative we report for the first time.

(I) [$Me_2InP(SiMe_3)_2]_2$[25,42]

The target compound was synthesized through the formation of Me_2InCl as an intermediate first and then subsequent reaction of Me_2InCl with $P(SiMe_3)_3$ to yield the final product (Scheme 2.7).

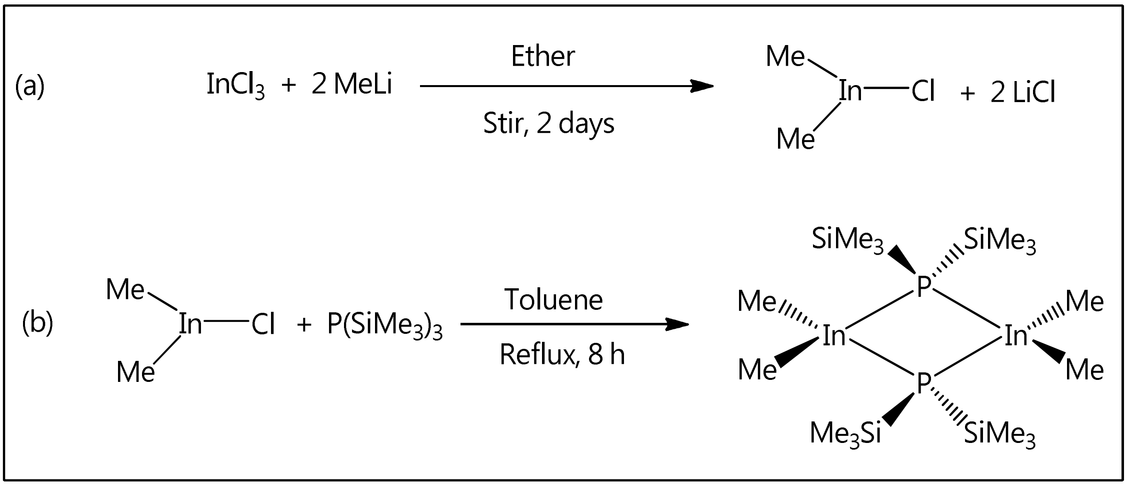

Scheme 2.7. Synthesis of the [$Me_2InP(SiMe_3)_2]_2$.

A successful formation of Me_2InCl depends largely on the molar ratio of the reactants and the time of reaction. The $InCl_3$: MeLi molar ratio needs to be strictly 1:2. However, trimethyl indium could also form if the molar ratio is 1:2 in addition to dimethyl indium chloride, depending upon the time of reaction. Literature reports that if the products are isolated as soon as the initial vigorous reaction is completed (*ca*. 30 min), trimethyl indium would be isolated.[42] To isolate the dimethylindium chloride compound, the reaction in this work was stirred vigorously for two days, during which if any trimethyl indium formed, would be converted to the dimethylindium chloride, according to the following equation:

$$2\,Me_3In + InCl_3 \rightleftharpoons 3\,Me_2InCl$$

The final target dimethyl compound was obtained as a colorless crystalline solid through a dehalosilylation reaction by the action of $P(SiMe_3)_3$ on Me_2InCl. The dimethyl precursor is fairly stable in air for a short time and decomposes around 240 °C.

(II) $[(PhCH_2)_2InP(SiMe_3)_2]_2$

The dibenzyl precursor was obtained by two step reactions – (a) the formation of dibenzylindium chloride from the reaction of $InCl_3$ and benzyl Grignard in the molar ratio 1:2 through a salt elimination pathway,

(b) the reaction of dibenzylindium chloride with $P(SiMe_3)_3$ via a dehalosilylation route (Scheme 2.8).

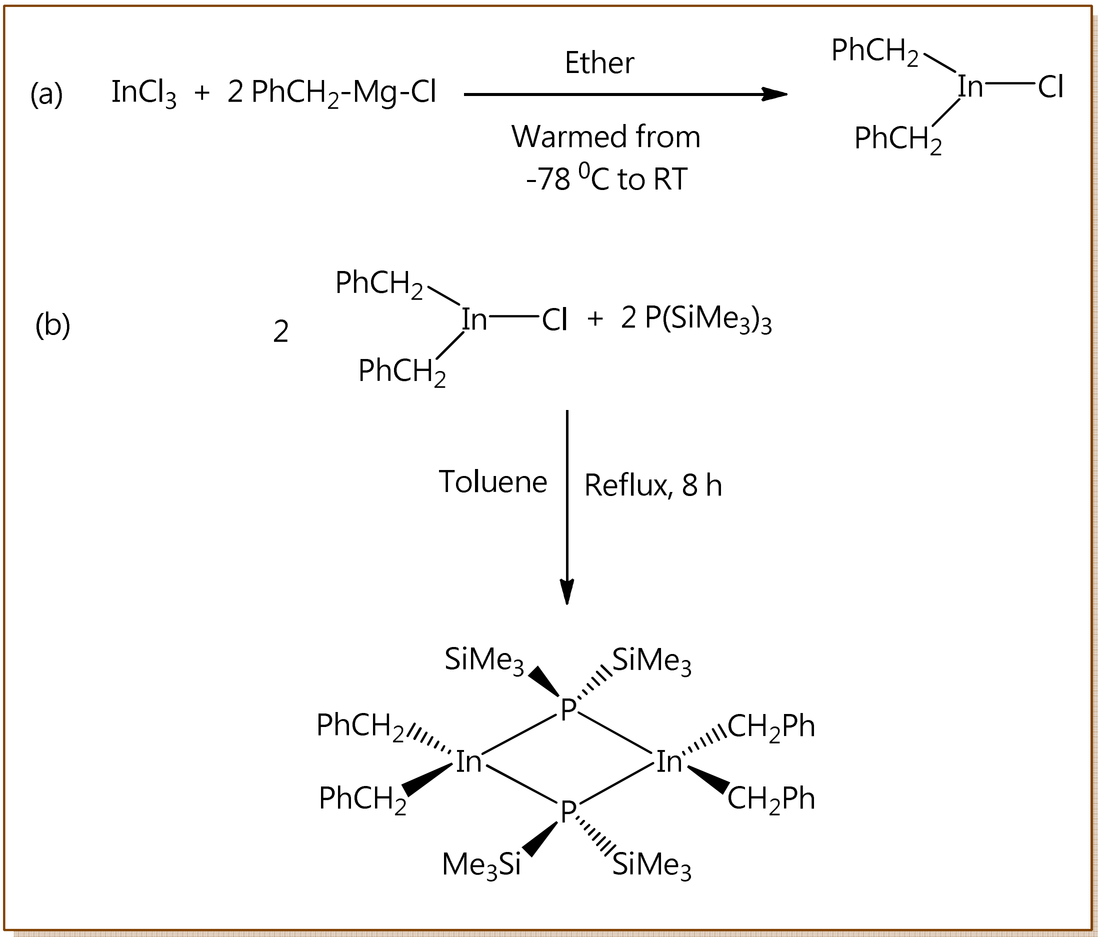

Scheme 2.8. Synthesis of the $[(PhCH_2)_2InP(SiMe_3)_2]_2$.

The dibenzyl precursor was obtained as large colorless crystals, suitable for single crystal X-ray analysis. The compound is fairly stable in air for a short period of time and decomposes at 210 °C.

The X-ray structure shows that the compound is dimeric (Figure 2.3). X-ray analysis also reveals an interesting feature in the conformation of the benzyl groups in our precursor, which is very similar to that found in [(PhCH$_2$)$_2$InP^{t}Bu$_2$]$_2$, reported previously.[41] In order to minimize steric interactions between the benzyl and the trimethylsilyl groups, the benzyl group attached to C(3), extends straight out from the In atom and bisects two P-SiMe$_3$ moieties, resulting in the angle C(31)-C(3)-In to be very close to the ideal tetrahedral value (108.73 ^{0}). In the case of the other benzyl group, attached to C(4), inter-aryl repulsion compels a conformation, in which it is oriented toward a P-SiMe$_3$ group.

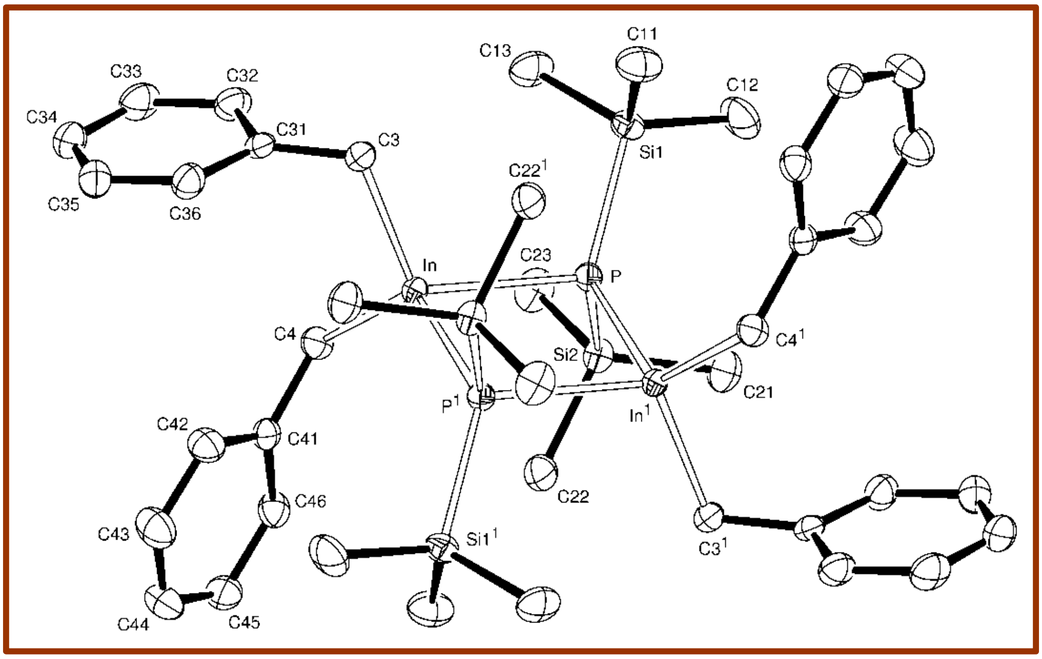

Figure 2.3. Molecular structure of [(PhCH$_2$)$_2$InP(SiMe$_3$)$_2$]$_2$.

Table 2.1. Selected bond lengths and bond angles in

$[(PhCH_2)_2InP(SiMe_3)_2]_2$

Selection	Bond Lengths (Å)	Bond Angles (^{0})
In-P	2.6085 (5)	-
In-P′	2.6160 (4)	-
In-C(3)	2.2279 (15)	-
In-C(4)	2.2013 (14)	-
P-Si(1)	2.2507 (5)	-
P-Si(2)	2.2516 (6)	-
P-In-P′	-	86.652 (14)
In-P-In′	-	93.348 (14)
C(3)-In-C(4)	-	110.00 (6)
C(31)-C(3)-In	-	108.73 (10)
C(41)-C(4)-In	-	118.88 (10)

As a consequence, the steric interactions between this benzyl and $SiMe_3$ group increases. To reduce this steric crowding, the angle C(41)-C(4)-In becomes considerably larger than the ideal tetrahedral value (118.88 ^{0}).

2.7 RESULTS AND DISCUSSIONS

2.7.1 Microwave Heating of the Precursor $[R_2InP^tBu_2]_2$

A mixture of $[R_2InP^tBu_2]_2$ precursor (0.1 mmol w.r.t. indium), hexadecylamine (0.2 mmol), stearic aicd (0.1 mmol) and zinc undecenoate (0.1 mmol) was dissolved in diphenyl ether (4 mL) and placed in a microwave heating tube. The tube, with its contents, was subjected to microwave heating at pressure 20 bar and 300 W power. The temperature was increased stepwise, with a hold time of 20 min at each temperature. Table 2.2 shows the observations at each temperature for both the methyl and the benzyl derivatives.

We found that for both the di-tert.butylphosphido compounds, In^0 precipitated, the amount increased with an increase in temperature. The resulting solution showed no luminescence under UV illumination.

To stop the unwanted formation of indium metal, a similar microwave study was performed without the amine (Table 2.3). It was found that even in absence of HDA, In^0 was precipitated, and a strong smell of phosphine could be perceived. The blue luminescence of the solution observed under UV illumination disappeared upon centrifugation. This was probably due to the Tyndall effect, i.e. scattering from the suspended colloidal indium particles.

Table 2.2. Microwave studies of $[R_2InPBu^t{}_2]_2$ at different temperatures with HDA at Pressure = 20 Bar & Power = 300 Watt

Precursors* (R)	**Temperature (℃)**	**Hold Time (min)**	**Observations**
Me	170	20	Clear solution
	190	20	,,
	200	20	,,
	220	20	,,
	230	20	,,
	250	20	,,
	270	20	Black In^0 ppt.
	290	20	,,
$PhCH_2$	180	20	,,
	200	20	,,
	220	20	,,

***Recipe:** Precursor (0.1 mmol), HDA (0.2 mmol), SA (0.1 mmol), ZnU (0.1 mmol), and DPE (4 mL)

Table 2.3. Microwave studies of $[R_2InPBu^t{}_2]_2$ at different temperatures without HDA at Pressure = 20 Bar & Power = 300 Watt

Precursors* (R)	**Temperature (℃)**	**Hold Time (min)**	**Observations**
Me	180	15	Clear solution
	200	15	,,
	220	15	,,
	240	15	Black In^0 ppt.
	260	15	,,
$PhCH_2$	120	20	Clear solution
	140	20	,,
	160	20	,,
	180	20	,,
	200	20	Turbidity
	220	20	Black In^0 ppt.
	240	20	,,
	260	20	Black In^0 ppt. Blue lumines.
	290	20	,,

***Recipe:** Precursor (0.1 mmol), SA (0.3 mmol), ZnU (0.1 mmol), and DPE (4 mL)

It appears that instead of the formation of InP through alkene elimination, the phosphido precursor undergoes a reductive elimination of alkane to yield RP^tBu_2 and metallic indium (Scheme 2.9). The phosphine seems to be more stable thermodynamically, and is formed at the expense of the In-P bond in the precursor.

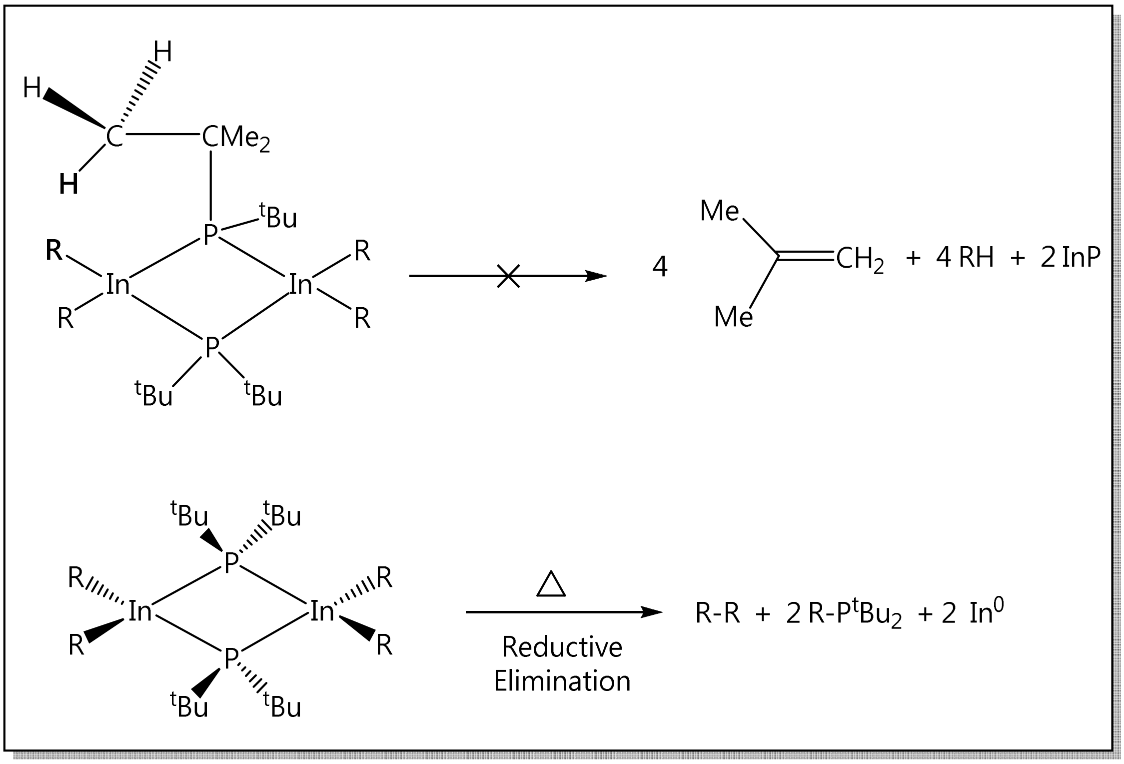

Scheme 2.9. Formation of metallic indium from the di-tert. butylphosphido precursor.

2.7.2 Microwave Heating of the Precursors $[R_2InP(SiMe_3)_2]_2$

Similar to the di-tert. butylphosphido precursors, the bis-(trimethylsilyl) phosphido precursors were also subjected to microwave heating with hexadecylamine (HDA) in the system. Table 2.4 shows the microwave study of the methyl derivative in the presence of HDA.

Table 2.4. Microwave studies of $[Me_2InP(SiMe_3)_2]_2$ at different temperatures with HDA at Pressure = 20 Bar & Power = 300 Watt

Precursor*	**Temperature (℃)**	**Hold Time (min)**	**Observations**
Me	100	15	Clear solution
	120	15	"
	140	15	"
	160	15	"
	180	15	"
	200	15	"
	220	15	Turbidity
	240	15	Black In^0 ppt.

***Recipe:** Precursor (0.1 mmol), HDA (0.2 mmol), SA (0.1 mmol), ZnU (0.1 mmol), and DPE (4 mL)

It was observed that the bis-(trimethylsilyl)phosphido precursor also gets reduced to metallic indium. Amines, reported to behave as a reducing agent, can easily react with highly active nuclei and small nanocrystals.

2.7.3 Hot Injection Studies of the Precursor $[R_2InP(SiMe_3)_2]_2$

During the course of our experiments with microwave heating, we found that $[Me_2InP(SiMe_3)_2]_2$ takes *ca.* 10 min in the microwave to reach the temperature of 280 °C. This time to reach the ramping temperature can be considered to be extremely slow in the synthesis of nanocrystals, where an instantaneous heating to initiate nucleation is highly desirable. This slow heating rate is due to the non-polar nature of our precursors, which makes them poor microwave absorbers, whereas molecules with permanent dipoles can efficiently absorb microwave energy. To induce an instantaneous nucleation burst, the hot injection technique appears to be more appropriate for such non-polar compounds.

Hot Injection studies of both $[Me_2InP(SiMe_3)_2]_2$ and $[(PhCH_2)_2InP(SiMe_3)_2]_2$ at an injection temperature of 280 ℃ and growth temperature of 240 ℃ also showed that there was always formation of grey/black metallic indium particles if hexadecylamine was present.

Therefore, in all further experiments hexadecylamine was not added into the reaction mixture.

When either $[Me_2InP(SiMe_3)_2]_2$ or $[(PhCH_2)_2InP(SiMe_3)_2]_2$ were subjected to hot injection degradation at an injection temperature of 310 °C and growth at 250 °C for 10 min, in the absence of hexadecylamine, for the first time we found that no metallic indium precipitated and instead InP nanocrystals were formed. The particles showed an orange luminescence under UV illumination. Figure 2.4 shows the UV-visible and photoluminescence spectra of the InP nanocrystals. TEM image shows the InP particles are spherical in shape and are of ~3 nm size (Figure 2.5).

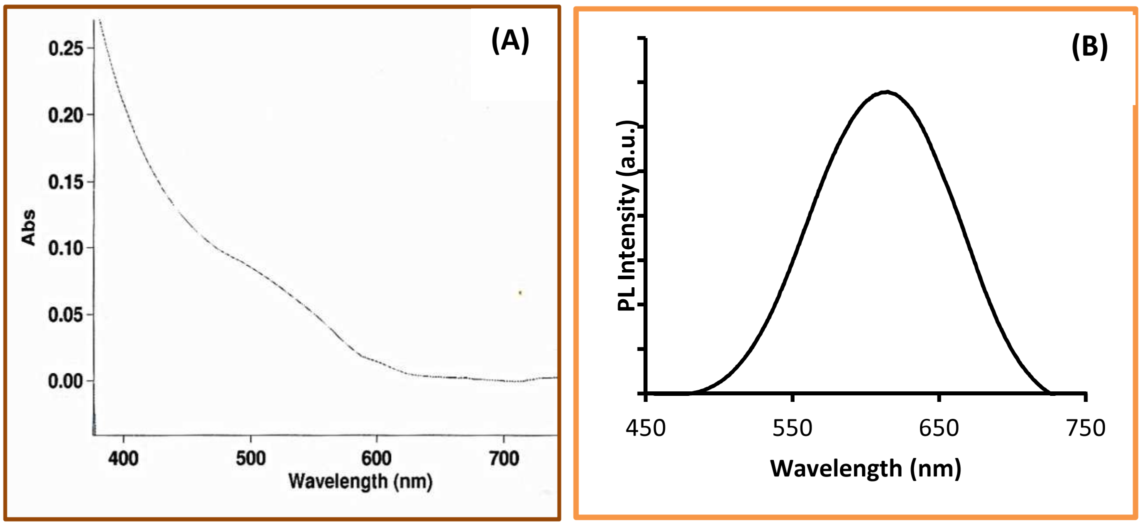

Figure 2.4. (A) UV-visible and (B) Photoluminescence spectra of InP.

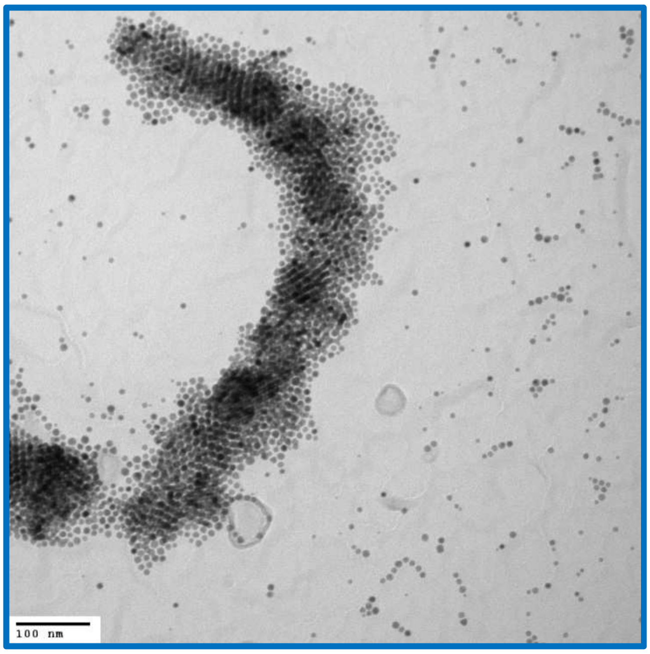

Figure 2.5. TEM image of the InP nanoparticles.

2.7.4 Effect of Stearic Acid

As soon as we found out that the bis-(trimethylsilyl)phosphido precursors were able to produce InP in the nano regime, through a hot injection technique, we were interested to know the role of stearic acid, which has been widely used in the syntheses of quantum dots. An NMR spectrum was recorded of a mixture of $[(PhCH_2)_2InP(SiMe_3)_2]_2$ and a 10 fold excess of stearic acid in C_6D_6 in a closed NMR tube. Stearic acid $[HOOC-CH_2-CH_2-(CH_2)_{14}-CH_3]$ should yield one triplet (α protons) and quintet (β protons), but it was found that two triplets and two quintets appear along with toluene $-CH_3$ singlet at 2.1 (Figure 2.6).

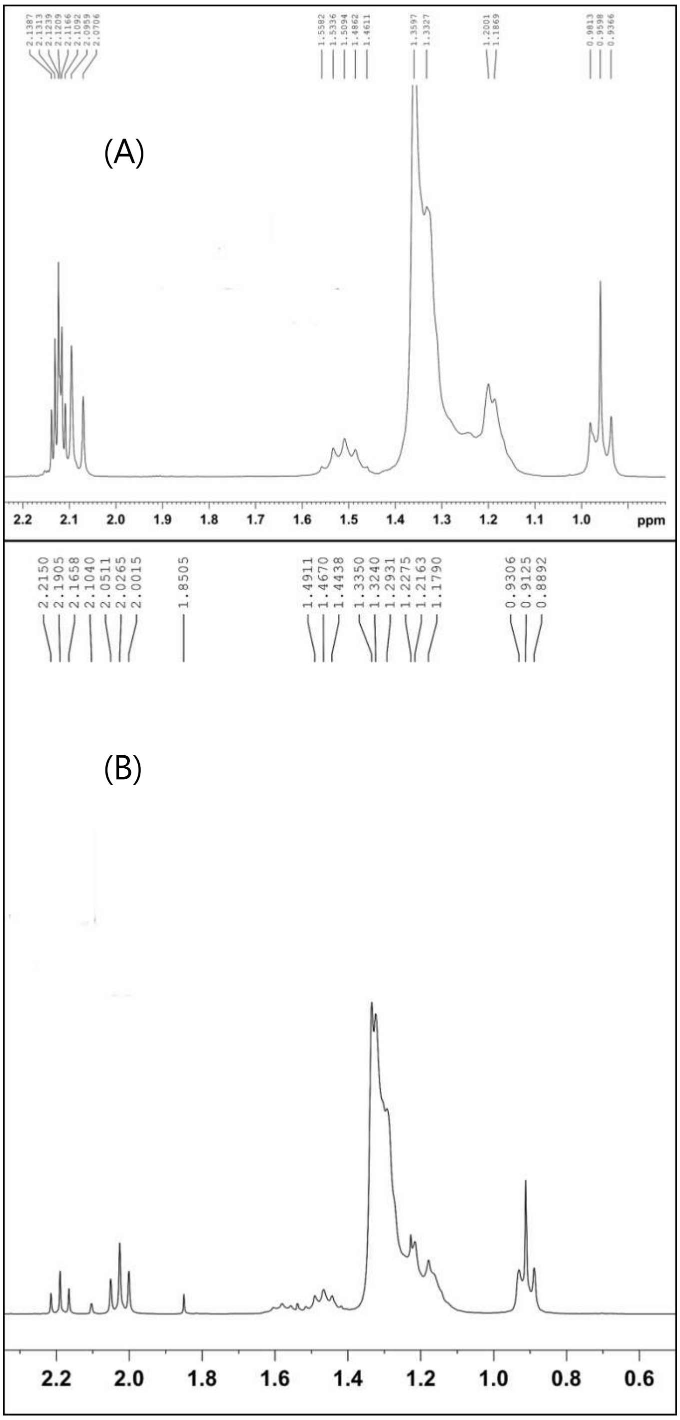

Figure 2.6. NMR spectra of (A) pure stearic acid in D^8 toluene (B) stearic acid in $[(PhCH_2)_2InP(SiMe_3)_2]_2$ in D^6 benzene.

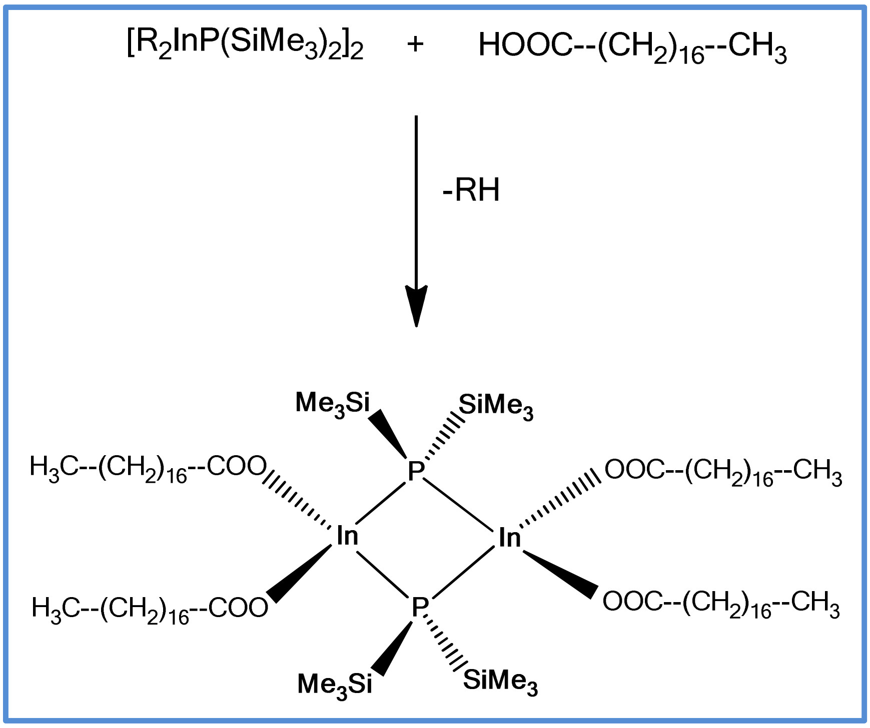

Scheme 2.10. Reaction of stearic acid with bis-(trimethylsilyl)phosphido precursor.

It can be concluded that the benzyl group is replaced by stearic acid and a stearate is formed as an intermediate. The stearate and the free stearic acid give rise to two triplets and quintets. A common stearate intermediate is formed regardless of the -R group attached to indium (Scheme 2.10). Therefore, in the presence of stearic acid changing the alkyl group on the indium, or a combination of stearic acid and indium chloride (as published already)[7,19] would all behave the same and would not affect the nanoparticle growth behavior.

To replace stearic acid, an alternative needs to be used, which would not only be unreactive toward the -R group attached to the indium, but also impart stability to the nanoparticles after their formation. High boiling esters are weakly coordinating and do not cleave In-alkyl bonds, and unlike strongly coordinating solvents, lead to a more controlled nucleation process. Methyl myristate was used for this purpose. This ester is inexpensive, non-toxic, has a high boiling point of 330 °C and is weakly coordinating.

2.7.5 $[(PhCH_2)_2InP(SiMe_3)_2]_2$ Precursor in Methyl Myristate

The dibenzyl precursor was injected into neat methyl myristate at a high temperature (310 °C) and immediately after the injection, a black precipitate formed. The temperature dropped down to 250 °C, and heating was continued at 250 °C for 10 min. After cooling the flask, the black precipitate was observed under TEM and it was found that nanopins (or nanowires) were formed, with a black globule of metallic indium at the base of each wire. The dibenzyl precursor generated nanowires via thermal decomposition, without the need of any co-reactant, surfactant or any protic reagent. Therefore, in a true sense, the dibenzyl precursor served as a single molecule precursor to nano-dimensional indium phosphide. The decomposition of the precursor is also very fast, otherwise, there are possibilities that metallic indium could be covered by InP and spherical particles could form.[30] This formation of nanowires had not been anticipated, and an in-depth investigation was initiated.

2.7.6 Morphology and Microstructure

Figure 2.7 (A) shows selected area electron diffraction (SAED) pattern of the nanowires. The point reflections confirm the monocrystallinity of the wires. Figure 2.7 (B) shows the X-ray diffraction (XRD) of a typical sample of nanowire confirming the presence of both InP, which are the wires and indium metal, which appear as black globules at the tip of each wire. The presence of indium metal and InP also confirms the anticipated SLS growth mechanism of these wires.

Figure 2.8 shows a high-resolution TEM micrograph (HRTEM) of a typical nanowire. The <001> lattice planes are clearly visible and the distance between them corresponds with the lattice parameter of zinc blende-type InP. The <001> lattice fringes of the of the InP (zinc blende crystal structure) are well aligned and the nanowire grew apparently along its long axis (c-axis of the unit cell). The distance between 10 lattice fringes was found to be 2.9 nm, which corresponds excellently with the expected value of 2.844 nm (InP has a lattice constant of 0.5688 nm).

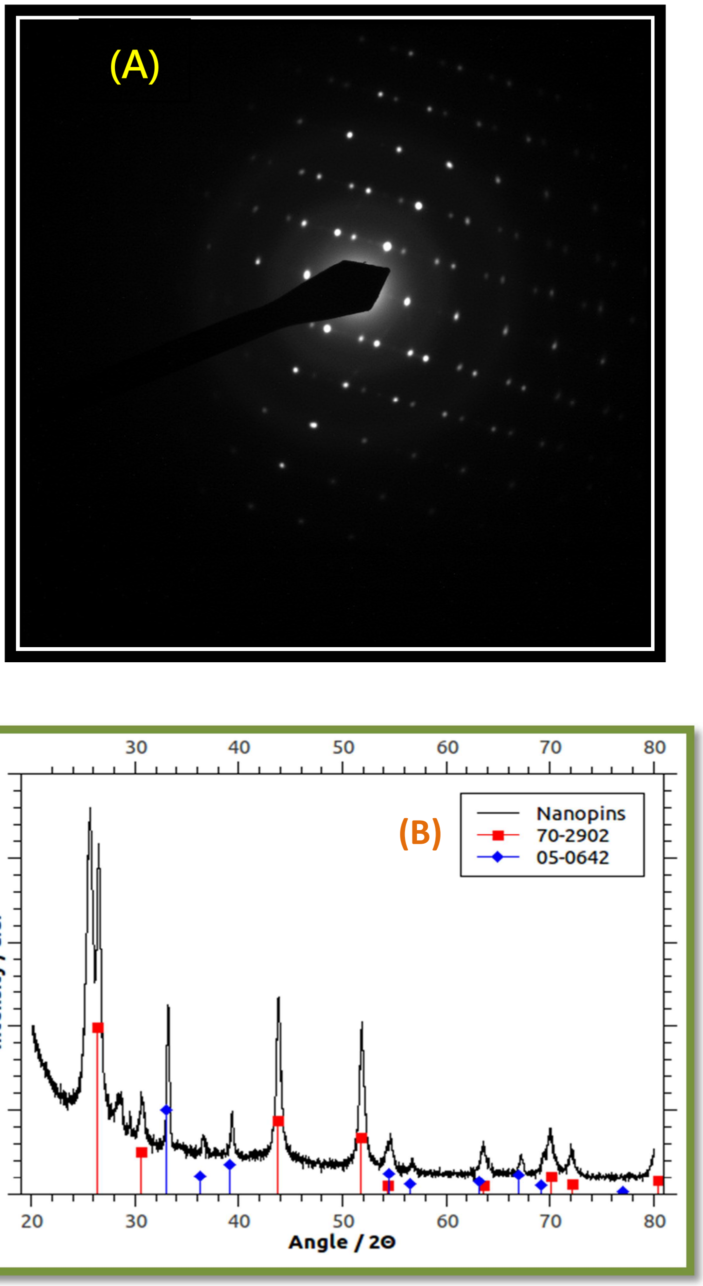

Figure 2.7. (A) Electron diffraction (SAED), (B) X-ray diffraction pattern of InP nanopins. Red: InP reflections according to card no 70-2902; Blue: In reflections according to card no. 05-0642.

There was no evidence of any oxide or amorphous surface layer. Thus, HRTEM confirms the mono-crystalline nature of the nanowires and the cubic zinc blende crystal structure.

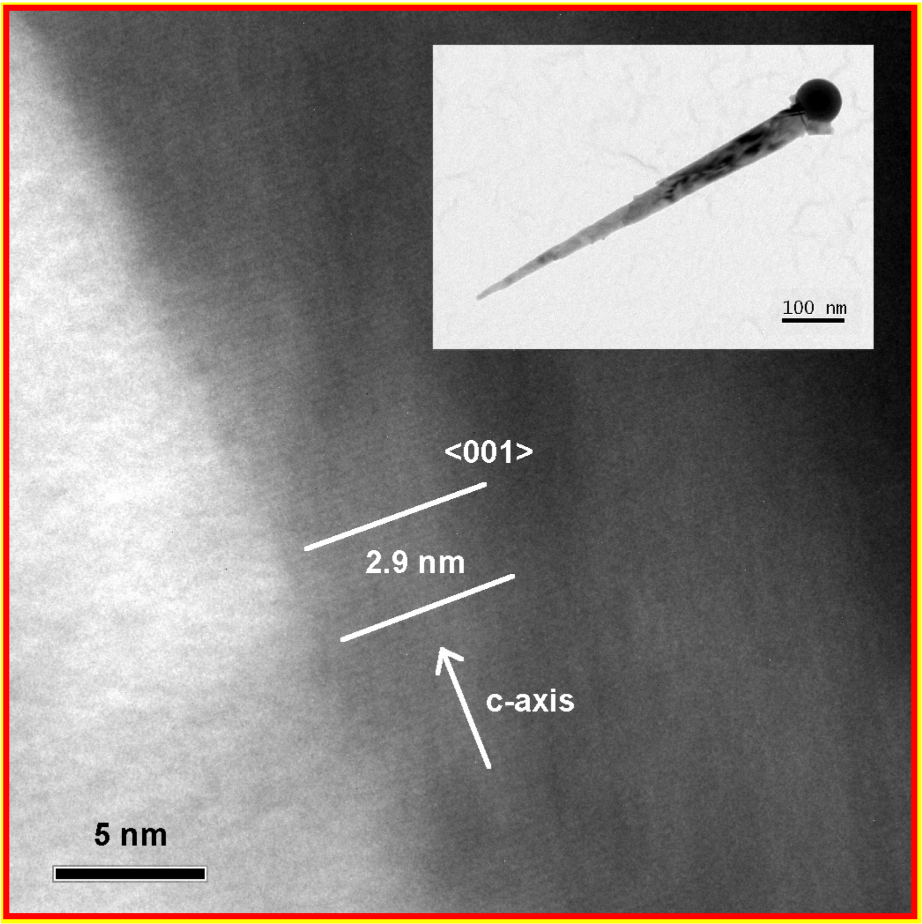

Figure 2.8. HRTEM micrograph of a single InP nanowire.

2.7.7 Mechanism of Formation of the Nanowires

Each InP nanowire obtained from the thermolysis of $[(PhCH_2)_2InP(SiMe_3)_2]_2$, was attached at one end to a small spherical globule of In metal. The formation of both InP and In^0 from the dibenzyl precursor (since no other sources for In and P were present) points to two probable decomposition pathways of the precursor under high temperature conditions – (i) the reduction of In(III) to In^0, which gives nanosized metal droplets, and (ii) the formation of indium phosphide, which grows as nanowires.

To obtain a deeper in-sight the dibenzyl precursor was subjected to thermogravimetric analysis. Thermogravimetric analysis (Figure 2.9) shows that the dibenzyl precursor incurs a 66% weight loss on heating to 210 ℃, probably due to the loss of volatiles such as $PhCH_2SiMe_3$, $PhCH_2CH_2Ph$ and $PhCH_2P(SiMe_3)_2$ (which approximate to 72 wt%), and shows that formation of InP and In^0 occurs at this temperature.

The decomposition process apparently differs from that of the analogous di-n-butyl precursor, which undergoes β-hydrogen and reductive elimination of the butyl group.[43] Under the high temperature conditions it seems likely that the indium metal can be formed from $[(PhCH_2)_2InP(SiMe_3)_2]_2$ by the reductive elimination of $PhCH_2CH_2Ph$ and

$PhCH_2P(SiMe_3)_2$, whereas, indium phosphide is formed via the dealkylsilylation route.

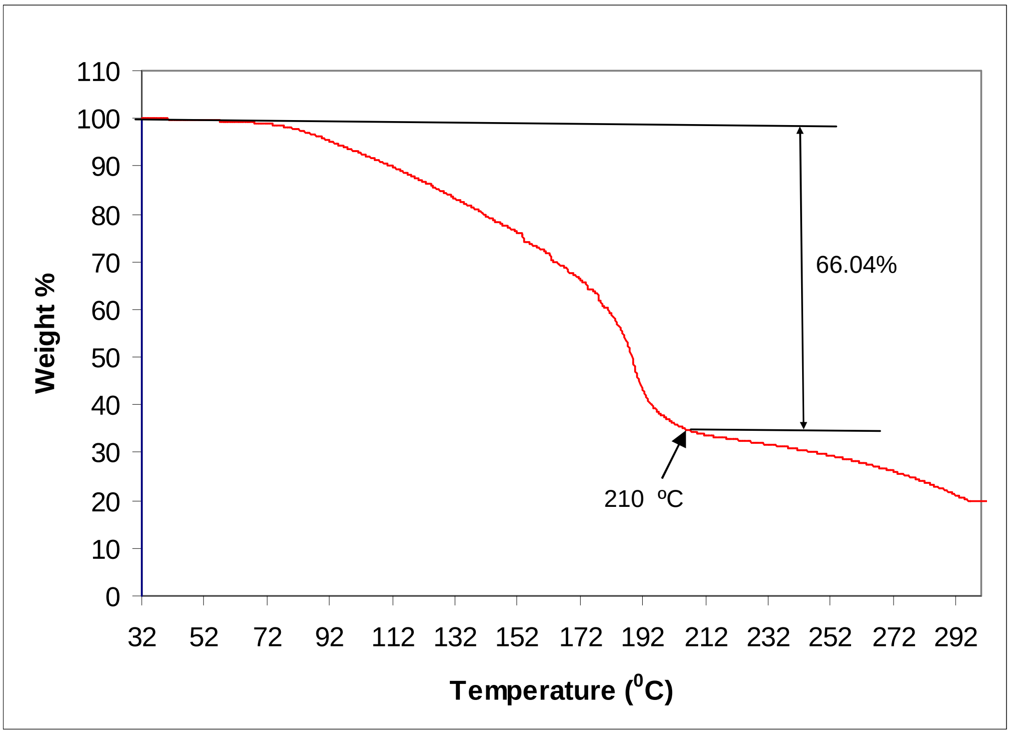

Figure 2.9. TGA diagram of $[(PhCH_2)_2InP(SiMe_3)_2]_2$; heating rate 10 °C min^{-1}(N_2 flow rate 60 cm^3/min).

In addition to the above two molecular pathways, a third non-molecular pathway called SLS mechanism (Solution-Liquid-Solid) is also in operation (Section 2.3), which is responsible for the growth of nanowires from the available InP and In^0, acting as seeds (Scheme 2.11).

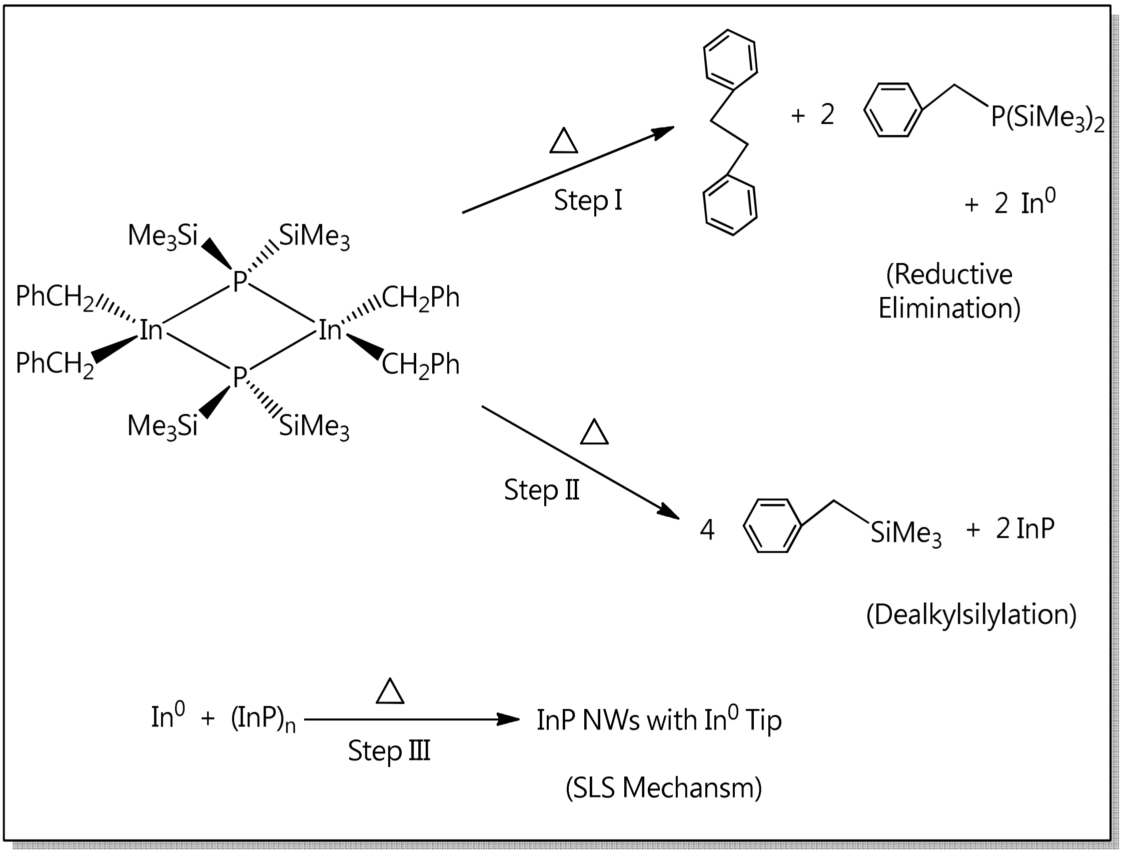

Scheme 2.11. Proposed pathways for the formation of InP nanowires.

2.7.8 Effect of Temperature on the Growth of the Nanowires

To grow the nanowires, a perfect balance between the above three steps is necessary. This can be achieved by choosing a suitable temperature regime. The dibenzyl precursor might generate indium phosphide, but if adequate numbers of In^0 seeds are not formed initially, the formation of the nanowires cannot be initiated. To find the working temperature regime, where the nanowires can be grown successfully, we started to investigate the formation of these wires at different temperatures. Since the TGA curve shows that at 210 ℃ the dibenzyl precursor is decomposed to generate both InP and In^0, we hypothesized that this should be the lowest temperature limit below which no nanowires should be formed. We repeated the same synthesis of nanowires as outlined in section 2.7.5, at an injection temperature of 210 ℃ and 200 ℃. We found that we could generate wires at 210 ℃, but no nanowires were formed at 200 ℃. This fact once again proved that In^0 formation is absolutely necessary for the formation of these wires. Furthermore, we also noticed that the wires formed at 210 ℃, were much longer than those formed at 310 ℃. This was an interesting result to us, because if the lengths of the wires vary with temperature, it would give a means to control the length of nanowires by simply altering the injection temperature. The morphology of nanowires depends on many factors, such as the concentration of the precursors, growth duration, temperature, and concentration of surfactants. Though empirical results have been published in the past showing a dependence of the diameter of nanowires on temperature,[20] to the best of our knowledge the effect of the injection temperature on the lengths of nanowires has not been systematically investigated.

We generated nanowires keeping all the reaction conditions the same, but the injection temperature. The precursor was injected at different temperatures ranging from 210-310 ℃ and the lengths of several wires were measured at each injection temperature. The average length of the wires at each temperature was then plotted against the corresponding injection temperature (Figure 2.10).

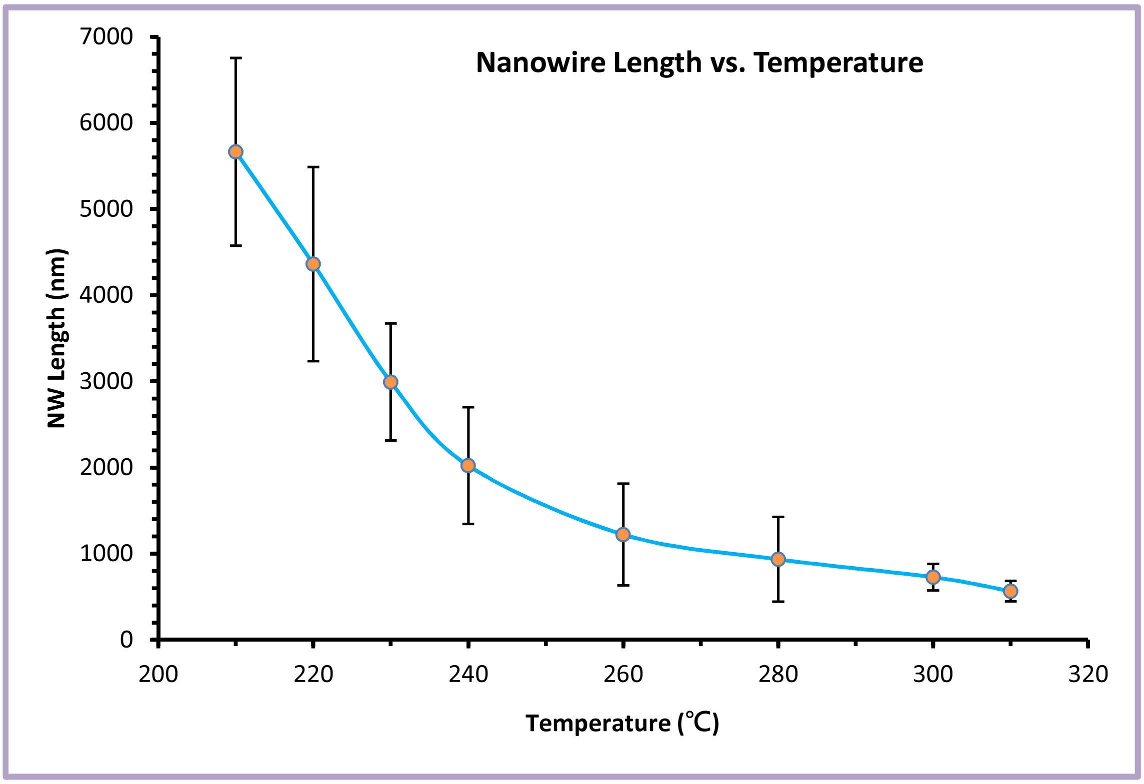

Figure 2.10. Variation of InP nanowire average lengths with injection temperature.

The graph shows that the length of the wires increases with decreasing injection temperature and below a threshold temperature (210 °C) no indium phosphide wires were formed.

As per SLS mechanism, the formation of these nanowires is catalyzed by the In^0 droplets, which are formed in-situ and act as seeds. Hence, the precursor decomposition step (Scheme 2.11, Step I), which yields the In^0 is actually the initiation step for the formation of the nanowires. A second competing step (Scheme 2.11, Step II), the formation of the InP from the precursor is also present, which provides the building material of the nanowires and is responsible for the growth of the wires. Entropically, Step I is more favored than Step II, due to an increase in the number of components in the product side. Since entropy of a system increases with an increase in temperature, Step I predominates over Step II, as the temperature rises higher. This, in other words means that, as the temperature of the system increases, the number of indium nano-droplets increases at the expense of InP formation, resulting in shorter wires being formed at higher temperature. As can be seen from the TGA curve (Figure 2.9), there is no decomposition of $[(PhCH_2)_2InP(SiMe_3)_2]_2$ below 210 °C, so either there is an insufficient number of seeds or no seeds at all to initiate the growth of the nanowires below this threshold temperature.

It was also observed that the formation of the nanowires depends on the minimum injection temperature of 210 ℃, but not on the growth temperatures. As long as the injection temperature is within the range 210-310 ℃, the wires can be grown at much lower temperature, such as 160 ℃, since sufficient seed formation has taken place, which is the limiting step in the nanowire formation. Our results show that nanowires can be obtained at a much lower temperature than previously reported (270-280 ℃).[20] The low decomposition temperature of the dibenzyl precursor and its ability to decompose in two different pathways makes the formation of the nanowires at low temperature possible. The stability of the benzyl radical might be an advantage since it facilitates reductive elimination.

Figure 2.11 shows the TEM images of the nanowires, with varied lengths, grown at three different injection temperatures viz. low (210 ℃), medium (240 ℃) and high (310 ℃). The nanowires synthesized herein, were several micrometers long (1000-6000 nm) but with a fairly constant diameter of 85-95 nm at all temperatures.

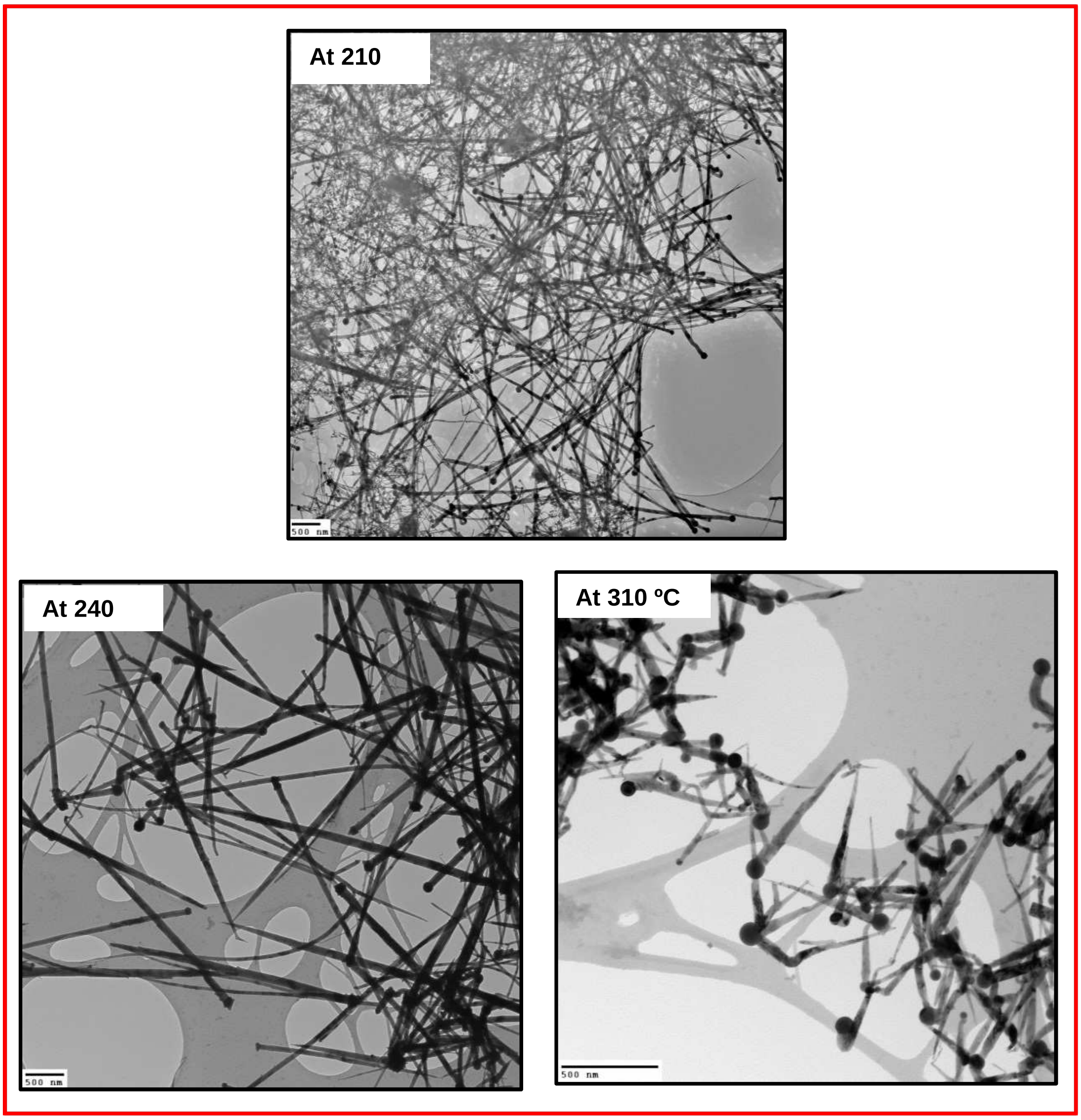

Figure 2.11. TEM micrographs of InP nanowires synthesized at injection temperatures of 210 °C, 240 °C and 310 °C.

2.7.9 Nanoparticle versus Nanowire Formation

The dibenzyl precursor is capable of producing both nanoparticle and nanowire, depending on the presence or absence of stearic acid respectively. No nanowires are formed in presence of stearic acid and no nanoparticles are formed in the absence of stearic acid. We found that stearic acid rapidly hydrolyses the In-benzyl bonds, and an indium stearate intermediate is formed, as already outlined in Section 2.7.4. The stearate intermediate cannot generate In^0 seed, thus no nanowire formation can be initiated. Instead, it does form InP by the elimination of trimethylsilyl stearate, leading to InP nanoparticles. The particles are further stabilized by the free stearic acid already present in the system. Therefore, simply by choice of presence or absence of the stearic acid, the same precursor can lead to different nanostructures.

2.7.10 Removal of the Indium Metal Tip

Presence of In^0 at the base of the nanowires has both advantages and disadvantages. The head tail morphology can be exploited to be used as electronic devices, such as Schottky diodes and Schottky transistors.[21] At the same time, the In^0 metal can act as charge acceptor and affect the physical properties of the wires. Thus depending on the final application of the wires, the presence or absence of the metal tips becomes important. Even though there are a number of reports concerning the synthesis of InP nanowires through SLS mechanisms, to the best of our knowledge removal of the metal tip has been addressed in only two instances. Buhro *et al.* used pre-formed metallic bismuth nanoparticles for nanowire growth and subsequently the Bi tip was removed through oleic acid etching.[29] Ahrenkiel *et al.* used indium metal particles as seeds to grow InP nanorods and to remove the indium tips, the samples were washed with methanol containing HF (0.5%) and further extracted by forming an alloy with mercury, however, only partial removal of the indium was achieved.[30] In both these cases, the surface of the nanorods was corroded and in the latter case, lattice fringes corresponding to left-over metallic indium were also observed.

We found that the metal tip can be conveniently removed in a one-pot reaction by utilizing the reactivity differences between InP and metallic In toward $P(SiMe_3)_3$. When $P(SiMe_3)_3$ was added to a solution of pre-formed nanowires in the presence of a P-Si hydrolyzing agent (thiophenol in this case), at a temperature well above the melting point of indium metal (m.p. 156.6 °C), the residual In metal was converted quantitatively to InP. The reducing nature of this process could also stop formation of any potential oxide layer on the wire surface. Heating the wires well above the melting point of indium is necessary for the efficient conversion of indium metal to indium phosphide under these conditions. Figure 2.12 shows the TEM micrograph of the metal-free InP nanowires. The inset image confirms that there is no indium left at the base of an individual wire. However, due to extensive washing of the wires with toluene by sonication and subsequent centrifugation, occasionally we noticed some twisting and wrinkling in the wires, which are possibly due to mechanical friction. Methanol with a lower boiling point is not suitable for use as the hydrolyzing agent and phenol was found to be acidic enough to corrode the nanowires.

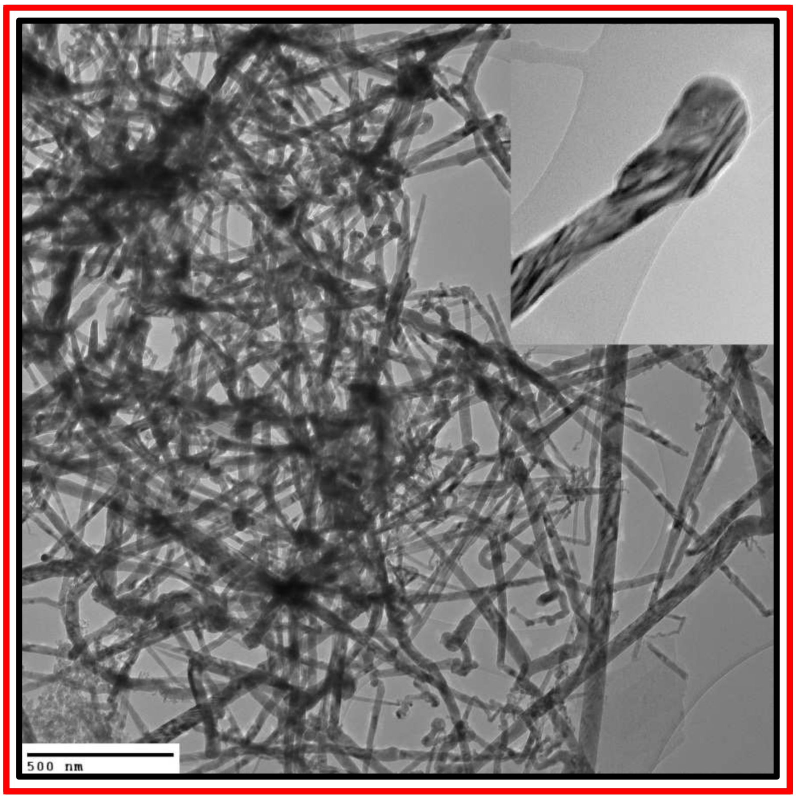

Figure 2.12. TEM image showing InP nanowires after removal of In metal particles; inset shows the indium removed base of a wire.

2.8 CONCLUSIONS

We found that the indium bis-(trimethylsilyl)phosphido compounds are efficient single molecule precursors to form InP nanostructures through thermal degradation. By contrast, indium di-tert-butylphosphido compounds always generated indium metal when subjected to thermal degradation. Thermolysis of the new dibenzyl precursor $[(PhCH_2)_2InP(SiMe_3)_2]_2$ could afford both InP nanoparticles and nanowires, depending on the presence or absence of stearic acid. The advantages of the dibenzyl precursor over other precursors reported previously, are- it can decompose at a lower temperature, generate the necessary indium metal catalyst *in situ* and also InP, through two different decomposition routes without the need of any protic reagent, and thereby, leading to a fast, simple, hazard-free synthesis of InP nanowires. The subtle balance, between the two decomposition routes of the afore-mentioned precursor with temperature, enabled us to conveniently control the length of the nanowires, for the first time, by simply varying the injection temperature (but not the growth temperature). Finally, we showed that the indium metal can be removed from the base of the wire under a mild, non-corrosive condition.

2.9 EXPERIMENTAL

2.9.1 General Procedures

Phosphorus trichloride (Aldrich, 98%), tert-butyl chloride (Aldrich, 99%), $LiAlH_4$ (Aldrich, 95%), magnesium turnings (Alfa Aesar, 99+%), n-butyl lithium (Aldrich, 1.6 M in hexane), indium chloride (Aldrich, 98%), methyl lithium (Alfa Aesar, 1-2 M in ether), zinc undecenoate or undecylenate (Aldrich, 98%), stearic acid (Aldrich, 95%), red phosphorus (Aldrich, >97%), white phosphorus (Aldrich, >99%), benzyl chloride (Alfa Aesar, 99%), chlorotrimethylsilane (Aldrich, 99%), hexadecylamine (Aldrich, 98%), diphenyl ether (Sigma-Aldrich, >99%) and methyl myristate (Aldrich, >98%) were used as received.

All reactions were carried out under dry oxygen-free nitrogen atmosphere, utilizing standard Schlenk techniques and chemicals handled in an N_2 filled dry box. Solvents were pre-dried over sodium wire and distilled under argon over sodium (toluene), sodium–potassium alloy (light petroleum, bp 40–60 °C), or sodium–benzophenone (diethyl ether, diphenyl ether-distilled at 110 °C at 0.017 mm Hg pressure). Dichloromethane was dried over calcium hydride. Methyl myristate was dried over molecular sieves and degassed by several freeze–thaw cycles. Deuterated solvents were stored over activated 4 Å molecular sieves and degassed by several freeze–thaw cycles. Other chemicals were used as received without any further purification. The concentrations of methyl lithium and Grignard reagents were determined by quenching measured aliquots by excess distilled water and titrating with 0.1 M HCl solution and phenolphthalein indicator. All compounds, except $[(PhCH_2)_2InP(SiMe_3)_2]_2$, were synthesized according to literature procedures. All spectroscopic data are in agreement with the literature values.

2.9.2 Instrumentation

^1H and ^{31}P NMR spectra were recorded using a Bruker Avance DPX300 spectrometer at ambient temperatures. ^1H NMR spectra were referenced to solvent peak at δ 7.15 for C_6D_6 and δ 5.33 for CD_2Cl_2 (δ 0.0 for Me_4Si). ^{31}P NMR referenced to external 85% H_3PO_4 (δ 0.0)-positive values are toward high frequency (downfield) in both cases.

Transmission electron microscopy (TEM) images were recorded using a JEM-2000 EX Electron Microscope (Jeol Ltd) at 200 kV; TEM samples were prepared by placing InP nanowires dispersed in dichloromethane on 300 mesh copper grids with Holey carbon films. Electron Diffraction was run using the same instrument.

Powder X-ray diffraction and high resolution TEM data were provided kindly by Prof. Thomas Nann, Ian Wark Research Institute, University of South Australia.

The single crystal X-ray diffraction study of $[(PhCH_2)_2InP(SiMe_3)_2]_2$ was carried out by Dr. David Hughes, Department of Chemistry, University of East Anglia, using an Oxford Diffraction X calibur-3/Sapphire 3-CCD diffractometer, equipped with Mo-Kα radiation and graphite monochromator.

Microwave analysis was performed in CEM Discover instrument at a pressure of 20 Bar and power 300 W, under nitrogen.

Thermogravimetric analyses were conducted using a Hi-Res TGA 2950 instrument (TA Instruments) at a heating rate of 10 °C min^{-1} and N_2 flow rate 60 cm^3/min.

UV-visible spectra were recorded on a Hitachi U-3010 spectrophotometer, using a quartz cuvette.

Steady-state photoluminescence was measured using a Perkin Elmer LS 55 fluorescence spectrometer, with a split size of 10 and excitation wavelength of 500 nm.

2.9.3 Synthesis of di-*tert*-Butyl Phosphine[44]

To a 1 L 3-neck round-bottomed flask, fitted with a reflux condenser, a liquid addition funnel and a stopper, was added freshly prepared ^tBuMgCl (1.28 M, 500 mL, 0.64 mol) in Et_2O. A mixture of PCl_3 (14.3 mL, 22.56 g, 0.16 mol) in 10 mL Et_2O was then added drop-wise to the flask while stirring. The reaction was exothermic and it started to reflux. The reflux was continued for 8 h. ^{31}P NMR was recorded with an aliquot to confirm the completion of the reaction to yield $^tBu_2PCl$.

^{31}P NMR ($CDCl_3$): δ 146.18 (Lit. value δ 146.2;[45] 147.3[46]).

The $^tBu_2PCl$ was filtered into a 3-neck 1L round-bottomed flask, fitted with a reflux condenser. $LiAlH_4$ (6.24 g, 0.16 mol) was then added slowly into the flask with stirring and it started to reflux. The stirring was continued for 3 h. The solution was filtered and the solid was washed three times with dry ether (3 x 20 mL) and the washings combined with the filtrate. Ether was distilled off under N_2. The final product, which is a colorless liquid, was collected by distillation under reduced pressure. The NMR spectrum showed the presence of small amounts of residual ether. The ^{t}butyl protons show a prominent and intense doublet, but the P-H peak was sometimes masked by the $–CH_2$ peak of the ether.

Yield: 15.02 g (0.1 mol, 62.53%); ^{1}H NMR (C_6D_6): δ 1.16 (d, 18 H), 3.16 (d P-H) (Lit. value δ 1.16, 3.14[47]) ^{31}P NMR (C_6D_6): δ 19.63 (lit. value δ 19.9[47,48]).

2.9.4 Synthesis of ^{t}Bu$_2$PLi[49]

To a 250 mL 3-neck round-bottomed flask, fitted with a liquid addition funnel and a reflux condenser, was added a solution of ^{t}Bu$_2$PH (15 g, 0.103 mol) in 10 mL of dry light petroleum. Then, a mixture of 65 mL of 1.6 M freshly titrated ^{n}BuLi (0.103 mol) in 100 mL of dry light petroleum was added drop-wise. The contents were heated to reflux for *ca*. 8 h to form a yellow precipitate of the product. The volatiles were then removed under vacuum and the yellow powdery residue was washed three times with dry petroleum ether (3 x 10 mL), filtered, and dried under vacuum.

Yield: 15.9 g (0.1 mol, 63.6%); ^{31}P NMR (C_6D_6): δ 35.05 (Lit. value unavailable).

2.9.5 Synthesis of $[Me_2In(\mu\text{-}{}^tBu_2P)]_2$[40]

To a 100 mL 2-neck round-bottomed flask, containing 15 mL of dry ether, was added $InCl_3$ (0.78 g, 3.47 mmol) and the contents cooled to -78 ℃. Next, freshly titrated MeLi (1.8 M, 3.7 mL, 6.74 mmol) was added to the flask while stirring and the mixture was again cooled to -78 ℃. Then a solution of ${}^tBu_2PLi$ (0.51 g, 3.37 mmol) dissolved in 2.5 mL of dry THF was added to the flask while stirring. The mixture was left at -78 ℃ for 1h and then allowed to warm up slowly to room temperature with stirring, when a grey colored precipitate formed. Next all the volatiles were removed under vacuum and the residue dried. The product was extracted three times with hot (80 ℃) dry toluene (3 x 15 mL) through filtration. The combined filtrate was reduced to ~20 mL and saved for crystallization at -25 ℃ for 1 day. The product was obtained as small colorless crystals.

Yield: 0.48 g (0.83 mmol, 46.8%); ^1H NMR (C_6D_6): δ 0.29 (s, 12 H), 1.30 (t, 36 H) (Lit. value δ 0.29, 1.30[40]); ^{31}P NMR (C_6D_6): δ 39.02 (lit. value δ 39.24[40]).

2.9.6 Synthesis of $[(PhCH_2)_2In(\mu\text{-}^tBu_2P)]_2$[41]

To a 100 mL 2-neck round-bottomed flask containing 15 mL of dry ether, was added $InCl_3$ (0.88 g, 3.96 mmol) and the contents was cooled to -78 °C. A solution of $^tBu_2PLi$ (0.60 g, 3.96 mmol) in 8.5 mL of dry THF was added to the flask while stirring. The mixture was again cooled to -78 °C and freshly prepared $PhCH_2MgCl$ in Et_2O (0.86 M, 9.2 mL, 7.92 mmol) was added to the flask. The flask was allowed to warm slowly to room temperature with stirring and a grey colored precipitate formed. The solvent was then removed under vacuum and the precipitate dried. The product was extracted with dry toluene (3 x 20 mL) and filtered to give a yellow filtrate. Toluene and other volatiles were removed under vacuum, leaving a yellow gummy solid. Next, the residue was dissolved in warm toluene (~45 °C) and left to recrystallize at -25 °C for a day. The product was obtained as small colorless crystals.

Yield: 0.86 g (0.97 mmol, 48.9%); ^1H NMR (C_6D_6): δ 2.6 (s, 8 H), 1.12 (t, 36 H), 6.8-7.2 (m, 20H aromatic) (Lit. values δ 2.62, 1.12, 6.8-7.5[41]); ^{31}P NMR (C_6D_6): δ 60.84 (Lit. value δ 60.84[41]).

2.9.7 Synthesis of $P(SiMe_3)_3$[50]

$P(SiMe_3)_3$ was synthesized both from white and red phosphorus.

(a) From White Phosphorus -

Naphthalene (12.8 g, 0.1 mol) and 1 L THF were placed in a 2 liter 3-neck flask, fitted with a stirrer, reflux condenser and a dropping funnel. Then, sodium (2.3 g, 0.1 mol) was added and dissolved with vigorous stirring, followed by addition of white phosphorus (31 g, 0.25 mol). The mixture was heated to 50 °C. Next sodium (67.7 g, 2.9 mol) was added in portions of 3 g every 20-25 min for the complete formation of the black Na_3P. The suspension was stirred for 2 h at 50 °C and then cooled to room temperature. The mixture turned black, indicating the formation of Na_3P. The solvent, along with any excess naphthalene, was filtered off. The black solid was washed with light petroleum (2 x 250 mL) and dried under vacuum. Then 1 L of 1,2-dimethoxyethane was added to the solid with stirring to form a suspension, followed by a drop-wise addition of freshly distilled chlorotrimethylsilane (390 mL, 336.8 g, 3.1 mol), through the dropping funnel over a period of 3 h with stirring. During this time the color changed from black to grey or white. The dropping funnel was replaced by a stopper and the contents was heated to reflux for 6 h. Filtration left NaCl which was washed with 250 mL of light petroleum. The washing was combined with the filtrate. The solvent was distilled off under nitrogen and the final product purified by distillation at 65 °C at 0.017 mm Hg pressure.

Yield: 150 g (0.6 mol, 60%); ^{31}P NMR (C_6D_6): -252 (Lit. value δ -251.89[50]).

(b) From Red Phosphorus -

Both potassium (5.43 g, 0.139 mol) and sodium (4.28 g, 0.186 mol) were placed in a 2-neck 1 L flask, equipped with a reflux condenser and a liquid addition funnel. The two metals were heated under nitrogen atmosphere to melt and form an alloy. To this was added dry 1,2-dimethoxyethane (400 mL) and the mixture was heated to reflux for 2 h with stirring, during which time the color turned purple. After cooling the flask to room temperature, red phosphorus (3.35 g, 0.108 mol) was added to it and the mixture was again heated to reflux for 24 h during which the color turned black due to the formation of $(Na/K)_3P$. The suspension was cooled to room temperature and chlorotrimethylsilane (45 mL, 0.358 mol) was added to the vigorously stirred solution over 1 h from the dropping funnel. During the course of the reaction a grey solid formed, which was filtered off. The solid was washed with 200 mL light petroleum and the washing combined with the filtrate. The solvent was removed at room temperature under vacuum and the product was purified by distillation at 65 °C at 0.017 mm Hg pressure.

Yield: 13.4 g (0.053 mol, 50%); ^1H NMR (C_6D_6): δ 0.28 (d, $^3J_{H,P}$ 3.0 Hz, 27 H) (Lit. value δ 0.27[50]); ^{31}P NMR (C_6D_6): δ -252 (Lit. value δ -251.89[50]).

2.9.9 Synthesis of $[Me_2InP(SiMe_3)_2]_2$[25,42]

Step (a) -

To a 100 mL 2-neck round-bottomed flask, attached with a reflux condenser and a septum, were added 50 mL of dry ether and $InCl_3$ (3.04 g, 13.7 mmol). Then freshly titrated MeLi (1.6 M, 17.2 mL, 27.5 mmol) was added to the flask slowly with stirring. The ether started to reflux and a curdy white precipitate was observed to form. The stirring was continued vigorously for two days under a flow of N_2. All the volatiles were then removed under vacuum. The white residue was dried and sublimed at 110 -120 ℃ (0.017 mm Hg) to yield 1.32 g of Me_2InCl.

^1H NMR (C_6D_6): δ 0.2885 (s, 6 H) (Lit. value δ 0.28[51]) .

Step (b) -

In a 100 mL 2-neck round-bottomed flask equipped with a reflux condenser and a septum was added dry toluene (55 mL) and Me_2InCl (1.32 g, 7.3 mmol). Next, $P(SiMe_3)_3$ (2.1 mL, 1.83 g, 7.3 mmol) was added to it drop-wise at room temperature with stirring, and the contents were then heated to reflux for 8 h. After cooling the flask to room temperature, the volatiles were removed under vacuum, leaving a white residue. The product was extracted with light petroleum (4 x 10 mL) and filtered. The volume of the filtrate was reduced to ~20 mL. The solution was left to crystallize at -25 °C overnight. Small colorless cubic crystals were obtained.

Yield: 0.54 g (0.84 mmol, 41%); ^{1}H NMR (C_6D_6): δ 0.2550 (s, 12 H), 0.37 (t, 36 H) (Lit. value δ 0.22, 0.34[25]) ; ^{31}P NMR (C_6D_6): δ -239.68 (Lit. value δ -239.8[25]).

2.9.10 Synthesis of $[(PhCH_2)_2InP(SiMe_3)_2]_2$

In a 100 mL 2-neck round-bottom flask, $InCl_3$ (1.52 g, 6.86 mmol) in 50 mL dry ether cooled to -78 °C was treated with freshly prepared $PhCH_2MgCl$ (1.14 M, 12.04 mL, 13.7 mmol). The mixture was then allowed to warm slowly to room temperature and stirred. A white precipitate formed. The solvent was removed under vacuum and the precipitate dried. Then 50 mL of dry toluene and 2 mL of $P(SiMe_3)_3$ (1.72 g, 6.87 mmol) were added to the precipitate and the mixture was heated to reflux for 8 h, during which time the color of the mixture turned pale yellow. Removal of volatiles under vacuum afforded a pale yellow precipitate, which was extracted with dry toluene (4 x 20 mL). The combined extracts were reduced to ~15 mL, which on cooling to -25 ℃ gave large colorless crystals of the product.

Yield: 1.42 g (43.7%); m.p. 209 ℃ (decomp); ^{1}H NMR (300 MHz, CD_2Cl_2): δ 7.07 (m, 4H, m-Ph), 6.87 (m, 6H, o- and p-Ph), 2.33 (s, 4H, CH_2), 0.32 (t, 18H, $SiMe_3$, J_{HP} = 5.6 Hz); $^{13}C\{^1H\}$ NMR (CD_2 Cl_2 , 75.5 MHz): δ 146.27 (Ph, ipso-C), 129.46, 128.68 (Ph, o-C, m-C), 122.72 (Ph, p-C), 25.75 (t, J_{CP} = 17.4 Hz, CH_2), 4.58 (t, J_{CP} = 9.3 Hz, $SiMe_3$); ^{31}P NMR (121.5 Hz, CD_2Cl_2): δ −220.3. Anal. Found: C, 51.05; H, 7.06. Calcd for $C_{20}H_{32}InPSi_2$: C, 50.63; H, 6.80%.

2.9.11 Synthesis of InP NPs from $[(PhCH_2)_2InP(SiMe_3)_2]_2$ by the Hot Injection Method

All operations were carried out under dry N_2. The weight measurements are within ±0.5 mg.

To a 100 mL 3-neck round-bottom flask, equipped with a reflux condenser, septum and a temperature probe, were added stearic acid (85.5 mg, 0.3 mmol) and zinc undecenoate (43.3 mg, 0.1 mmol). The flask was evacuated and filled with N_2 3-5 times to ensure complete removal of oxygen and moisture. Then 10 mL of 1-octadecene was placed into the flask and the mixture heated to 310 ℃ using a temperature-controlled heating mantle. At 310 ℃, 1.6 mL of 0.02 M solution of $[(PhCH_2)_2InP(SiMe_3)_2]_2$ (0.03 mmol w.r.t. indium) in diphenyl ether was very rapidly injected , with vigorous stirring. Instantly the solution turned orange and the temperature dropped to 250 ℃. The solution was further stirred for 10 min at 250 ℃. The flask was then air-cooled to room temperature. The solution was yellowish in color and showed an orange luminescence under a UV lamp.

2.9.12 A Representative Procedure for the Synthesis of InP Nanowires

All operations were conducted under dry nitrogen. The weight measurements are within ±0.5 mg.

A 3-neck 100 mL flask, equipped with a reflux condenser, septum and a temperature probe was charged with 10 mL of methyl myristate and the contents heated to 310 ℃ using a temperature-controlled heating mantle. At 310 ℃, a solution of $[(PhCH_2)_2InP(SiMe_3)_2]_2$ (1.6 mL of 0.02 M, 0.03 mmol w.r.t. indium) in diphenyl ether was injected as quickly as possible into the flask, with vigorous stirring. Instantly a black precipitate was formed. The temperature was immediately set to 250 ℃

by the temperature control. The solution was stirred for 10 min at 250 ℃ and then cooled to room temperature. For injection temperatures below 250 ℃, the growth temperature was kept constant at 160 ℃ for all samples. The black precipitate was centrifuged, washed with toluene (3 x 5 mL) and dispersed in 3 mL dichloromethane for TEM imaging.

2.9.13 Removal of the Indium Metal Tip

All operations were conducted under dry nitrogen. The nanowires synthesized as above were dispersed in 10 mL of methyl myristate and placed into a 100 mL 3-neck round bottom flask, equipped with a reflux condenser, septum and a temperature probe. To this was added $P(SiMe_3)_3$ (1 mL, 0.86 g, 3.43 mmol) and the mixture heated to 250 ℃ by a temperature-controlled heating mantle. Then thiophenol (1.1 mL, 10.3 mmol) was injected and the mixture was kept at 250 ℃ for 30 min with continuous stirring. After cooling to room temperature the black precipitate was centrifuged, washed with toluene (5 x 4 mL) and dispersed in 3 mL dichloromethane for subsequent TEM analysis.

Publication from Chapter 2: Banerjee, C.; Hughes, D.L.; Bochmann, M.; Nann, T. *Dalton Trans.* **2012**, *41*, 7244.

REFERENCES

(1) Duan, X.; Huang, Y.; Cui, Y.; Wang, J.; Lieber, C. M. *Nature* **2001**, *409*, 66–69.

(2) Wang, J.; Gudiksen, M. S.; Duan, X.; Cui, Y.; Lieber, C. M. *Science* **2001**, *293*, 1455–1457.

(3) Gudiksen, M. S.; Lauhon, L. J.; Wang, J.; Smith, D. C.; Lieber, C. M. *Nature* **2002**, *415*, 617–620.

(4) Duan, X.; Niu, C.; Sahi, V.; Chen, J.; Parce, J. W.; Empedocles, S.; Goldman, J. L. *Nature* **2003**, *425*, 274–278.

(5) Nilsson, H. A.; Thelander, C.; Fröberg, L. E.; Wagner, J. B.; Samuelson, L. *Appl. Phys. Lett.* **2006**, *89*, 163101–163101–3.

(6) Lucey, D. W.; MacRae, D. J.; Furis, M.; Sahoo, Y.; Cartwright, A. N.; Prasad, P. N. *Chem. Mater.* **2005**, *17*, 3754–3762.

(7) Xu, S.; Ziegler, J.; Nann, T. *J. Mater. Chem.* **2008**, *18*, 2653.

(8) Banerjee, C.; Hughes, D. L.; Bochmann, M.; Nann, T. *Dalton Trans.* **2012**, *41*, 7244.

(9) Trentler, T. J.; Hickman, K. M.; Goel, S. C.; Viano, A. M.; Gibbons, P. C.; Buhro, W. E. *Science* **1995**, *270*, 1791–1794.

(10) Agger, J. R.; Anderson, M. W.; Pemble, M. E.; Terasaki, O.; Nozue, Y. *J. Phys. Chem. B* **1998**, *102*, 3345–3353.

(11) Qian, Y. *Adv. Mater.* **1999**, *11*, 1101–1102.

(12) Wells, R. L.; Pitt, C. G.; McPhail, A. T.; Purdy, A. P.; Shafieezad, S.; Hallock, R. B. *Chem. Mater.* **1989**, *1*, 4–6.

(13) Healy, M. D.; Laibinis, P. E.; Stupik, P. D.; Barron, A. R. *J. Chem. Soc., Chem. Commun.* **1989**, 359–360.

(14) Micic, O. I.; Curtis, C. J.; Jones, K. M.; Sprague, J. R.; Nozik, A. J. *J. Phys. Chem.* **1994**, *98*, 4966–4969.

(15) Guzelian, A. A.; Katari, J. E. B.; Kadavanich, A. V.; Banin, U.; Hamad, K.; Juban, E.; Alivisatos, A. P.; Wolters, R. H.; Arnold, C. C.; Heath, J. R. *J. Phys. Chem.* **1996**, *100*, 7212–7219.

(16) Yan, P.; Xie, Y.; Wang, W.; Liu, F.; Qian, Y. *J. Mater. Chem.* **1999**, *9*, 1831–1833.

(17) Battaglia, D.; Peng, X. *Nano Lett.* **2002**, *2*, 1027–1030.

(18) Gerbec, J. A.; Magana, D.; Washington, A.; Strouse, G. F. *J. Am. Chem. Soc.* **2005**, *127*, 15791–15800.

(19) Xu, S.; Kumar, S.; Nann, T. *J. Am. Chem. Soc.* **2006**, *128*, 1054–1055.

(20) Liu, Z.; Sun, K.; Jian, W.-B.; Xu, D.; Lin, Y.-F.; Fang, J. *Chem. Eur. J.* **2009**, *15*, 4546–4552.

(21) Strupeit, T.; Klinke, C.; Kornowski, A.; Weller, H. *ACS Nano* **2009**, *3*, 668–672.

(22) Green, M.; O′ Brien, P. *Chem. Commun.* **1998**, 2459–2460.

(23) Green, M.; O′ Brien, P. *J. Mater. Chem.* **2004**, *14*, 629.

(24) Andrews, D. A.; Davies, G. J.; Bradley, D. C.; Faktor, M. M.; Frigo, D. M.; White, E. A. D. *Semicond. Sci. Technol.* **1988**, *3*, 1053–1056.

(25) Stuczynski, S. M.; Opila, R. L.; Marsh, P.; Brennan, J. G.; Steigerwald, M. L. *Chem. Mater.* **1991**, *3*, 379–381.

(26) Trentler, T. J.; Goel, S. C.; Hickman, K. M.; Viano, A. M.; Chiang, M. Y.; Beatty, A. M.; Gibbons, P. C.; Buhro, W. E. *J. Am. Chem. Soc.* **1997**, *119*, 2172–2181.

(27) Nedeljković, J. M.; Mićić, O. I.; Ahrenkiel, S. P.; Miedaner, A.; Nozik, A. J. *J. Am. Chem. Soc.* **2004**, *126*, 2632–2639.

(28) Yu, H.; Li, J.; Loomis, R. A.; Wang, L.-W.; Buhro, W. E. *Nat. Mater.* **2003**, *2*, 517–520.

(29) Wang, F.; Buhro, W. E. *J. Am. Chem. Soc.* **2007**, *129*, 14381–14387.

(30) Ahrenkiel, S. P.; Mićić, O. I.; Miedaner, A.; Curtis, C. J.; Nedeljković, J. M.; Nozik, A. J. *Nano Lett.* **2003**, *3*, 833–837.

(31) Woo, R. L.; Gao, L.; Goel, N.; Hudait, M. K.; Wang, K. L.; Kodambaka, S.; Hicks, R. F. *Nano Lett.* **2009**, *9*, 2207–2211.

(32) Wagner, R. S.; Ellis, W. C. *Appl. Phys. Lett.* **1964**, *4*, 89–90.

(33) Duan, X.; Lieber, C. M. *J. Am. Chem. Soc.* **2000**, *122*, 188–189.

(34) Morales, A. M.; Lieber, C. M. *Science* **1998**, *279*, 208–211.

(35) Zhang, R.-Q.; Lifshitz, Y.; Lee, S.-T. *Adv. Mater.* **2003**, *15*, 635–640.

(36) Shi, W. S.; Zheng, Y. F.; Wang, N.; Lee, C. S.; Lee, S. T. *Appl. Phys. Lett.* **2001**, *78*, 3304–3306.

(37) Han, W.; Fan, S.; Li, Q.; Hu, Y. *Science* **1997**, *277*, 1287–1289.

(38) Berry, A. D.; Tonucci, R. J.; Fatemi, M. *Appl. Phys. Lett.* **1996**, *69*, 2846–2848.

(39) Bradley, D. C.; Faktor, M. M.; Scott, M.; White, E. A. D. *J. Crys. Growth* **1986**, *75*, 101–106.

(40) Arif, A. M.; Benac, B., L.; Cowley, A. H.; Jones, R. A.; Kidd, K. B.; Nunn, C. M. *New J. Chem.* **1988**, *12*, 553–557.

(41) Culp, R. D.; Cowley, A. H.; Decken, A.; Jones, R. A.; Bond, M. R.; Mokry, L. M.; Carrano, C. J. *Inorg. Chem.* **1997**, *36*, 5165–5172.

(42) Clark, H. C.; Pickard, A. L. *J. Organometal. Chem.* **1967**, *8*, 427–434.

(43) Barry, S. T.; Belhumeur, S.; Richeson, D. S. *Organometallics* **1997**, *16*, 3588–3592.

(44) Hoffmann, H.; Schellenbeck, P. *Chem. Ber.* **1966**, *99*, 1134–1142.

(45) Eisenträger, F.; Göthlich, A.; Gruber, I.; Heiss, H.; Kiener, C. A.; Krüger, C.; Notheis, J. U.; Rominger, F.; Scherhag, G.; Schultz, M.; Straub, B. F.; Volland, M. A. O.; Hofmann, P. *New J. Chem.* **2003**, *27*, 540–550.

(46) Naiini, A. A.; Han, Y.; Akinc, M.; Verkade, J. G. *Inorg. Chem.* **1993**, *32*, 5394–5395.

(47) Beachley, O. T.; Chao, S. H. L.; Churchill, M. R.; Lake, C. H. *Organometallics* **1993**, *12*, 3992–3997.

(48) Rithner, C. D.; Bushweller, C. H. *J. Am. Chem. Soc.* **1985**, *107*, 7823–7836.

(49) Issleib, K.; Krech, F. *J. Organometal. Chem.* **1968**, *13*, 283–289.

(50) Karsch, H. H.; Bienlein, F.; Rupprich, T.; Uhlig, F.; Herrmann, E.; Scheer, M. *Synthetic Methods of Organometallic and Inorganic Chemistry*, W.A. Herrmann, Thieme, Stuttgart.; 1996; Vol. 3, Pages 59-65.

(51) Hobbs, C. W.; Tobias, R. S. *Inorg. Chem.* **1970**, *9*, 1998–2004.

CHAPTER 3 SYNTHESES & CHARACTERIZATIONS OF II-VI SEMICONDUCTOR QUANTUM DOTS

3.1 INTRODUCTION

The II-VI semiconductor quantum dots are of great fundamental and technical interest, due to their novel size-dependent properties, excellent chemical processibilities and wide-range of applications. They had been used in solar cells,[1] sensors,[2] light-emitting devices,[3] as a photo-sensitizer,[4] and biological imaging.[5] A large volume of research had been devoted to the syntheses of II-VI nanocrystals such as, CdSe, ZnSe, CdS, ZnS, ZnO. Among these, most of the studies on physical and optical properties have been carried out on CdSe, which has become a model compound. ZnSe also gained interest as a replacement material to toxic Cd-containing quantum dots, as a good shell material due to its wide band gap (bulk band gap 2.7 eV)[6] and as a UV-blue region emitter for opto-electronic devices.[7]

Our interest with respect to these II-VI quantum dots lies in building a hetero nano-composite structure through coupling of ZnSe or CdSe quantum dots with the cup-shaped subphthalocyanine molecules. Although several organic molecules have been previously used in conjunction with quantum dots, no attempts have been made so far to attach subphthalocyanines to the nanoparticles. The formation, energy transfer and photo-physics of these subphthalocyanine-quantum dot composites will be further dealt with in details in the following chapter.

In this chapter, the syntheses and characterizations of ZnSe and CdSe nanoparticles are described. Mainly two differently sized CdSe particles are synthesized to bind to the subphthalocyanine - the smaller size (*ca.* 2.68 nm) called Green QD (GQD) luminesce with a green color under UV illumination and the larger size (*ca.* 3 nm) called Orange QD (OQD) shows orange luminescence under UV light. ZnSe particles synthesized are *ca.* 3 nm and show a blue luminescence. The roles of different reaction conditions are discussed and finally a modified synthetic recipe is presented. The detailed experimental procedures have been provided at the end of this chapter.

3.2 REACTION PARAMETERS FOR THE SYNTHESES OF QUANTUM DOTS

The syntheses of nanocrystals largely depend on several factors, viz. solvent, temperatures of precursor injection and of nanoparticle growth, type and concentration ratios of precursors, types of surfactants, and duration of the crystal growth phase. This section briefly introduces the role of these parameters, the knowledge of which is necessary to optimize a synthetic procedure.

3.2.1 Solvent

The choice of an appropriate solvent is crucial in the syntheses of nanocrystals. Solvents have pronounced effect on the formation and stability of the nanoparticle systems since they can influence the dispersion and reactivity of the precursors and any intermediates and control the coordinating environment of the nanoparticles. Solvents can affect the nucleation and growth rates, stability and shape of the nanocrystals.

Solvents can be coordinating or non-coordinating type. The coordinating solvents such as TOPO,[8] HDA[9] can bind to the crystal surface and prevent any agglomeration of the particles, thereby, stabilizing the colloidal solution.[10] However, the number of such coordinating solvents, with high b.p. and high thermal stability is limited. Thus, it becomes quite challenging to identify a suitable reaction system to grow high quality nanoparticles. Moreover, strongly coordinating solvents lead to a slower nucleation process and can make it difficult to separate the nucleation and the growth phases.[11] In contrast, stable non-coordinating solvents, such as, ODE or paraffin oil do not bind to the nanocrystals and are ideal to study the effect of ligands or investigate the reaction kinetics.[12] Yu *et al.* showed that II-VI nanoparticles can also be synthesized in a non-coordinating solvent, provided that a suitable amount of stabilizing agent is present.[13] Moreover, by changing the concentration of the stabilizing agent, it is possible to tune the nanocrystal growth rate and control the polydispersity of the particle size.[13,14]

3.2.2 Temperature

The most important parameter in the synthesis of high quality nanocrystals is probably the synthesis temperature. By a sophisticated control of the reaction temperature, one can control the nucleation/growth rate, the size/size distribution of the nanoparticles, the reactivity of the precursor molecules and the crystal structure/defects in a nanocrystal.

Nucleation has a higher activation barrier than the growth and is kinetically favored at high temperature.[12,15] Consequently, higher temperature should produce more nuclei, resulting in smaller particles (provided coagulation and Ostwald ripening are not accelerated at higher temperature).[12,16] Elevated temperatures also favor faster monomer diffusion, thereby fostering a faster crystal growth.[17] Since Ostwald ripening increases with temperature,[18] in the current research nanoparticles were grown at a lower temperature than the nucleation temperature, through the hot injection technique. High temperature also minimizes the surface defects of the nanocrystals. The smaller the particle size, the higher is the probability of defects because of high surface-to-volume ratio.[19] At an elevated temperature, atoms and molecules gain thermal energy and can reshuffle themselves to fill up vacant sites and surface reconstruction takes place, minimizing defects.

3.2.3 Precursors

Numerous approaches have been reported for the syntheses of CdSe and ZnSe nanocrystals to-date, which include a wide variety of precursors and surfactants. In the early 90s, one of the most established non-aqueous synthetic routes toward high quality CdSe, was the reaction of the organometallic compound, $Cd(CH_3)_2$ with TOPSe or $(TMS)_2Se$ in TOP/TOPO at an elevated temperatures.[8] However, further developments in the II-VI nanocrystal syntheses, have led to the replacement of the toxic, pyrophoric and expensive $Cd(CH_3)_2$, with CdO,[20]

$Cd(CO_3)_2$ or cadmium carboxylates.[21] Liu *et al.* have shown that cadmium stearate can also form CdSe when reacted with TBPSe in ODE at high temperature.[22] The same principle can be further extended for the formation of ZnSe nanocrystals also. Zinc carboxylates are more stable than the corresponding cadmium carboxylate salts, and thus can be used as a precursor for ZnSe nanoparticles, which require a high temperature synthesis.[23] A wide variety of sources of selenium such as selenourea,[24,25] TOPSe,[22,26] ODE-Se,[27,28] olive oil-Se[29], TBPSe[19,30] have also been reported.

3.2.4 Surfactants

Surfactants play a vital role in stabilizing a nanoparticle system and also help to maintain their luminescence efficiency. They are generally long-chain organic molecules (such as fatty acids and aliphatic amines), with donating groups, which can bind to nanoparticle surfaces. Due to their high surface energy, the particles have an inherent tendency to fuse together and form larger aggregates. Surfactants reduce the surface energy, thereby, stopping coagulation and imparting stability to the colloidal solution. By reducing any dangling bond and through surface passivation, the surfactants also increase quantum efficiency of the nanocrystals. Additionally, the long chains of the surfactants improve the solubility of the particles and the electron donation group can also protect particles from any aerial oxidation. It was Peng’ s group, who first reported, the role of amines is to activate the carboxylate precursors.[23] They found that in the absence of amine, the formation of ZnSe did not occur within the first 10 min, whereas, with amine it was instantaneous, but they did not provide any detail mechanism for this.

3.2.5 Growth Time

Generally the size of a particle is directly proportional to the reaction or growth time. After the rapid nucleation burst, the addition of monomers to the tiny nuclei continues throughout the growth phase and the nanocrystals keep growing in size. The smaller particles grow faster, whereas, the larger ones slower, leading to a slow focusing of size. This focusing takes place up to a certain time, followed by a defocusing, which is due to the Ostwald ripening.

3.3 RESULTS AND DISCUSSIONS

With a theoretical understanding of the important roles of the above mentioned parameters, we tried to make the best possible combination of these conditions, which would eventually converge to an optimized recipe within our experimental set up and hands.

3.3.1 Choice of Solvent

Two non-coordinating solvents were tested, viz. ODE and paraffin oil. Synthesis of zinc selenide quantum dots requires a very high injection temperature (~320-330 ℃). We have found that with pure ODE (b.p. 310-315 ℃) it was not possible to reach the target injection temperature. Peng *et al.* added a large amount of tetracosane to ODE to reach a temperature of 330 ℃.[23] Tetracosane is a solid at room temperature, hence, difficult to remove from the solvent after synthesis.[31] Additionally, the rubber septum, attached to the 3-neck reaction flask gets attacked by hot ODE and contaminates the reaction mixture.

If the growth of the nanoparticles can be stopped instantaneously, size and size distribution can be controlled. This is generally done by injecting ice-cold solvent to the hot reaction flask very rapidly, which brings down the temperature. Since ODE freezes at 17-18 ℃, ice-cold ODE cannot be used. Due to all these difficulties with ODE, paraffin oil was finally chosen as the preferred solvent for the syntheses of both ZnSe and CdSe nanoparticles. Paraffin oil is inexpensive, environmentalfriendly and allows easy isolation and purification of nanocrystals, which are relatively monodisperse in size.

3.3.2 Choice of Temperature

In the current work, the injection/growth temperatures found to be suitable for the growth of ZnSe and CdSe nanocrystals were 320/300 ℃ and 280/250 ℃ respectively. ZnSe has a narrow temperature window for synthesis. Whenever we tried to synthesize ZnSe at any temperature lower than 320 ℃, defect peak in the form of a shoulder appeared along with the excitonic peak.

This is illustrated in Figure 3.1, which shows the photoluminescence (PL) spectrum of ZnSe from two of our experiments. A shoulder at 487 nm in addition to the excitonic peak (419 nm) appears, when the injection/growth temperatures were 300/250 ℃, whereas, at 320/300 ℃ the shoulder disappeared.

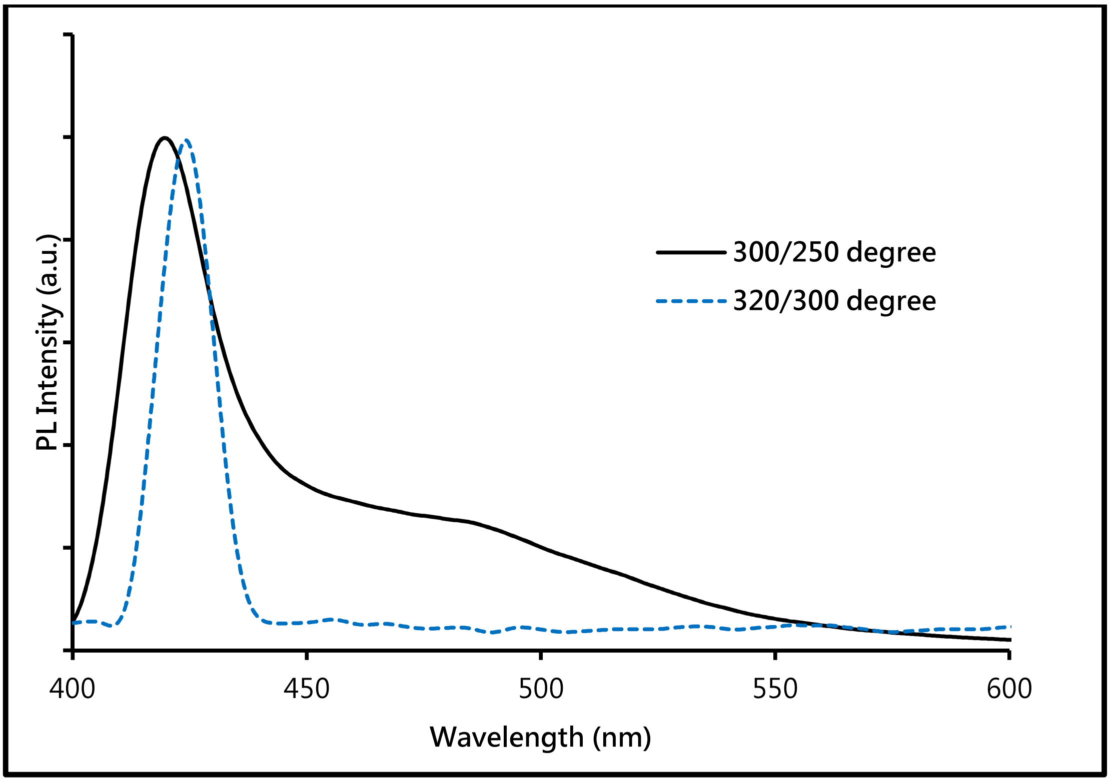

Figure 3.1. PL spectra of ZnSe nanocrystals, showing how the defect peak disappears at a higher injection/growth temperature.

An emission lifetime measurement at 419 nm and 487 nm reveals that, at 419 nm, a shorter component (τ = 6.98 ns) dominates the decay, whereas at 487 nm, a longer-lived component (63.4 ns) is predominant (Figure 3.2). The defect emission from ZnSe nanoparticles have been reported previously at 475 nm with lifetime several tens of nano seconds.[32] PL emission from ZnS defect states have also been reported to be *ca.* 100 ns.[33] Thus it is reasonable to conclude from the lifetime results, that the 419 nm peak is due to the excitonic emission and the emission at 487 nm is due to defect. By contrast, no defect peak or trap emission was observed for the CdSe nanocrystals synthesized at 280/250 °C, in the current research.

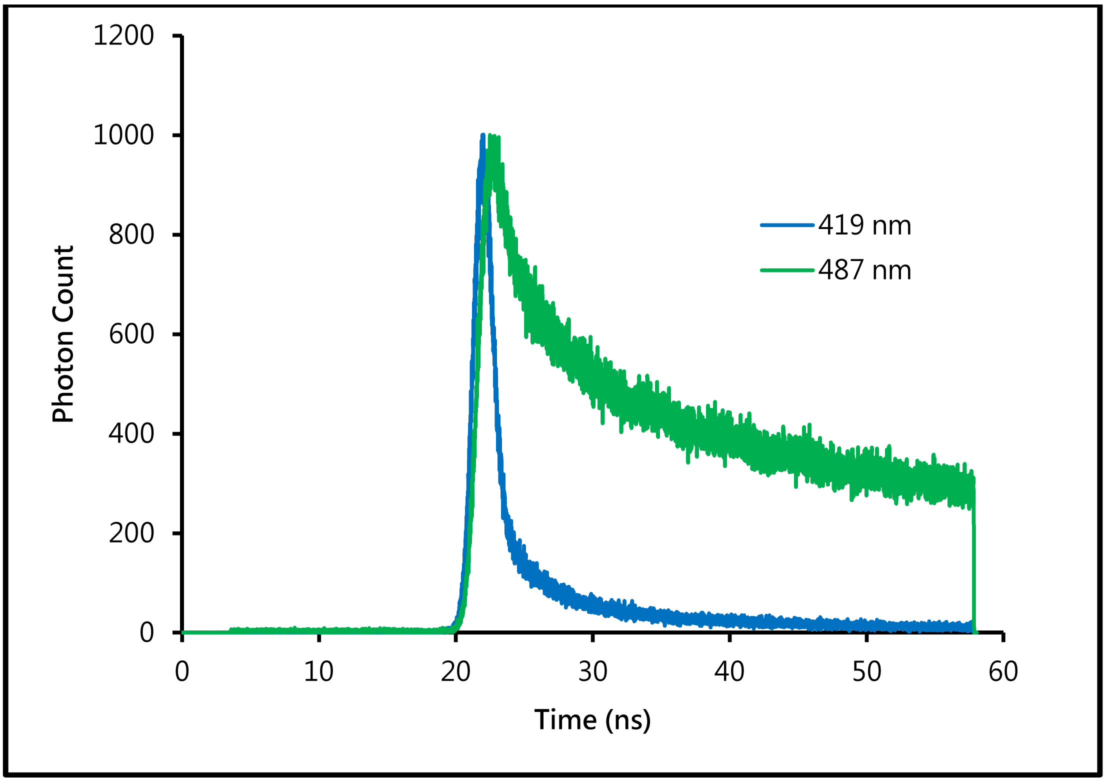

Figure 3.2. Lifetime decay curve of ZnSe QD measured at emission wavelengths 419 nm (short decay) and 487 nm (long decay). The sample was excited at λ_{ex} = 370 nm.

3.3.3 Choice of Precursors

In the current work, cadmium and zinc stearates have been used as the precursors. We noticed that zinc stearates can be used in paraffin liquid at a temperature as high as 320 °C, whereas any attempt to heat cadmium stearate in neat paraffin liquid at any temperature higher than 310 °C leads to decomposition and the reaction mixture changes to a brown color. Similar results were obtained by Qu *et al.* when they used lauric acid salt of cadmium.[21] The stearates, with long alkyl chains facilitate stabilization of the nanoparticles and initiate a more controllable nucleation process than the extremely reactive $Cd(CH_3)_2$. This controlled nature makes the syntheses more reproducible. The stearates can be readily synthesized in the lab by heating; for example, zinc stearate is prepared from the reaction of zinc acetate and stearic acid, which generates only volatile by-products that can be pumped out easily.

TBPSe was chosen as the selenium source for the syntheses of ZnSe and CdSe nanocrystals. It has been reported earlier that with TBPSe, nanocrystals of spherical shape, have always been restricted up to 5 nm diameter. Any attempt to grow particles beyond this size leads to anisotropic growth.[34] Thus, TBPSe, turned out to be a suitable selenium source for us, to grow crystals of small size. Another advantage of using TBPSe is that any excess TBPSe or any TBPO formed during the course of the reaction (Scheme 3.1), is well known to preferentially passivate the Cd rich surface, thereby, minimizing the surface defects/recombination sites.[35,36] The reaction between cadmium stearate and TBPSe leads to the formation of CdSe, TBPO and stearyl anhydride (Scheme 3.1).[19,22]

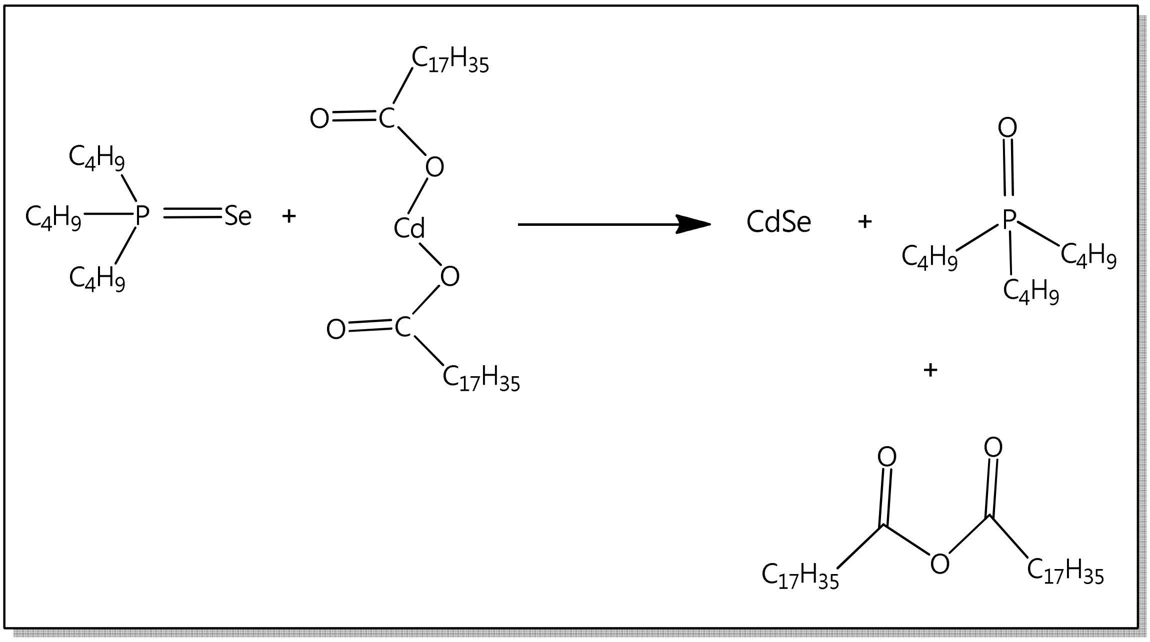

Scheme 3.1. Reaction between cadmium stearate and TBPSe.

3.3.4 Zn/Cd : Se Ratio

To determine the optimum Zn-to-Se ratio, ZnSe has been prepared at a fixed growth temperature (300 °C) but with varied Zn:Se ratio from 1:1 to 1:6. Figure 3.3 shows the variation of FWHM of the emission spectra of ZnSe QDs, that have been prepared with different Se : Zn ratio.

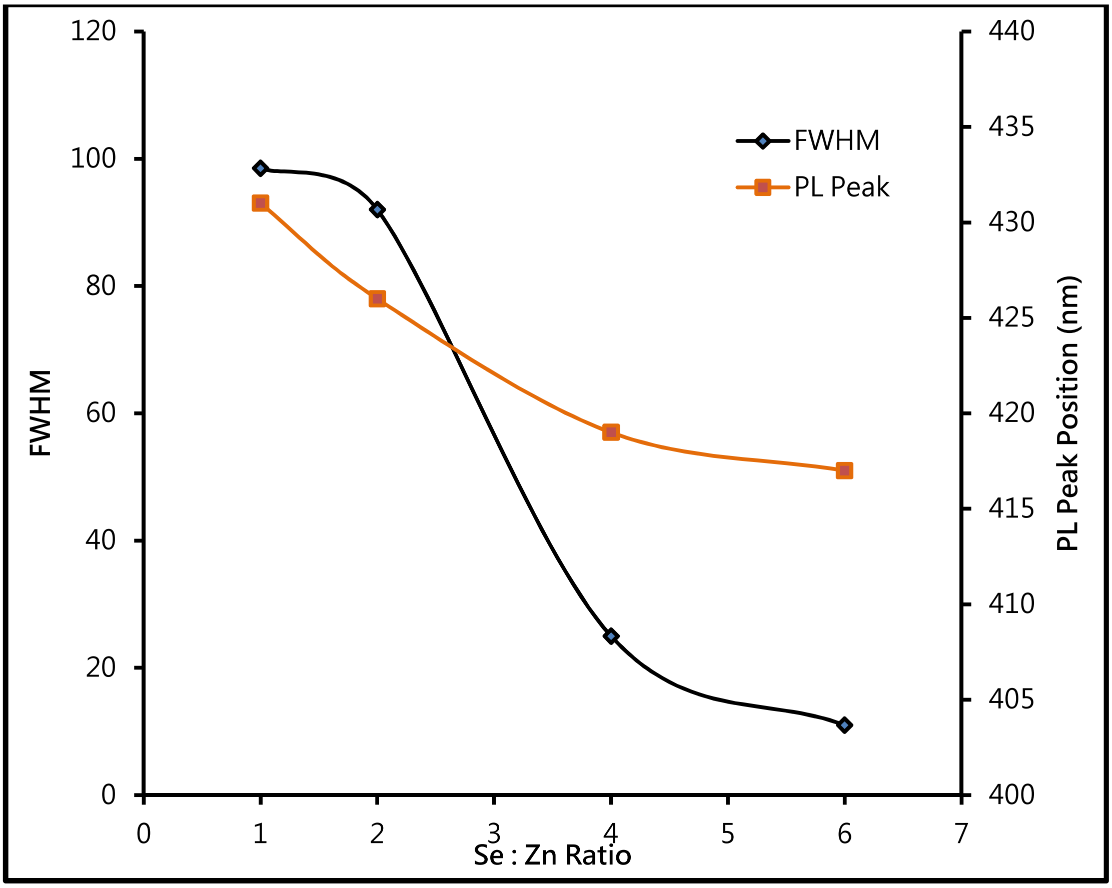

Figure 3.3. Changes in FWHM and PL peak position of ZnSe QDs with change in Se : Zn ratio.

With increasing Se:Zn ratio, the PL peak showed a blue shift, implying formation of smaller particles and the FWHM decreased, denoting a narrower size distribution. The reason for such observation is because excess Se leads to slow growth, which helps to form smaller particles with narrow size distribution due to large monomer oversaturation during growth.[37] At a high monomer concentration, the critical size remains small and focusing of size takes place, leading to smaller particles with a narrow size distribution.[14] A slow growth rate is also advantageous, because it facilitates smooth surface construction, thereby reducing surface disorders.

Therefore, the Zn/Cd:Se ratio chosen in the current research was 1:6, which showed a narrow size distribution. The presence of excess selenium helps to quantitatively consume the metal stearate and drives the reaction toward completion. Moreover, it reduces the formation of any unwanted ZnO that might be formed as any side-product. It has been reported by Li *et al.* that ZnO is formed, when carboxylates are used as precursors in the presence of a long-chain alkylamine, used as surfactants.[23]

3.3.5 Choice of Surfactant

In the current work, liquid paraffin has been used as the solvent. This is non-coordinating and cannot stabilize the nanocrystals formed. Hence, the addition of a surfactant becomes necessary. Oleylamine was used for this purpose in the current research. This 18-carbon long chain molecule has a high boiling point (364 °C) and is a suitable choice for the high temperature synthesis of both ZnSe and CdSe nanocrystals. The long chain of oleylamine also imparts solubility of the nanocrystals and provides colloidal stability to the system. Oleylamine is also believed to activate the zinc or cadmium carboxylate precursors to initiate the formation of nanocrystals, as reported by Peng' s group.[23] To avoid formation of any ZnO from the preheated mixture of amine and the stearates, the oleylamine was injected along with the TBPSe precursor solution, which made the system very stable and reproducible. Moreover, the amines are weaker bases than TOPO and have weak/intermediate coordinating capabilities.[9] Hence, in the next set of experiments with subphthalocyanine ligands (*vide* Chapter 5), the oleylamine could easily be replaced.

3.3.6 Growth Time

Figure 3.4 shows the optical spectrum of as- prepared CdSe samples as a function of time. As growth of the particles proceeds, the first excitonic peak shows a red-shift. The quantum confinement effect is clearly visible across the size range (2.68-3.72 nm) and a dramatic shift from the CdSe bulk band gap (716 nm). The spectra show 2 to 3 resolved transitions, which ensure good quality of the particles. No trap emission could be seen from the particles. The typical PL FWHMs of the samples were in the range 26-33 nm. The syntheses are very reproducible.

The green and the orange quantum dots (GQD and OQD) were preferentially synthesized by simply altering the growth time viz. 30 s and 1.5 min respectively.

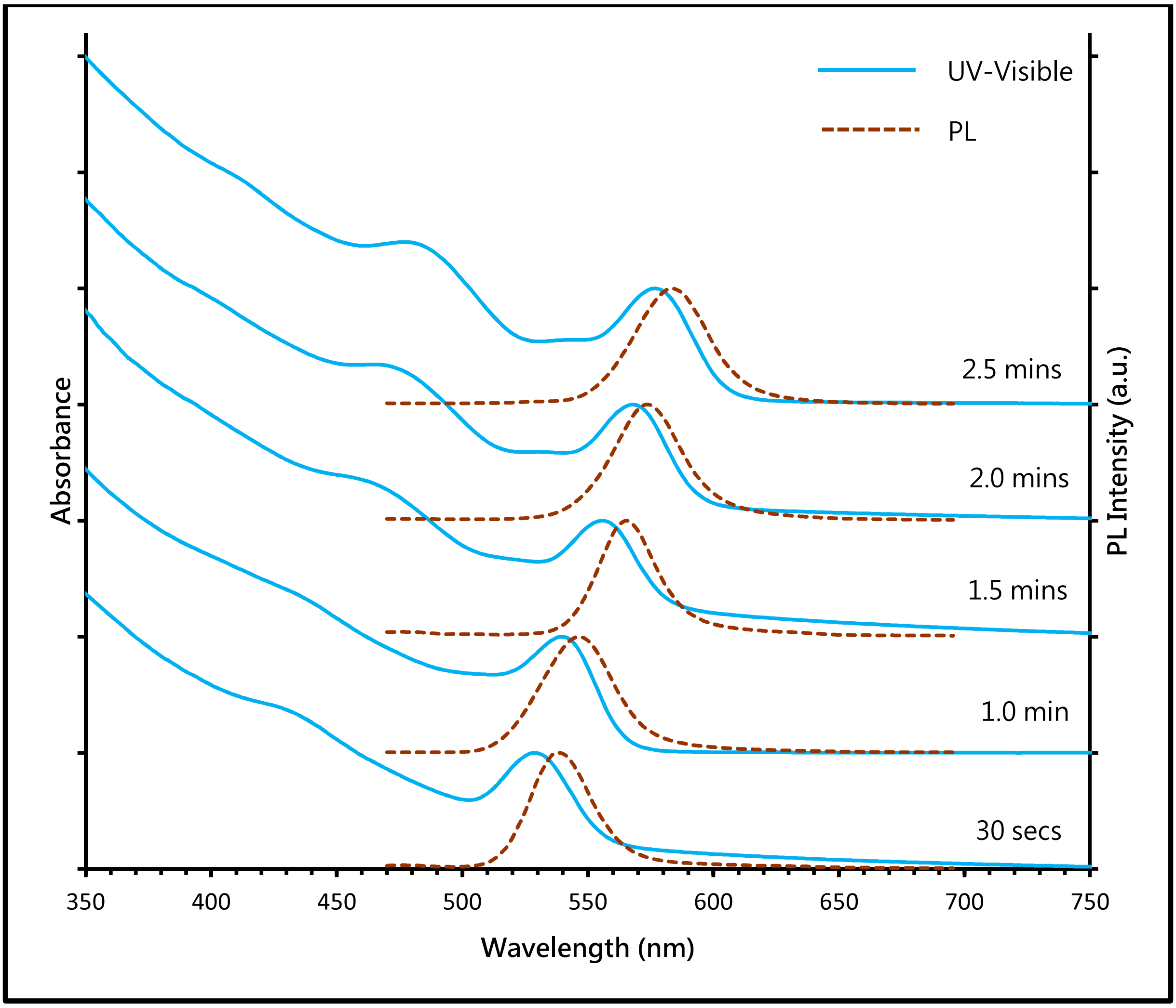

Figure 3.4. Temporal evolution of UV-visible and PL spectra of CdSe QDs.

3.4 THE OPTIMIZED RECIPE

A modified synthetic recipe was developed, which produced quantum dots of required size and quality for further experiments with subphthalocyanine, discussed in chapter 4. The detailed synthetic procedure is described in the experimental section of this chapter. Here, the different reaction conditions are tabulated for a quick reference.

Table 3.1. Reaction conditions for the syntheses of CdSe and ZnSe QDs

Parameters	**ZnSe**	**CdSe (GQD)**	**CdSe (OQD)**
Solvent	Paraffin liquid	Paraffin liquid	Paraffin liquid
Injection Temp. (℃)	320	280	280
Growth Temp. (℃)	300	250	250
Precursors	Zinc stearate TBPSe	Cadmium stearate TBPSe	Cadmium stearate TBPSe
Zn/Cd:Se	1:6	1:6	1:6
Surfactant	Oleylamine	Oleylamine	Oleylamine
Growth Time (min)	1.5	0.5	1.5

3.5 CHARACTERIZATIONS

3.5.1 Luminescence under UV Illumination

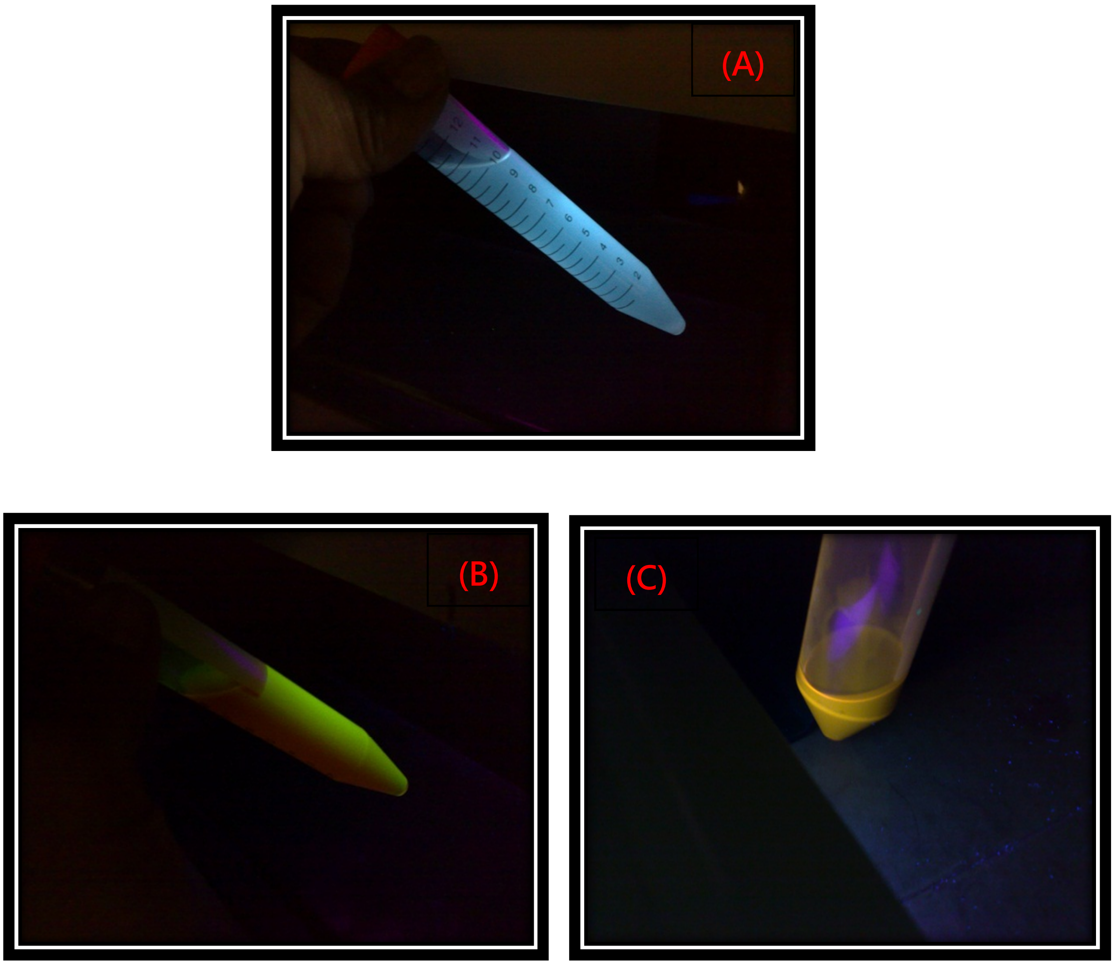

Figure 3.5. Luminescence of (A) ZnSe, (B) GQD and (C) OQD under UV illumination (365 nm).

When the quantum dots, prepared in this work, were illuminated with UV light, they showed different luminescence colors, depending on their size and nature. ZnSe showed a blue color, the smaller CdSe (GQD) green and the larger CdSe (OQD) showed orange luminescence (Figure 3.5).

3.5.2 Optical Spectra

The UV-visible and the photoluminescence spectra of ZnSe and two types of CdSe are presented in Figures 3.6 and 3.7 respectively.

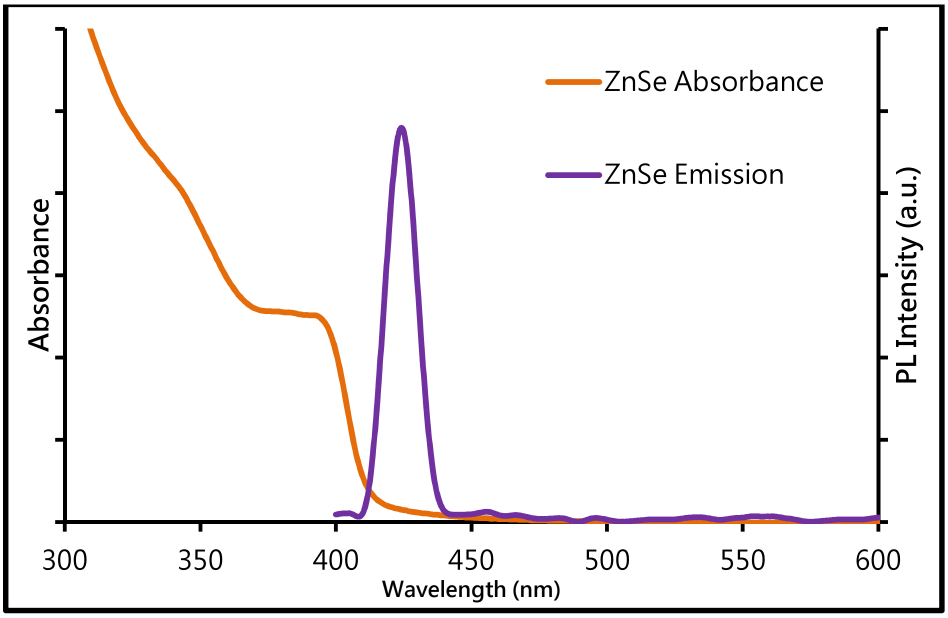

Figure 3.6. UV-visible & PL spectra of synthesized ZnSe QDs.

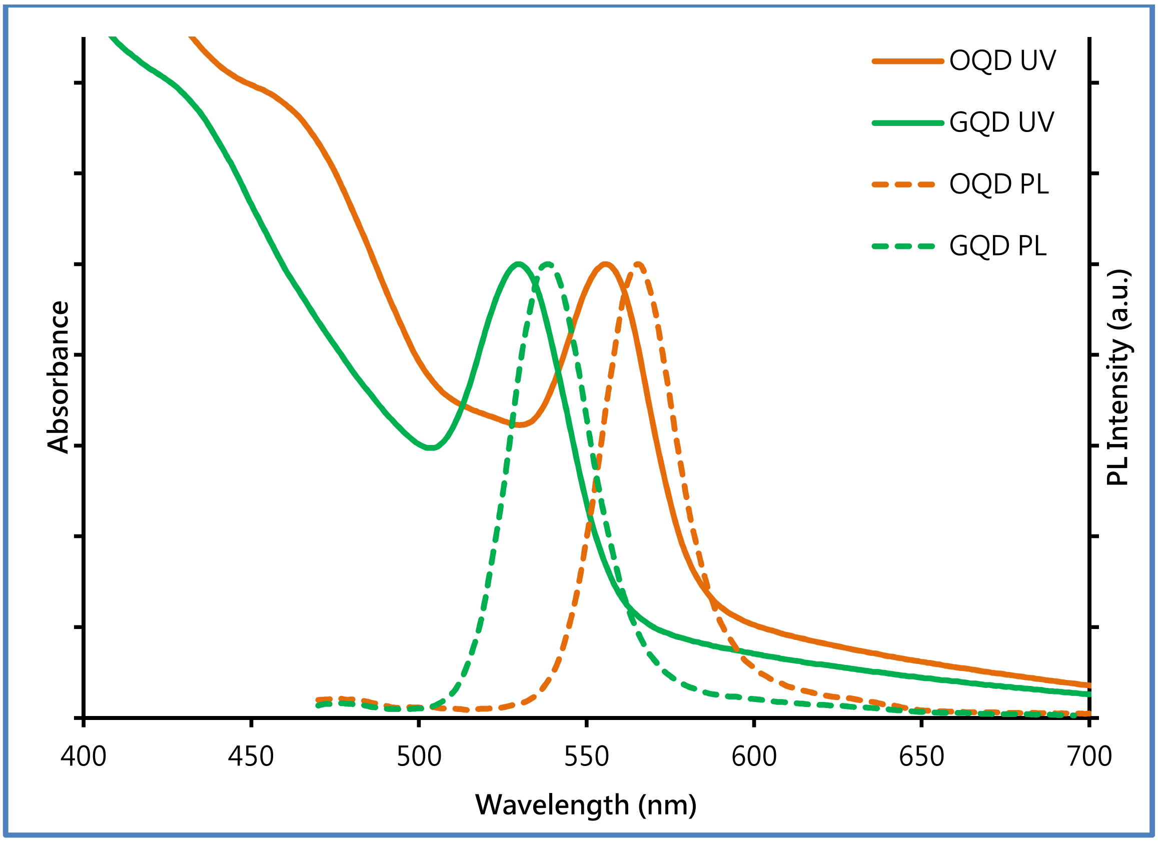

Figure 3.7. UV-visible & PL spectra of synthesized CdSe (OQD, GQD).

The first excitonic peak for ZnSe appears at 396 nm, for GQD at 530 nm and OQD at 556 nm. The FWHM for ZnSe was 13 nm, GQD was 29 nm and OQD was 26 nm. The small FWHM values signify a good monodispersity in the synthesized particles. The absence of any trap emission in the PL spectra of these nanocrystals ensures good quality and almost defect-free (or negligible defects) particles.

3.5.3 Size, Shape and Composition

The ZnSe particles are around 3 nm diameter and the two types of CdSe, GQD and OQD are *ca*. 2.68 nm and 3 nm size. Figure 3.8 shows TEM micrographs of as-prepared ZnSe and CdSe particles. The particle sizes have been calculated by measuring 200 particles and showed a standard deviation of ~0.3-0.4 nm. The particles are spherical in shape and are nearly monodisperse.

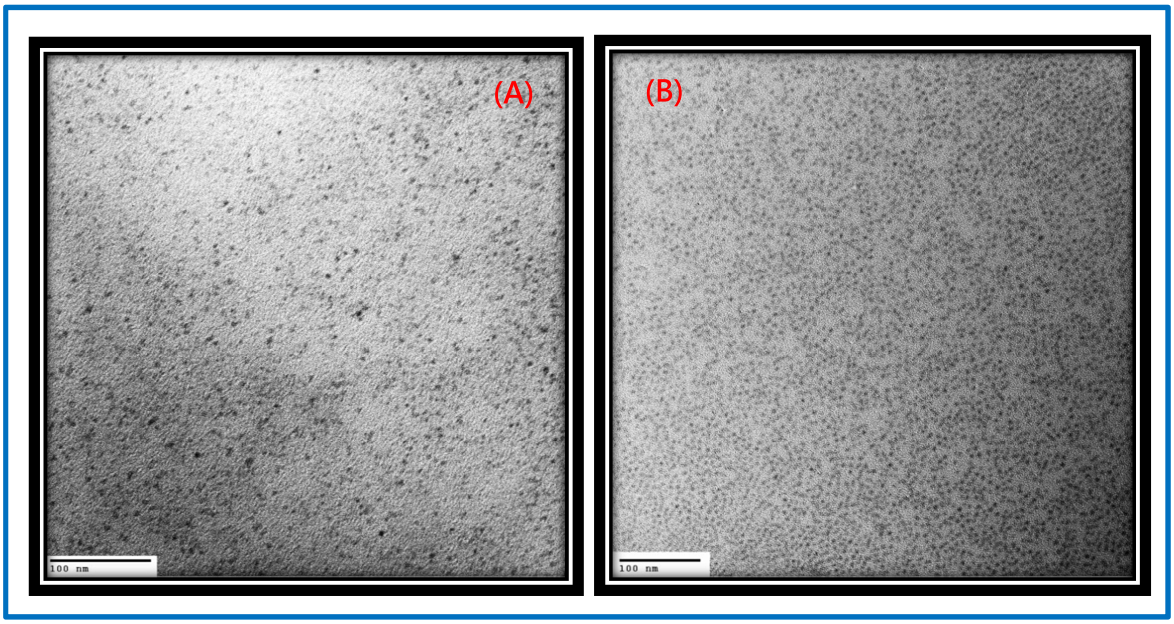

Figure 3.8. TEM micrograph of as-prepared (A) ZnSe and (B) CdSe nanoparticles.

Energy dispersive X-ray (EDX) studies of a CdSe sample show that the atomic ratio of Se : Cd is 1.02 : 1 (Figure 3.9).

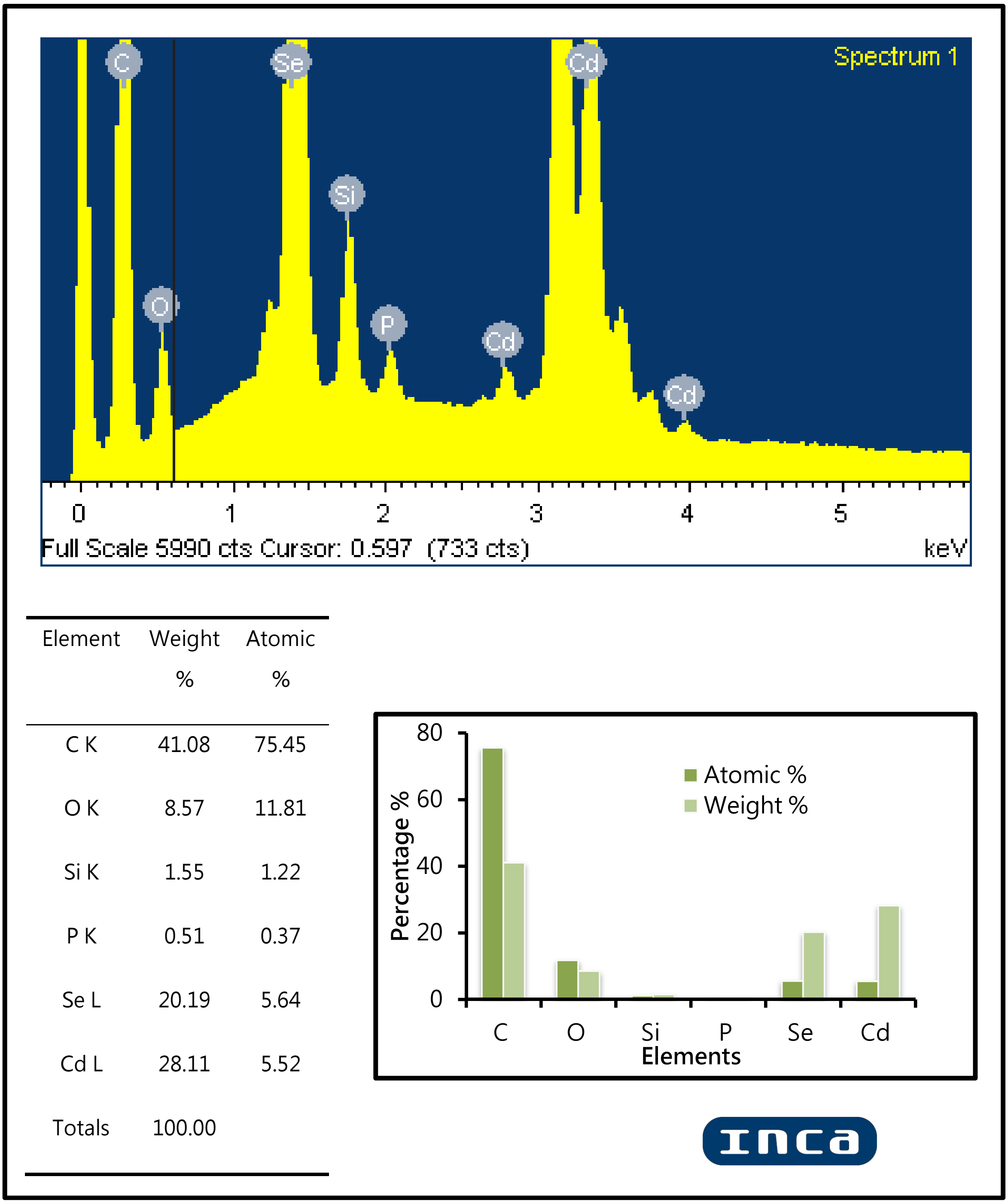

Element	Weight %	Atomic %
C K	41.08	75.45
O K	8.57	11.81
Si K	1.55	1.22
P K	0.51	0.37
Se L	20.19	5.64
Cd L	28.11	5.52
Totals	100.00	

Figure 3.9. Energy dispersive X-ray spectrum of a typical CdSe sample.

3.6 CONCLUSIONS

In summary, ZnSe and two different size CdSe nanoparticles (GQD and OQD), have been made in the current research. The particles were synthesized in liquid paraffin, with TBPSe and the corresponding stearates using a *hot injection* technique. Oleylamine was used as the surfactant. The nanocrystals showed a very narrow FWHM, which indicates a good monodispersity and the absence of any defect peak in their PL spectra, implies negligible defects in these particles. The ZnSe quantum dots have a much narrower temperature window compared to the CdSe nanoparticles. Thus, it is quite challenging to synthesize monodisperse ZnSe particles with minimal defects. The particles synthesized herein, would be used to form conjugates with the subphthalocyanine molecules, which can serve as the building block of supra-molecular nanoassemblies.

3.7 EXPERIMENTAL

3.7.1 General Procedure

Zinc acetate (Aldrich, 99.99%), Stearic acid (Acros Organics, 97%), selenium powder (Aldrich, 99.99%), tri-n-butyl phosphine (Aldrich, 97%), liquid paraffin (Fisher Scientific, pure), oleylamine (Acros Organics, 80-90%), toluene (Aldrich, 99.8%), methanol (Aldrich, 99.8%), acetone (Aldrich, 99.9%) were used as purchased.

All manipulations were performed under dry nitrogen, using standard Schlenk techniques. Toluene was pre-dried over sodium wire and distilled under nitrogen over sodium. Liquid paraffin and acetone was stored over activated 4 Å molecular sieves. The nanoparticles were synthesized using the *hot injection* technique.

3.7.2 Instrumentation

Transmission electron microscopy (TEM) images were recorded using a JEM-2000 EX Electron Microscope (Jeol Ltd) at an acceleration voltage of 200 kV. TEM samples were prepared by placing the nanocrystals dispersed in dichloromethane on 300 mesh copper grids with Holey carbon films.

UV-visible spectra were recorded on a Hitachi U-3010 spectrophotometer, using a quartz cuvette.

Steady-state photoluminescence was measured using a Perkin Elmer LS 55 fluorescence spectrometer using a quartz cuvette.

Lifetime fluorescence data were recorded using a Horiba JOBIN-YVON TCSPC Fluorolog instrument, using a quartz cuvette. For the lifetime measurement, the excitation wavelength was 370 nm and the laser pulse was 1.2 ns. The channel width was 7.085666E-03 ns/channel. The collected data were analysed using Horiba Jobin Yvon DAS6 v.6.3 software.

Energy dispersive X-ray (EDX) measurement was done on JEOL JSM 5900LV INCA Energy and Wave system, Oxford Instruments. The facility was provided by the Geotechnical Microanalysis Laboratory, School of Environmental Science, University of East Anglia, UK.

3.7.3 Synthesis of Zinc Stearate[38]

Zinc stearate was made by the fusion method by heating zinc acetate and stearic acid at 140 °C under vacuum for 4-5 h. Zinc oxide can also be used instead of zinc acetate. A 100 mL 2-neck round-bottomed flask, which was interfaced to a vacuum line, was loaded with zinc acetate (1.05 g, 5.7 mmol) and stearic acid (3.26 g, 11.5 mmol). The mixture was heated to 140 °C in vacuo for 5 h with stirring. The reaction temperature of 140 °C was chosen so that any zinc stearate formed, will remain molten (m.p. 130 °C), lowering the viscosity of the mixture. At this high temperature, the by-product, acetic acid (b.p. 118.1 °C) evaporates. After the reaction was complete, the flask was cooled to room temperature.

$$(CH_3COO)_2Zn + CH_3(CH_2)_{16}COOH \xrightarrow[4\text{-}5\ h]{140\ ^\circ C} [CH_3(CH_2)_{16}COO]_2Zn + 2\ CH_3COOH$$

The crude product was washed with diethyl ether (3 x 5 mL) to remove any stearic acid and centrifuged. Stearic acid is readily soluble in diethyl ether, $CHCl_3$, or acetone. The melting point of the final product was 129 °C. The IR spectrum showed the characteristic peaks of zinc stearate.

Yield: 97% (3.5g, 5.55 mmol); m.p. 129 °C (Lit. value[39] 130 °C); IR (neat, cm^{-1}): 1535.73 (s, υ_a COO^-), 1397.39 (ms, υ_s COO^-), 2915.27 (s, υ_a CH_2), 2847.04 (ms, υ_s CH_2), 1461.89 (ms, δ_s CH_2). The IR values are in agreement with the reported value.[38]

3.7.4 Preparation of TBPSe-Oleylamine Stock Solution

To 0.48 g of selenium powder (6 mmol) in a Schlenk tube under N_2 was added 3.5 mL of TBP. The contents were swirled to dissolve the Se powder. To this was added 2.5 mL of paraffin liquid to dilute the solution, followed by 0.7 mL of oleylamine (2 mmol). 0.67 mL of this solution was used each time to synthesize the nanoparticles.

3.7.5 Synthesis of ZnSe Nanoparticles

Zinc stearate (0.063 g, 0.1 mmol) was placed in a 25 mL 3-neck flask, fitted with a reflux condenser, an internal temperature probe and a glass stopper. The flask was then evacuated and filled with nitrogen 3-5 times to ensure complete removal of all oxygen and moisture. After replacing the glass stopper with a rubber septum, liquid paraffin (3 mL) was added to the flask and the contents were heated to 320 ℃ using a temperature-controlled heating mantle. At 320 ℃, TBPSe-amine precursor (0.67 mL, 0.6 mmol Se, 0.2 mmol amine) was swiftly injected into the flask with vigorous stirring. The temperature dropped to 300 ℃ and growth was allowed for 1.5 min. The reaction was quenched by injecting 3 mL of ice-cooled liquid paraffin and further cooling the flask in an ice-water bath.

3.7.6 Synthesis of CdSe Quantum Dots

To a 25 mL 3-neck round-bottom flask, fitted with a reflux condenser, a temperature probe and a stopper, was placed cadmium stearate (0.079 g, 0.1 mmol). The flask was then evacuated and filled with nitrogen 3-5 times to ensure complete removal of all oxygen and moisture. Liquid paraffin (3 mL) was added to the flask and the contents heated to 280 ℃ using a temperature-controlled heating mantle. At 280 ℃, TBPSe-amine precursor (0.67 mL, 0.6 mmol Se, 0.2 mmol amine) was swiftly injected in the flask with vigorous stirring. The temperature dropped to 250 ℃ and growth was allowed for 1.5 min. The reaction was quenched by injecting 3 mL of ice-cooled paraffin liquid and further cooling the flask in an ice-water bath. For smaller size particles, the growth time was reduced to 30 s.

3.7.7 Purification and Isolation of Nanoparticles

The reaction solution was cooled to 25 ℃. The mixture was centrifuged at 4000 rpm for 5 min to remove any precipitate. To the clear solution, 10 mL of isopropanol was added and the mixture was sonicated for 5-10 min. The nanocrystals precipitated from the solution and were separated by centrifugation. They were washed with an acetone-methanol-acetone sequence, and then dissolved in toluene. From toluene they were again precipitated with methanol and further washed with an acetone-methanol-acetone sequence. The final purified crystals were vacuum dried. Yield: 25 mg

\-------------------------------------

REFERENCES

(1) Greenham, N. C.; Peng, X.; Alivisatos, A. P. *Phys. Rev. B* **1996**, *54*, 17628–17637.

(2) Maheshwari, V.; Saraf, R. F. *Science* **2006**, *312*, 1501–1504.

(3) Colvin, V. L.; Schlamp, M. C.; Alivisatos, A. P. *Nature* **1994**, *370*, 354–357.

(4) Shen, Q.; Arae, D.; Toyoda, T. *J. Photochem. Photobiol. A : Chem.* **2004**, *164*, 75–80.

(5) Bruchez, M.; Moronne, M.; Gin, P.; Weiss, S.; Alivisatos, A. P. *Science* **1998**, *281*, 2013–2016.

(6) Reiss, P.; Bleuse, J.; Pron, A. *Nano Lett.* **2002**, *2*, 781–784.

(7) Lischka, K. *Phys. Stat. Sol. (b)* **1997**, *202*, 673–681.

(8) Murray, C. B.; Norris, D. J.; Bawendi, M. G. *J. Am. Chem. Soc.* **1993**, *115*, 8706–8715.

(9) Hines, M. A.; Guyot-Sionnest, P. *J. Phys. Chem. B* **1998**, *102*, 3655–3657.

(10) Talapin, D. V.; Rogach, A. L.; Kornowski, A.; Haase, M.; Weller, H. *Nano Lett.* **2001**, *1*, 207–211.

(11) Xu, S.; Kumar, S.; Nann, T. *J. Am. Chem. Soc.* **2006**, *128*, 1054–1055.

(12) Bullen, C. R.; Mulvaney, P. *Nano Lett.* **2004**, *4*, 2303–2307.

(13) Yu, W. W.; Peng, X. *Angew. Chem. Int. Ed.* **2002**, *41*, 2368–2371.

(14) Peng, X.; Wickham, J.; Alivisatos, A. P. *J. Am. Chem. Soc.* **1998**, *120*, 5343–5344.

(15) Cozzoli, P. D.; Manna, L.; Curri, M. L.; Kudera, S.; Giannini, C.; Striccoli, M.; Agostiano, A. *Chem. Mater.* **2005**, *17*, 1296–1306.

(16) Jun, Y.; Koo, J.-E.; Cheon, J. *Chem. Commun.* **2000**, 1243–1244.

(17) Van Embden, J.; Mulvaney, P. *Langmuir* **2005**, *21*, 10226–10233.

(18) Wang, Q.; Pan, D.; Jiang, S.; Ji, X.; An, L.; Jiang, B. *Chem. Eur. J.* **2005**, *11*, 3843–3848.

(19) Yordanov, G. G.; Dushkin, C. D.; Adachi, E. *Colloids and Surfaces A: Physicochem. Eng. Aspects* **2008**, *316*, 37–45.

(20) Peng, Z. A.; Peng, X. *J. Am. Chem. Soc.* **2000**, *123*, 183–184.

(21) Qu, L.; Peng, Z. A.; Peng, X. *Nano Lett.* **2001**, *1*, 333–337.

(22) Liu, H.; Owen, J. S.; Alivisatos, A. P. *J. Am. Chem. Soc.* **2006**, *129*, 305–312.

(23) Li, L. S.; Pradhan, N.; Wang, Y.; Peng, X. *Nano Lett.* **2004**, *4*, 2261–2264.

(24) Zhu, J.; Koltypin, Y.; Gedanken, A. *Chem. Mater.* **1999**, *12*, 73–78.

(25) Iwahori, K.; Yoshizawa, K.; Muraoka, M.; Yamashita, I. *Inorg. Chem.* **2005**, *44*, 6393–6400.

(26) Zhong, X.; Feng, Y.; Zhang, Y. *J. Phys. Chem. C* **2006**, *111*, 526–531.

(27) Shen, H.; Wang, H.; Li, X.; Niu, J. Z.; Wang, H.; Chen, X.; Li, L. S. *Dalton Trans.* **2009**, 10534–10540.

(28) Bullen, C.; Van Embden, J.; Jasieniak, J.; Cosgriff, J. E.; Mulder, R. J.; Rizzardo, E.; Gu, M.; Raston, C. L. *Chem. Mater.* **2010**, *22*, 4135–4143.

(29) Sapra, S.; Rogach, A. L.; Feldmann, J. *J. Mater. Chem.* **2006**, *16*, 3391–3395.

(30) Qu, L.; Peng, X. *J. Am. Chem. Soc.* **2002**, *124*, 2049–2055.

(31) Dai, Q.; Xiao, N.; Ning, J.; Li, C.; Li, D.; Zou, B.; Yu, W. W.; Kan, S.; Chen, H.; Liu, B.; Zou, G. *J. Phys. Chem. C* **2008**, *112*, 7567–7571.

(32) Murase, N.; Gao, M. *Mater. Lett.* **2004**, *58*, 3898–3902.

(33) Bol, A. A.; Meijerink, A. *Phys. Rev. B* **1998**, *58*, R15997–R16000.

(34) Acharya, S.; Sarma, D. D.; Jana, N. R.; Pradhan, N. *J. Phys. Chem. Lett.* **2010**, *1*, 485–488.

(35) Rafeletos, G.; Nørager, S.; O′ Brien, P. *J. Mater. Chem.* **2001**, *11*, 2542–2544.

(36) Jasieniak, J.; Mulvaney, P. *J. Am. Chem. Soc.* **2007**, *129*, 2841–2848.

(37) De Mello Donegá, C.; Hickey, S. G.; Wuister, S. F.; Vanmaekelbergh, D.; Meijerink, A. *J. Phys. Chem. B* **2003**, *107*, 489–496.

(38) Gönen, M.; Balköse, D.; İnal, F.; Ülkü, S. *Ind. Eng. Chem. Res.* **2005**, *44*, 1627–1633.

(39) Lide, D. R. *CRC Handbook of Chemistry and Physics*; 90th. ed.; CRC Press, Boca Raton, Florida, 2010.

CHAPTER 4 QUANTUM DOTS MEET SUBPHTHALOCYANINES: A SYSTEMATIC STUDY OF THE FORMATION OF AND ENERGY FLOW IN II-VI HYBRID NANOASSEMBLIES

4.1 INTRODUCTION

In the last few years, research in nanoscience advanced significantly beyond synthesis and characterization of the so-called quantum dots (QDs) and concentrated more on their applications. To accomplish this, inorganic semiconductor nanoparticles have often been found to couple with organic molecules,[1,2] polymers,[3] dyes,[4,5] and biomolecules[6], to form novel hybrid nanoassemblies. In many of these hybrid assemblies, especially those which find applications in photodynamic therapy and imaging, the QDs behave as light energy accumulators (donors) and transfer that energy to the hybrid counterpart (acceptors).

CdSe based nanoassemblies are perhaps the most studied systems in this regard because they offer several advantages, such as high extinction coefficients, size-tunable band gaps, continuous absorption spectra and synthesis of the particles with remarkable size control. The physics of energy transfer between the donor and the acceptor involves either a charge-transfer mechanism[7–9] or a radiation-less process through dipole-dipole interactions known as fluorescence (or Förster) resonance energy transfer (FRET)[10,11] and a thorough understanding of this energy transfer process is the key to build an efficient donor-acceptor hybrid system.

Although a wide range of compounds have been coupled with different QDs, interestingly, to the best of our knowledge there are no prior examples where subphthalocyanine (SubPc) molecules have been utilized to form any sort of nano-hybrids. In spite of their rich photophysical properties, viz. intense pink color, wide range of absorption spectra, and obvious fluorescence, it is surprising that the interaction of subphthalocyanines with nanoparticles has not been explored. To exploit the above-mentioned properties of SubPcs, in conjunction with the light harvesting nature of the QDs, we have attempted to interface the two moieties, for the first time, and to construct a new class of nanoassemblies. The formation of a SubPc-QD complex, association constant, energy transfer mechanism, the number of SubPc attached per QD and FRET parameters have been addressed in detail in the current work. This work is expected to lead to the hierarchical syntheses of novel supra-nano constructs in the future.

4.2 SURFACE FUNCTIONALIZATION OF QUANTUM DOTS: ITS MEANING AND IMPORTANCE

Due to a large surface-to-volume ratio, many of the chemical and physical properties of nanoparticles are principally guided by their surface structure and surface atoms. In contrast to the core atoms, the surface atoms in a nanocrystal are always coordinatively unsaturated and give rise to dangling bonds. In a typical synthesis of nanoparticles, ligands (surfactants) are initially introduced into the system to attach to these coordinatively unsaturated surface atoms of the nanoparticles that prevent coagulation of the particles and impart stability. Depending on the intended property and application of the particles, these original ligands are then replaced by a wide variety of molecules, with some donor groups, to give rise to novel physical and chemical properties of the particles for end applications. This derivatization of the surface of the quantum dots, to obtain desired functionality, by a judicial choice of ligand is known as *Surface Functionalization*. A large variety of molecules has been attached to quantum dots to-date, through various donor groups, such as thiols,[12,13] carbodithioic acid,[14] amines,[1,15] phosphines[16,17] or phosphine oxides.[18,19] Generally a bifunctional ligand X-Y-Z is chosen for this purpose, in which, X is a functional group having high affinity to bind to the quantum dot surface, Y is a spacer of alkyl, aryl or macrocycles, and Z is the second functional group, which binds to other molecules or a substrate or to another nanoparticle. It is the nature of Z that introduces the desired functionality and property to the host quantum dot.

Surface functionalization of nanoparticles becomes particularly significant when one desires to employ the particles to generate functional nanomaterials. Knowledge of the type of ligand being attached to the particle surface and the type of bond that the ligand forms with the surface atoms is of crucial importance to modify or tune the stability, processability and reactivity of the nanoparticles. The spectroscopic behavior of the quantum dots are also greatly influenced by the nature of surface functionalization of the dots. The three principal functions of the surface ligands are –

i) They prevent individual colloidal nanoparticles from aggregation.

ii) They facilitate nanocrystals' dispersion in a large variety of solvents.

iii) Ligands with appropriate functional groups serve as bridging units and encourage coupling of the quantum dots to other molecules, substrates or to another nanoparticle, opening up possibilities to fabricate novel hybrid nanomaterials.

The surface functionalization process leads to a well-defined surface chemistry of the nanoparticles and essentially the original size of the particles is maintained.

4.3 A BRIEF SURVEY OF THE CURRENT STATE-OF-THE-ART SUPRA-NANOASSEMBLIES

A wide range of research had been reported to-date on functionalization of quantum dot surfaces to achieve various functional nano-hybrids. Functionalization with different classes of compounds is discussed below.

4.3.1 Organic Compounds

Miliron *et al.*, first reported a general approach of attaching an organic functionality to the class of compound semiconductors typified by CdSe, by using the phosphonic acid group.[2] A coating of electroactive oligothiophene was attached to CdSe nanoparticles, to facilitate the particles' interaction with a matrix of organic semiconductor. The oligothiophene moiety was terminated with a phosphonic acid group, which binds strongly to the CdSe surface.

4.3.2 Lipids

TOPO capped CdSe nanocrystals were co-solubilized with phosphate functionalized lipid, to obtain a self-assembled monolayer of phospholipid around CdSe. It was possible to tune the physical and chemical properties of the nanocrystals by simply altering the polar heads of the lipids. The authors demonstrated that such multi-functionalized lipid-coated NCs can bind different proteins (streptavidin or oligohistidine) per particle specifically and subsequently position themselves on micro-patterned surfaces to form nanometer-sized supra-molecular structures of higher complexity. Although, lipids have been used as coating on nanoparticles earlier, this is the first report, where lipids can be multi-functionalized to form complex supra-molecular structures.[20]

4.3.3 Polymers

An interesting example of polymer coated nanocrystals have been provided by Sill and Emrick,[21] where instead of attaching the nanoparticles to a polymer, polymerization was done directly on the surface of the quantum dots. TOPO capped CdSe nanocrystals were first functionalized with nitroxide containing ligand via room temperature ligand exchange in THF. Then polystyrene or poly(methyl methacrylate) were grown directly on the surface of these nitroxide-functionalized nanoparticles via nitroxide-mediated controlled free radical polymerization to form polymer-nanocrystal composite. Conventional methods to grow the above-mentioned polymers (anodic and free-radical polymerization) are not compatible with the nanoparticles, since they are too severe in nature and degrade the particles and quench their photoluminescence.

4.3.4 Biomolecules: Protein, Enzyme and DNA

Biomolecules such as proteins, enzymes, DNA have also contributed to the literature of QD surface functionalization. Bawendi’s group showed a direct method of conjugating *E. coli* maltose binding protein to luminescent CdSe-ZnS core/shell quantum dots for use as bioactive fluorescent probes in sensing, imaging, immunoassay, and other diagnostics applications. The approach is based on self-assembly utilizing electrostatic attractions between water-soluble, negatively charged lipoic acid capped CdSe-ZnS quantum dots and a bi-functional protein, having positively charged leucine attachment domains. This method is reported to be quite general and is applicable to a wide range of core-shell nanoparticles and biomolecules amenable to alterations of the interaction domain, such as charge, size, pH, and temperature.[22] Narayanan *et al.* reported a direct covalent attachment of the enzyme α-chymotrypsin onto the surface of CdS quantum dots.[23] The covalent nature of the bond was confirmed by MALDI-MS, in which the CdS-enzyme conjugate peak appeared as the major one. No structural perturbation was seen in the secondary structure of the enzyme; however, due to immobilization on the quantum dot surface, the enzyme’ s activity reduced to half of that of the free form. The authors claimed that the enzyme-conjugated nanoparticles were well dispersed and remained indefinitely stable in aqueous solutions. Pathak *et al.* used water soluble hydroxyl terminated CdSe quantum dots to couple with different oligonucleotide (DNA) via a carbamate linkage for the detection of chromosome abnormalities or mutation using fluorescence *in situ* hybridization (FISH) procedures. The DNA-dot conjugates are stable for months and are useful luminescent probes in FISH assays.[13]

4.3.5 With Another Quantum Dot

Surface functionalized nanoparticles can also be attached to another particle to form dimer-like conjugates. For example, di-n-octyl phosphine oxide functionalized silicon nanoparticles can efficiently be coupled with CdSe quantum dots, through the bonding of phosphine oxide corona of silicon particles with the CdSe dot surface. A pronounced photoluminescence quenching of the CdSe quantum dots was observed, and the energy transfer was thought to proceed via hole transfer from CdSe to Si.[18] Another strategy to knit two nanoparticles together is through 1,3-dipolar cycloaddition of an azide and an acetylenic group, known as *click chemistry* (Scheme 4.1).[3,24]

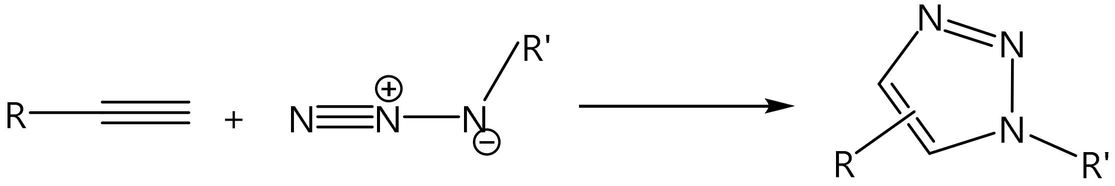

Scheme 4.1. The Click Chemistry.

In both cases, two species of CdSe quantum dots were used, one functionalized only with the azide group and the other with the acetylenic group. The two species were then joined by using click chemistry.

4.3.6 Macrocycles: Phthalocyanines and Porphyrins

Although subphthalocyanines have never been used previously to couple with quantum dots, there are ample examples where phthalocyanine (Pc) molecules have been used to form QD-Pc conjugates.[5,11,25] Hone *et al.* stabilized gold nanoparticles with Pc, which are potential carriers for delivery of photosensitizers in photodynamic therapy.[26] Use of semiconductor quantum dots (CdSe) with silicon based Pc was reported by Burda and co-workers in 2003.[27] This was the first report on QD-based FRET to facilitate excitation of a photosensitizer (Pc) in photodynamic therapy. Another class of QD-macro cycle conjugate, which gained a lot of attention, is the QD-porphyrin system. von Borczyskowski' s research group has done an appreciable amount of work on such systems, and showed that when meta- and para- pyridyl substituted porphyrins were conjugated with CdSe/ZnS core/shell quantum dots, photoluminescence of the particles was quenched. For ortho- pyridyl substituent, no quenching was observed. They concluded that porphyrins attach themselves to the QD surface through the meta- and para- pyridyl groups and remain perpendicular to the QD surface.[28] In another publication, they reported that the porphyrin-to-nanoparticle ratio is 1:1, even at higher porphyrin concentration than CdSe nanoparticles.[29] In 2010, Frasco *et al.* reported a novel hybrid CdSe-porphyrin (para- pyridyl substituted) conjugate, which can be used for direct sensing of metal ions (Zn^{2+}). The zinc ions attach to the CdSe-porphyrin conjugate at the free pyridyl end of the porphyrin, which is detected by an increased fluorescence of the CdSe QD. The attached zinc ions provide a passivation to the CdSe QDs and an increased band-gap emission is seen.[30]

4.4 WHY SUBPHTHALOCYANINE?

Subphthalocyanines are 14-π electron aromatic systems, which have a non-planar cone shaped structure. These compounds are only known as boron derivatives. The boron atom is tetra coordinated, three of which are attached to the three pyrrole nitrogens of the rigid macrocycle, and the fourth bond lies perpendicular to the macrocycle. Unlike the phthalocyanine, the macrocycle is not flat and planar. The boron lies in the center and slightly above the macrocycle, giving the entire molecule a pyramidal structure. The axial perpendicular bond on boron serves as a placeholder for different functional groups and allows one to tune the properties of the subphthalocyanine molecule.

In the current work, a tri-substituted subphthalocyanine (SubPc) was used, which has three peripheral alkyne groups, each terminated with a meta- pyridyl ring. An unsubstituted version (UsubPc) was also used for control experiments, which lacks the substituted alkyne-pyridyl moiety and simply has the SubPc core. The boron atom has an axial –OPh group in both the substituted and the unsubstituted versions.

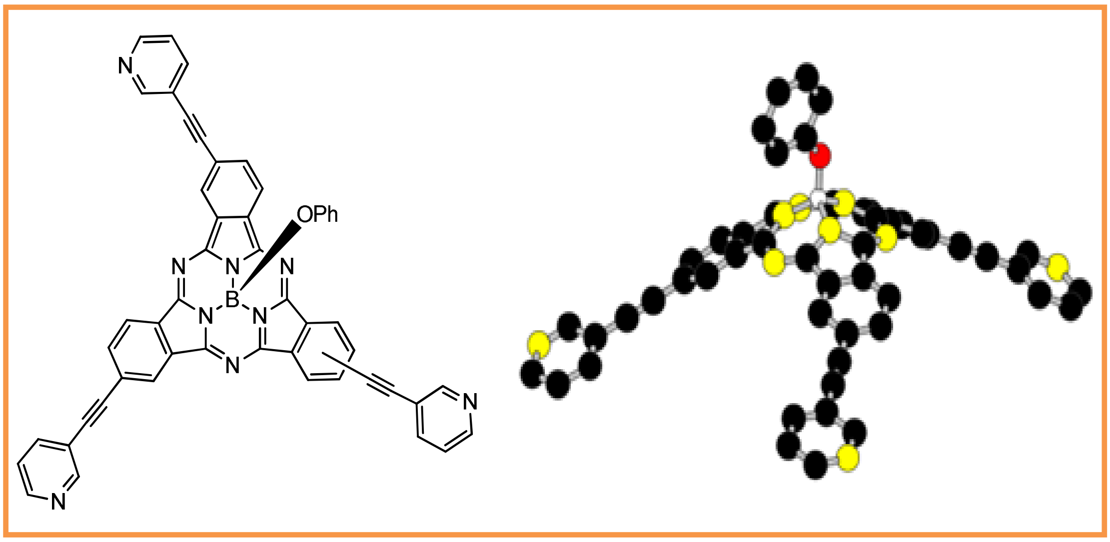

Figure 4.1. Structure of tri-substituted subphthalocyanine.

The primary reasons to select SubPc molecules for our experiments are as follows -

i) The 3-dimensinal conical shape of the core gives the molecule a convenient cup shape for an easy fit onto the spherical surface of the nanoparticles.

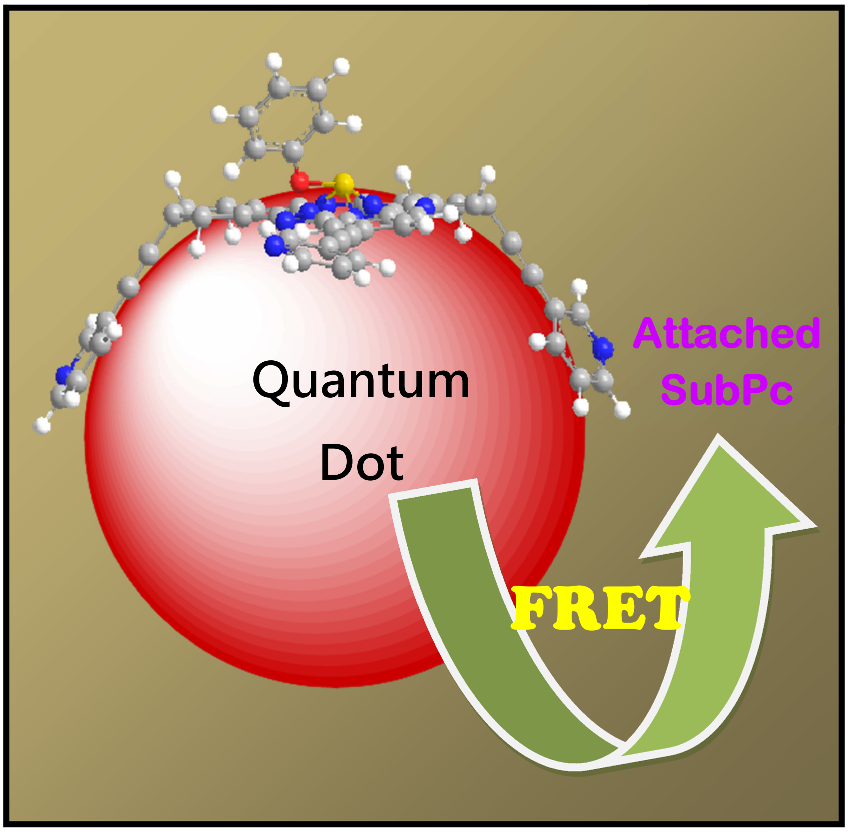

Figure 4.2. Schematic diagram showing attachment of SubPc molecule on CdSe quantum dot and energy transfer through FRET mechanism.

ii) The meta-pyridyl groups attached to the alkyne side chains serve as the binding sites. The flexibility and the 3-dimensional orientations of all the three meta pyridyl rings are suitable for anchoring on a spherical surface, behaving as a tridentate chelating ligand. On the other hand, para-pyridyls would have been more difficult to bind. Tetra-substituted porphyrins, though having four pyridyl groups, could only use two to bind due to the flat structure of the porphyrin core, as reported previously.[28]

iii) The axial –OPh group on boron imparts a directional functionality perpendicular to the macrocycle cone, and can be suitably substituted to covalently attach two or more nanoparticles to form supra nanoassemblies. Additionally, the –OPh group also prevents any pi-stacking of the SubPc molecule, thereby, keeping the optical spectrum and structure interpretation simple.

iv) SubPcs are bright pink in color and have a wide absorption spectrum; the Soret band absorbs at 365 nm and the Q band at 587 nm (Fig. 4.3). The absorption of SubPc is almost nil at and around 450 nm, although the QDs show appreciable absorbance at this wavelength. This allowed us to preferentially excite the QD at 450 nm but not the SubPc.

v) Their single strong emission peak at 597 nm (Fig. 4.3) could be easily identified and can be monitored systematically to study the energy transfer mechanism.

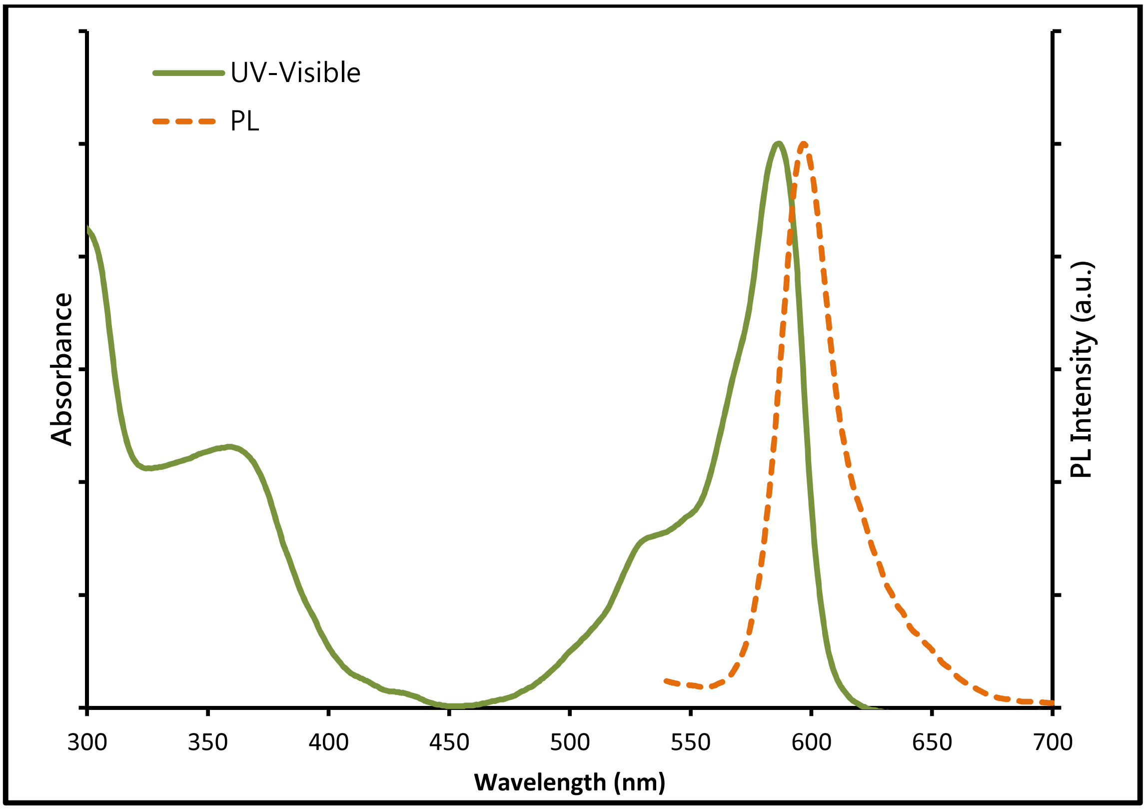

Figure 4.3. UV-visible & Photoluminescence (PL) spectra of SubPc.

vi) Since no previous attempt had been made to build a SubPc-QD nanoassembly, the potential of the SubPc to form nanoassembly can be verified and the energy transfer mechanism can also be simultaneously evaluated.

4.5 DETERMINATION OF EXTINCTION COEFFICIENTS OF QDS

A brief discussion on one of the fundamental aspects of nanoparticles should find a place in the current chapter – how to determine the concentration of a solution of nanoparticle? Generally, by gravimetric methods, one can determine the weight, from which the moles of any bulk level chemical compound can be calculated. In the case of nanoparticles, simple gravimetry fails due to an unknown number of stabilizing ligands on the surface of the particles. Even the UV-visible technique fails to estimate the exact concentration either of pure nanoparticles or with some ligands because the extinction coefficient value changes with the size and purity of the particles, which in turn depend on the experimental procedure and the non-transferable/non-imitable capability of the experimentalist. A few reports have addressed this gap and attempted to determine the concentration and extinction coefficient of nanoparticles (mostly dealing with CdSe), through different approaches such as membrane osmometry, atomic absorption spectroscopy, anodic stripping voltammetry along with fitting the data in empirical polynomial functions and computer softwares.[9,31–33] The extinction coefficient, even though it followed some cubic function, becomes random above particle diameter 4.5 nm. To determine the extinction coefficient of CdSe, we used the equation provided by Yu *et al.*[33]

$\varepsilon = 5857\,(D)^{2.65}$, where D is the diameter of the nanoparticle.

$D = (1.6122 \times 10^{-9})\,\lambda^4 - (2.6575 \times 10^{-6})\,\lambda^3 + (1.6242 \times 10^{-3})\,\lambda^2 - (0.4277)\,\lambda + 41.57$, where λ is the wavelength of the first excitonic peak.

Once the ε value is known, the concentration of the particles can be calculated using the Lambert-Beer Law. We have seen that concentration calculated using gravimetric method (ignoring the surface ligands on the particles), gives a slightly lesser value than the above method (11% less). Where concentration does not need to be known very precisely, the gravimetric method is quite handy and fast. To calculate gravimetrically the following approximations are made -

(i) The nanoparticles are hard spheres.

(ii) The particles are mono disperse with a fairly constant diameter.

(iii) The densities of the bulk CdSe and of the nanoparticles are essentially identical, due to similar crystal packing.

Now, Volume of a particle, $V = (\pi/6)\,D^3$, where D is the diameter of the particle

Mass of a particle = $V\rho$, where ρ=density of CdSe, 5.82 g cm^{-3}

Weight of 1 mole of CdSe NPs = $N_AV\rho$, where N_A = Avogadro number

Moles of particles weighed = $w / N_AV\rho$, where w is the particles' weight in grams.

The ZnSe particles are weighed gravimetrically, since there are no available ε data in the literature.

4.6 RESULTS AND DISCUSSIONS

4.6.1 Absorption/Emission Features of SubPc and QDs

ZnSe and two different sizes of CdSe QDs, viz. the smaller size or Green QDs (GQDs) and the larger size or Orange QDs (OQDs), as described in chapter 3, have been used to couple with the tri-substituted SubPc.

While comparing the absorption/emission features of the quantum dots with that of the SubPc, it was found that, unfortunately ZnSe does not absorb at 450 nm, the point of minimum absorption of the SubPc, and thus no preferential excitation of ZnSe over SubPc would be possible. In addition, the ZnSe QDs also do not emit at a wavelength, where the SubPc molecule shows an appreciable absorbance. Thus, in other words, it can be said that the overlap integral between ZnSe emission and SubPc absorption is negligible (Fig. 4.4). Hence, no photophysical studies could be done with the ZnSe-SubPc pair; instead an NMR study was performed.

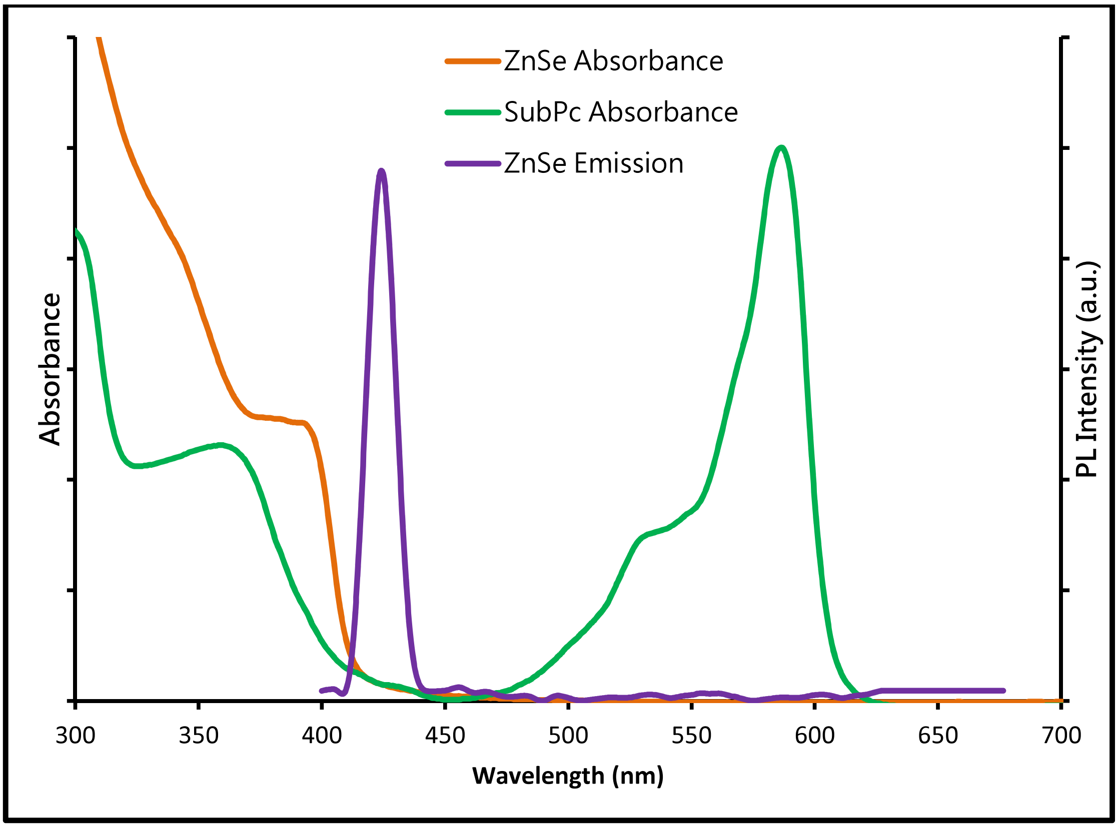

Figure 4.4. Comparison of UV-visible & PL spectra of ZnSe & SubPc.

By contrast, CdSe QDs show a high absorbance at 450 nm and the SubPc molecule also absorbs appreciably at wavelengths, where CdSe QDs emit (Fig. 4.5). Thus the overlap integral between the pair is significant and they make a promising donor-acceptor couple in photo-physical studies.

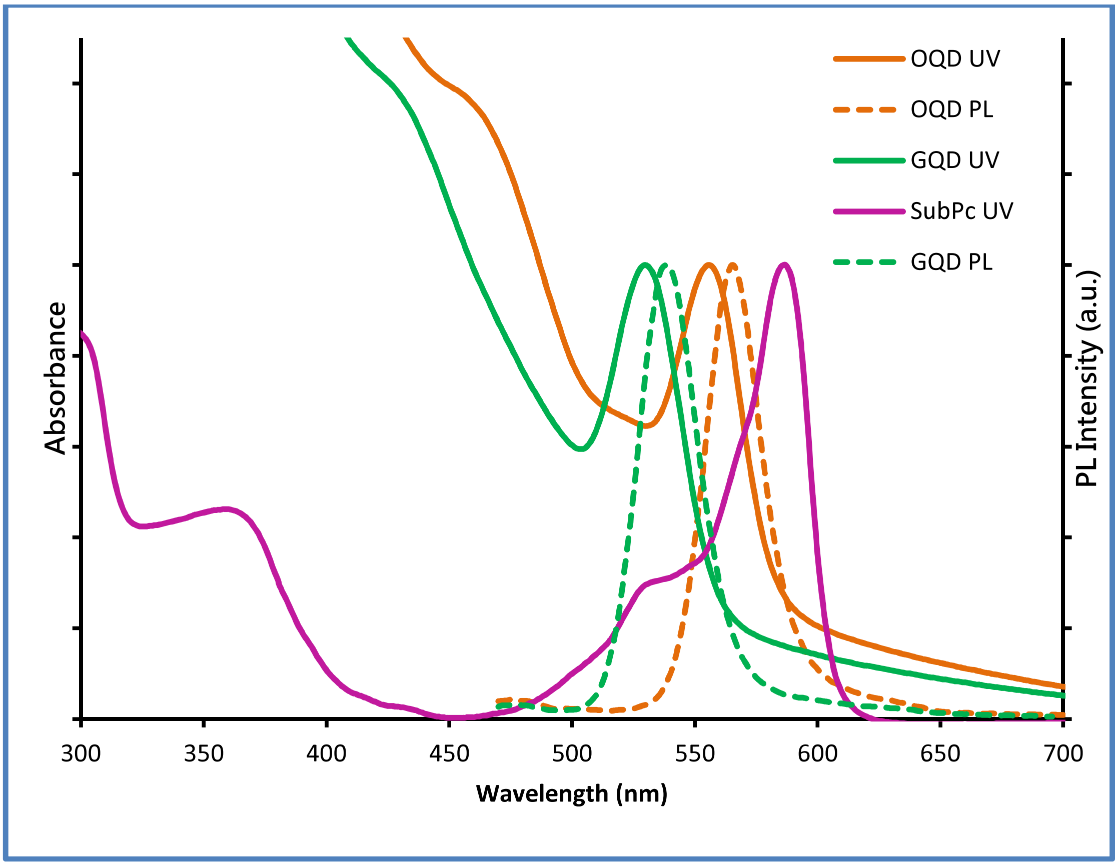

Figure 4.5. Comparison of UV-visible & PL spectra of CdSe (OQD, GQD) & SubPc.

4.6.2 Fluorescence Quenching of CdSe Quantum Dots

To study the mechanism of energy transfer between CdSe QDs and SubPc, both GQD and OQD were titrated with SubPc.

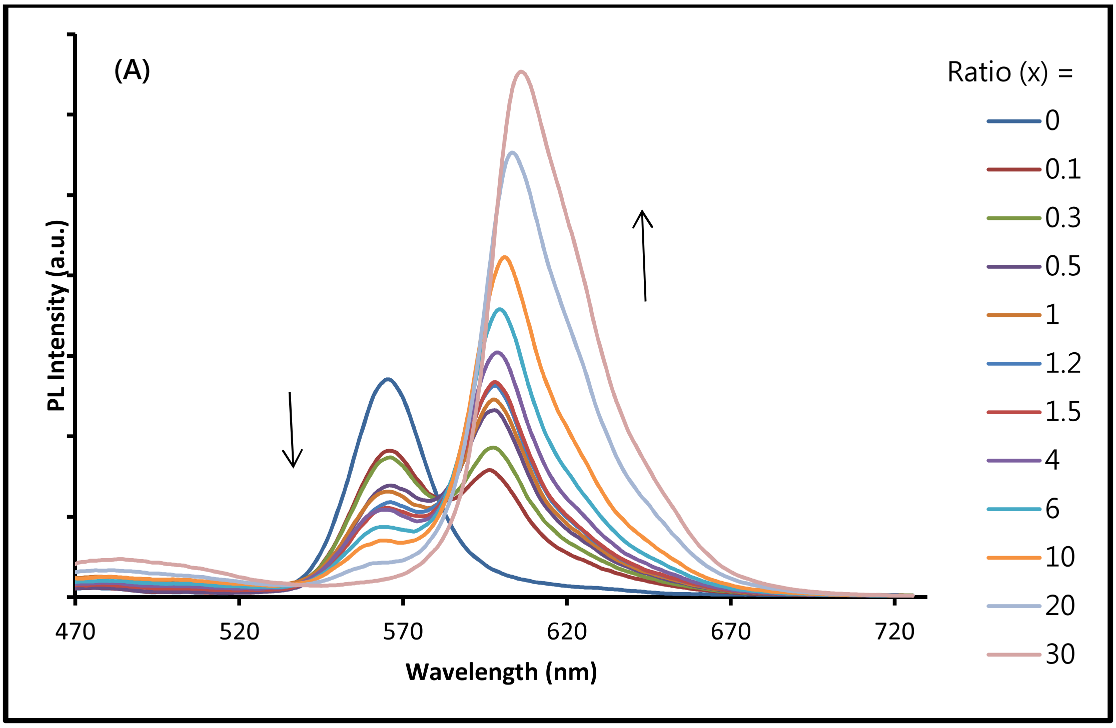

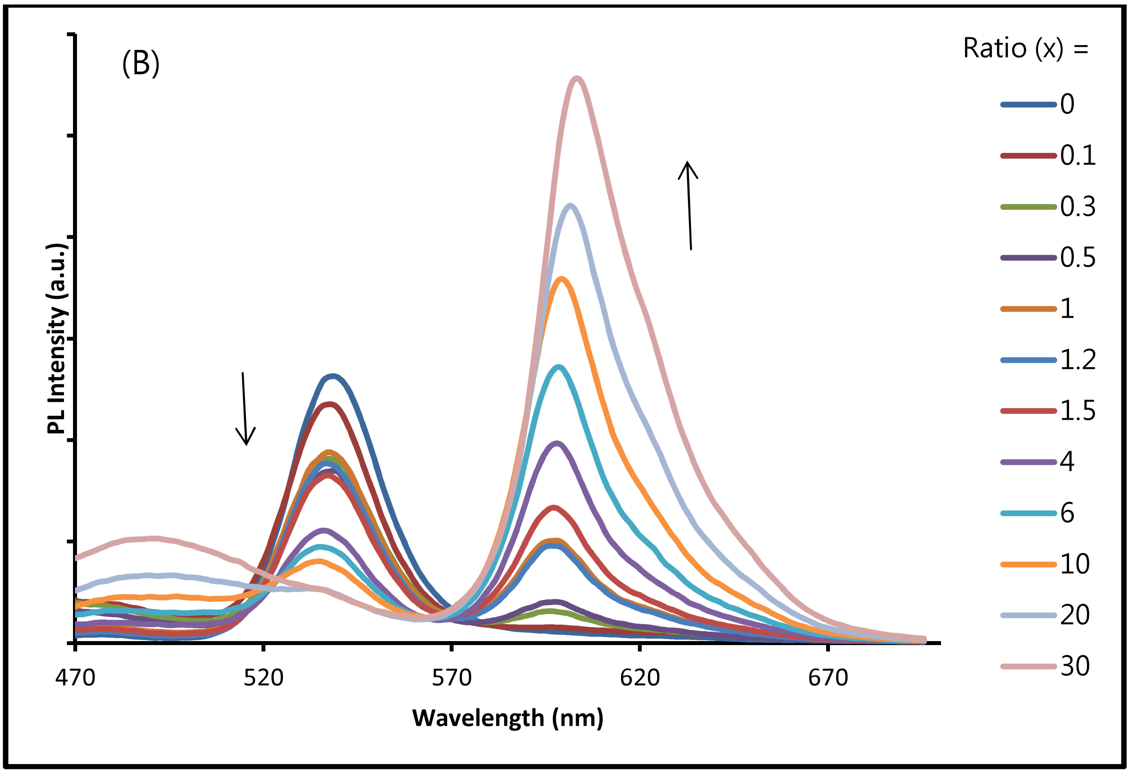

Figure 4.6. Fluorimetric Titration of (A) OQD & (B) GQD with SubPc.

Figure 4.6 captures the photoluminescence spectra of GQD and OQD as a function of added SubPc at different SubPc : CdSe molar ratios (x). To keep the direct excitation of the SubPc molecules as low as possible, the QDs were excited at 450 nm, i.e. at the SubPc absorption minimum between the Soret and the Q bands. The concentrations of the solutions and the number of additions were chosen such that the ratio of the molar concentrations (x) would vary over a wide range. It can be observed that the intensity of the emission band of CdSe QDs shows a monotonic decrease i.e. quenching, whereas, the SubPc showed a systematic enhancement of emission intensity with increase in the molar ratio x and goes well-above the initial QD peak (at x=0).

A separate plot of the change in SubPc emission peak intensity is shown in Figure 4.7. Although the direct absorbance of SubPc was minimized, by selecting the excitation wavelength to be 450 nm, emission of pure SubPc was measured at an excitation wavelength 450 nm, corresponding to every mole ratio.

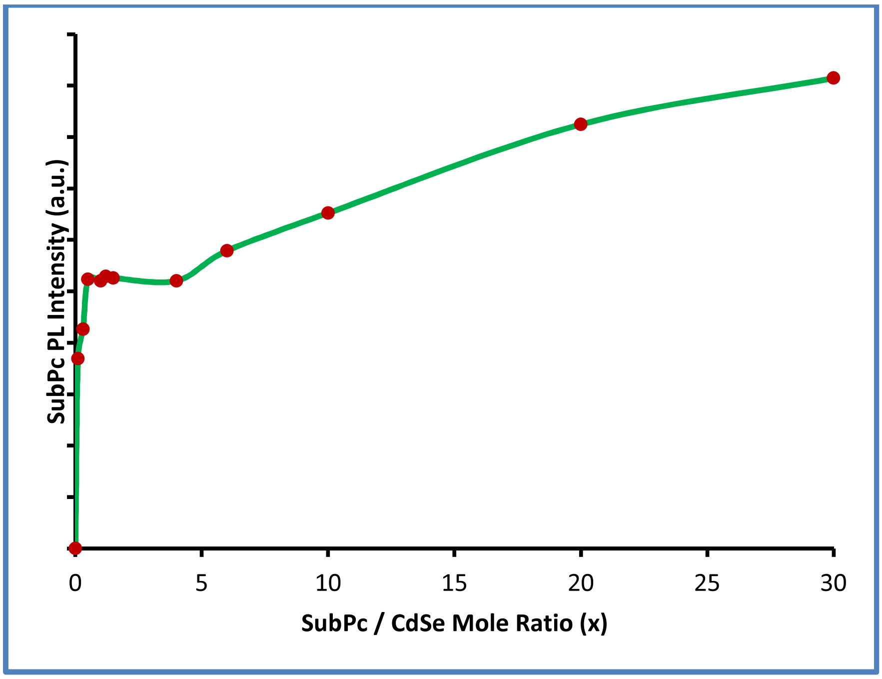

Figure 4.7. Change in SubPc PL peak intensity with Sub : CdSe mole ratio.

The SubPc peak in the CdSe-SubPc complex was de-convoluted through curve fitting and then subtracting the emission of pure SubPc due to direct absorbance (not via CdSe) at 450 nm. The increase in SubPc intensity with increasing mole ratio (x), shows a steep increase at low x values and then slowly levels off around x = 0.5-1.5, and finally again increases with a lower slope. The curve looks like a titration curve, which signifies that at low x values the nanoparticles are coordinatively unsaturated and all of the added SubPc molecules form CdSe-SubPc conjugates. Even at that extent of dilution, effective energy transfer from the CdSe to the SubPc could be possible if the SubPc molecules are bound to the CdSe surface and are thus close enough to each other. With an increase in x values, the nanoparticles get saturated and the saturation point is an indication of the average number of SubPc molecules accommodated around each CdSe particle (*vide infra*). At higher x values, due to the presence of a large excess of SubPc, the slope of the line decreases. These observations led us to hypothesize that efficient energy transfer from QD (donor) to SubPc (acceptor) is probably occurring through a FRET mechanism, which is further confirmed in the next section.

4.6.3 Is A FRET Mechanism in Operation?

To gain more insight into the energy transfer mechanism, the emission peak intensity of SubPc (de-convoluted) in the CdSe-SubPc complex was compared with that of the pure SubPc (without any CdSe), made up to the same concentration as was used in different mole ratios (x) of SubPc : CdSe mixture. The SubPc PL peak in the SubPc : CdSe mixture always showed a higher intensity than that of the pure SubPc, excited directly either at 450 nm (Fig. 4.8) or 400 nm. 400 nm was used (in addition to 450 nm) for comparison, because pure SubPc absorbs 41 times more at 400 nm than at 450 nm (i.e. the 450 nm absorbance is 98% less than the 400 nm absorbance); the SubPc intensity in the complex enhances so much that it even surpasses the absorbance of pure SubPc at 400 nm.

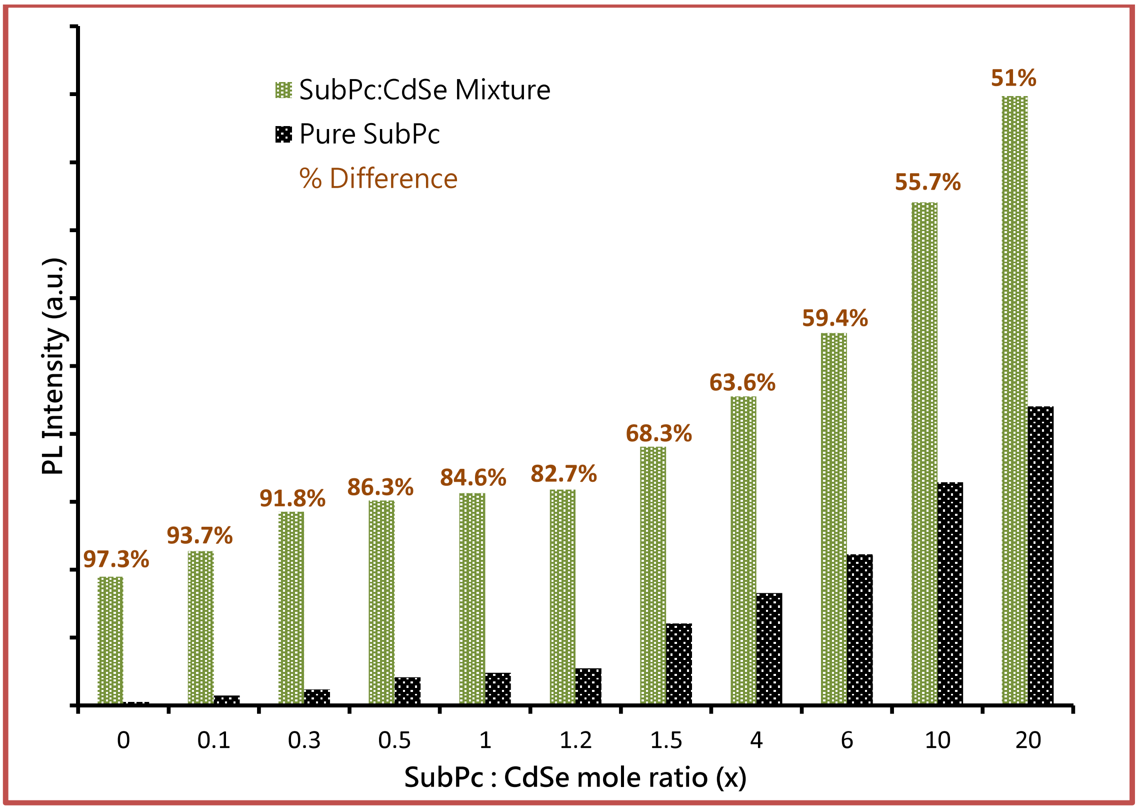

Figure 4.8. Comparison of SubPc PL intensity in the SubPc : CdSe mixture with pure SubPc, excited at 450 nm.

These observations clearly show the fluorescence enhancement effect for the SubPc molecules, which in other words, is FRET. Similar results have been observed in some CdSe-porphyrin systems by other research groups.[28] By contrast, some QD-porphyrin systems showed diminished fluorescence of both the QD and porphyrin, where the energy transfer mechanism was attributed to non-FRET pathways (mainly through electron-hole transfer).[30]

4.6.4 FRET versus Reabsorption

Another obvious question arises in this context of energy transfer in our CdSe-SubPc nanoassemblies – can it be simple reabsorption instead of FRET? The QDs emit at wavelengths where the SubPc shows good absorption; it might therefore be possible that the SubPc molecules are simply absorbing the emitted light, thereby, reducing the light reaching at the detector, which then gives the appearance of quenching.

To address this issue, we carried out a titration experiment with GQDs and unsubstituted SubPc (UsubPc), which has the same core as that of SubPc, but not any anchoring pyridine groups at its periphery. Therefore, there is no scope for the UsubPc to bind to the CdSe QDs. The two systems viz. GQD-UsubPc and GQD-SubPc were then compared. If it had been a simple reabsorption, the light emitted by the GQD at 537 nm would be absorbed directly by the SubPc or UsubPc, to an extent depending on their molar absorptivity values (ε). Molar absorptivity values of SubPc and UsubPc at 537 nm are as follows:

$$\text{SubPc} = 25851\ \text{M}^{-1}\ \text{cm}^{-1} \qquad \text{UsubPc} = 30431\ \text{M}^{-1}\ \text{cm}^{-1}$$

Since, ε for UsubPc is larger than that of SubPc at 537 nm, if it had been reabsorption, the UsubPc would be expected to absorb and emit more than SubPc at any given molar ratio.

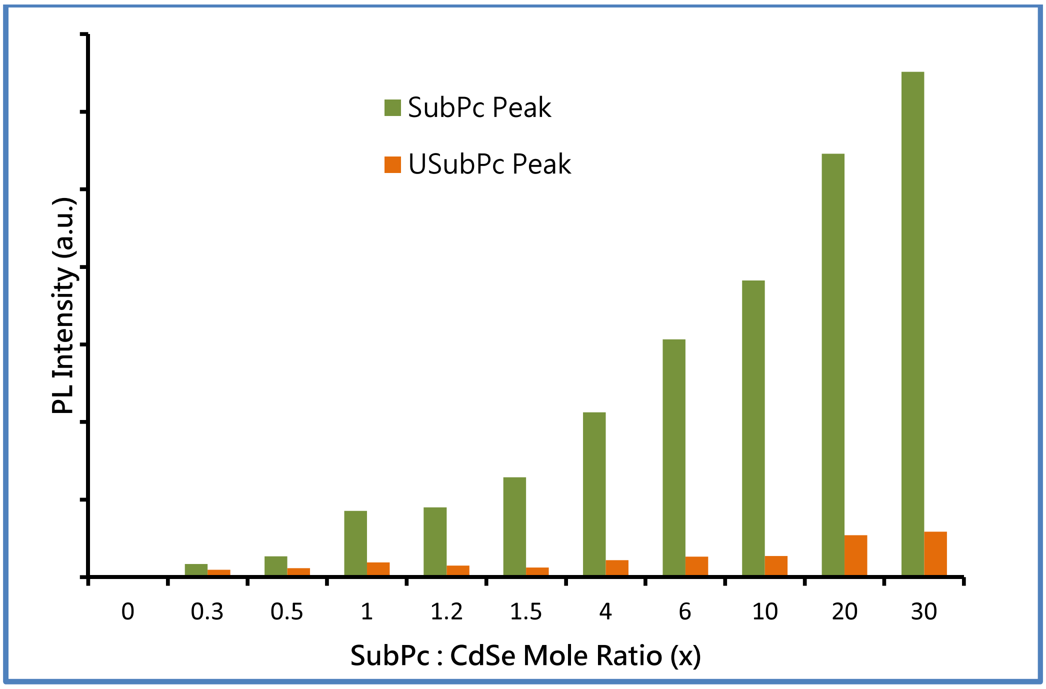

Figure 4.9. Comparison of PL intensities of SubPc & UsubPc peaks in the mixture.

Figure 4.9, shows a comparison of the intensity of the emitted light by SubPc and UsubPc. In every case, it was found that the SubPc emission exceeds far more than that by UsubPc. This fluorescence enhancement is possible only if energy is transferred through a FRET pathway.

Additionally, a closer look at Figure 4.6 reveals that, the light emitted by SubPc in both OQD and GQD systems goes well above the intensity of blank CdSe (at $x = 0$). The maximum light that can be emitted by CdSe is at molar ratio, $x = 0$. If simple reabsorption was taking place, then the maximum light intensity emitted by the SubPc would also be equal to that emitted by CdSe at $x = 0$. The higher light intensity emitted by the SubPc, thus shows that the PL observations are not based on reabsorption.

4.6.5 Comparison of FRET in OQDs and GQDs

To support our hypothesis regarding FRET, one more salient feature of FRET becomes important to investigate. This is known as the spectral overlap integral. The spectral overlap integral, $J(\lambda)$, is defined as the extent of overlap of the emission peak of the donor and the absorbance peak of the acceptor and is calculated as:

$$J(\lambda) = \int_0^{\infty} F_D(\lambda)\varepsilon_A(\lambda)\lambda^4 \, d\lambda,$$

where, $F_D(\lambda)$ is the normalized donor emission and $\varepsilon_A(\lambda)$ is the extinction coefficient of the acceptor. A good spectral overlap between the CdSe QDs and the SubPc molecule is paramount to high energy transfer efficiency through the FRET mechanism.

If FRET is the primary energy transfer mechanism in a system, then any variation of the spectral overlap between the donor and the acceptor would also bring changes in the efficiency of energy transfer. It will be prudent to apply this criterion into our system to confirm that FRET is the leading energy transport pathway. Due to the quantum size effect, luminescence spectra of QDs depend on the size of nanocrystals. Therefore, by simply tuning the size of our CdSe nanocrystals, we should be able to alter the degree of overlap between the CdSe QDs and the SubPc molecule and thereby, the energy transfer efficiency between them. To study this effect, two differently sized CdSe QDs, viz. the GQD and the OQD systems were compared with a single acceptor, the SubPc.

It is always more advantageous to use donor (QD here) quenching results than acceptor (SubPc here) PL enhancements when doing any strict quantitative determination, such as FRET efficiency and other data calculations. This is because of the simplicity of the donor quenching results and the signal does not need to be adjusted by other parameters. By contrast, acceptor fluorescence enhancement signal requires additional adjustment to account for any direct excitation or overlapping of donor emission. Generally, by de-convoluting the PL curve or by adjusting the extinction coefficients of the donor and acceptor at the excitation wavelength, the results are calculated.

Figure 4.10 shows a comparison of the quenching of the CdSe relative peak intensity (I_x / I_0 , where I_x is the CdSe intensity at molar ratio x and I_0 is the CdSe intensity in absence of SubPc) for both GQD & OQD conjugates. It can be observed that overall the CdSe peak gets quenched more in OQD than that in GQD, though the difference in quenching become smaller at higher SubPc : CdSe molar ratio.

This can be explained in terms of overlap integral between SubPc and the two types of CdSe QDs. Spectral overlap calculated for the two types of CdSe are:

$$\text{OQD} = 4.2 \times 10^{-13}\ \text{cm}^3\ \text{M}^{-1} \quad \text{and} \quad \text{GQD} = 2.28 \times 10^{-13}\ \text{cm}^3\ \text{M}^{-1}.$$

The OQD, with a larger overlap integral, should be able to transfer energy more efficiently than the GQD, to the SubPc molecule. Thus, OQDs in general, show a larger quenching than the GQDs. At low molar ratio, when the QDs are coordinatively unsaturated, the effect of this

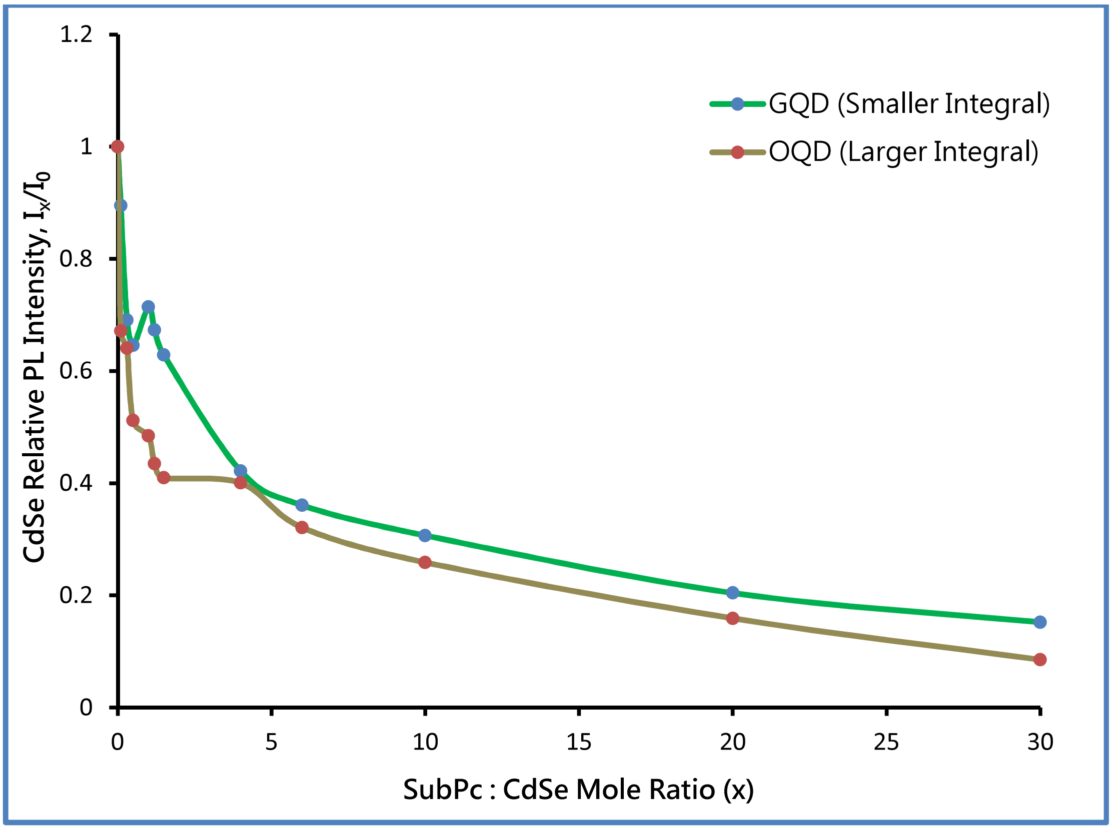

Figure 4.10. Comparison of CdSe relative PL peak intensity in OQD & GQD

quenching and spectra overlap effect is very pronounced, but as the number of SubPc molecules increases i.e. at a high molar ratio, where SubPcs are present in large excess, the QDs are already coordinatively saturated, and the spectral overlap becomes less significant. This change in quenching behavior, depending on the spectral overlap, conclusively proves that in our system, FRET is the primary mechanism of energy transfer.

4.6.6 Number of SubPc Molecules per QD Particle

The operation of FRET in the current CdSe-SubPc system confirms the formation of nanoassemblies between the QDs and the SubPc molecules. However, this fact opens up a new question: In the afore-mentioned nanoassemblies, how many SubPc molecules are then attached to one CdSe nanoparticle? This basic question, though apparently simple and trivial, becomes extremely challenging to get the right answer. The main reason is because the surface of the particles is always covered with an unknown number of stabilizing surfactant molecules. The number of these surfactants replaced by any other ligand is not known. Moreover, each particle in an ensemble can also house different numbers of ligands. No MALDI-TOF mass spectrometry could be done because the heavy nanoparticles do not seem to fly within the MALDI chamber. Simple gravimetric analysis methods fail because of the uncertainties in the number of attached stabilizing surfactants. Even the molar absorptivity values of nanoparticles changes with size and differ in each system. Zenkevich *et al.* tried to estimate the number of porphyrins per QD (1:1 ratio) through qualitative arguments from spectral changes, but no unambiguous experimental proof was provided.[29] Orlova *et al.* estimated the number of porphyrins per QD (4:1 ratio) through theoretical modeling and fitting of an exponential curve with the experimental data.[4] Bawendi' s group determined the number of proteins attached to each CdSe-ZnS core-shell nanocrystal (19:1 ratio) through theoretical modeling, considering each protein moiety as close packed spheres (though crystal structure shows that they are rather ellipsoidal) around the QDs, and found some discrepancies when the data are compared with the values from the titration curve.[22]

In the current research, to find the number of SubPc molecules attached to our CdSe QDs, we were inclined more toward an experimental than a theoretical approach. Finally we compared our findings, with the titration curve in Figure 4.7 and NMR data discussed in section 4.6.10. To the best of our knowledge, no such approach was reported in the past and could turn out to be useful for many systems, where a collisional quenching mechanism is in operation and common experimental methodologies fail.

Our approach was to add a known amount of large excess of SubPc to a known amount of CdSe QD and let the complex form over a few hours, so that every QD gets coordinatively saturated. Then, after isolating the SubPc-QD complex, it was subjected to several washings with an appropriate solvent (acetone), which will preferentially dissolve the excess SubPc, but not the QDs. Finally, recording UV-visible spectra on the washings and the complex, an estimate of the ligand-to-QD ratio can be obtained from the known initial amounts (assuming that the extinction coefficient of the SubPc does not change on binding). In this approach, acetone was used as the washing solvent. Acetone is well-known to precipitate CdSe particles and also was used in the isolation-purification of our nanoparticles (see Chapter 3), whereas, the SubPc molecules are highly soluble in acetone. The washing was continued, till no purple coloration of SubPc was seen in the washing and UV showed no considerable SubPc peak. Though blank nanocrystals are insoluble in the chosen solvent, the complexation of the QDs with the SubPc molecules changes the surface environment of the nanocrystals and makes the nanocrystals soluble. This solubility supports the notion that CdSe-SubPc nanoassemblies have been formed.

Figure 4.11 and 4.12 respectively show the UV-Visible and PL spectra of washings and of the complex. The filtrate (from which the complex was isolated) and the first washing combination, shows exclusively the peak of excess SubPc that was not bonded to the QD. The second washing contains the peak of both CdSe and SubPc of the complex, though negligible amount, due to sparing solubility. No further washing was done to prevent compound loss. The isolated complex was then dissolved in $CH_2Cl_2/CHCl_3$, and shows strong peaks of CdSe and SubPc.

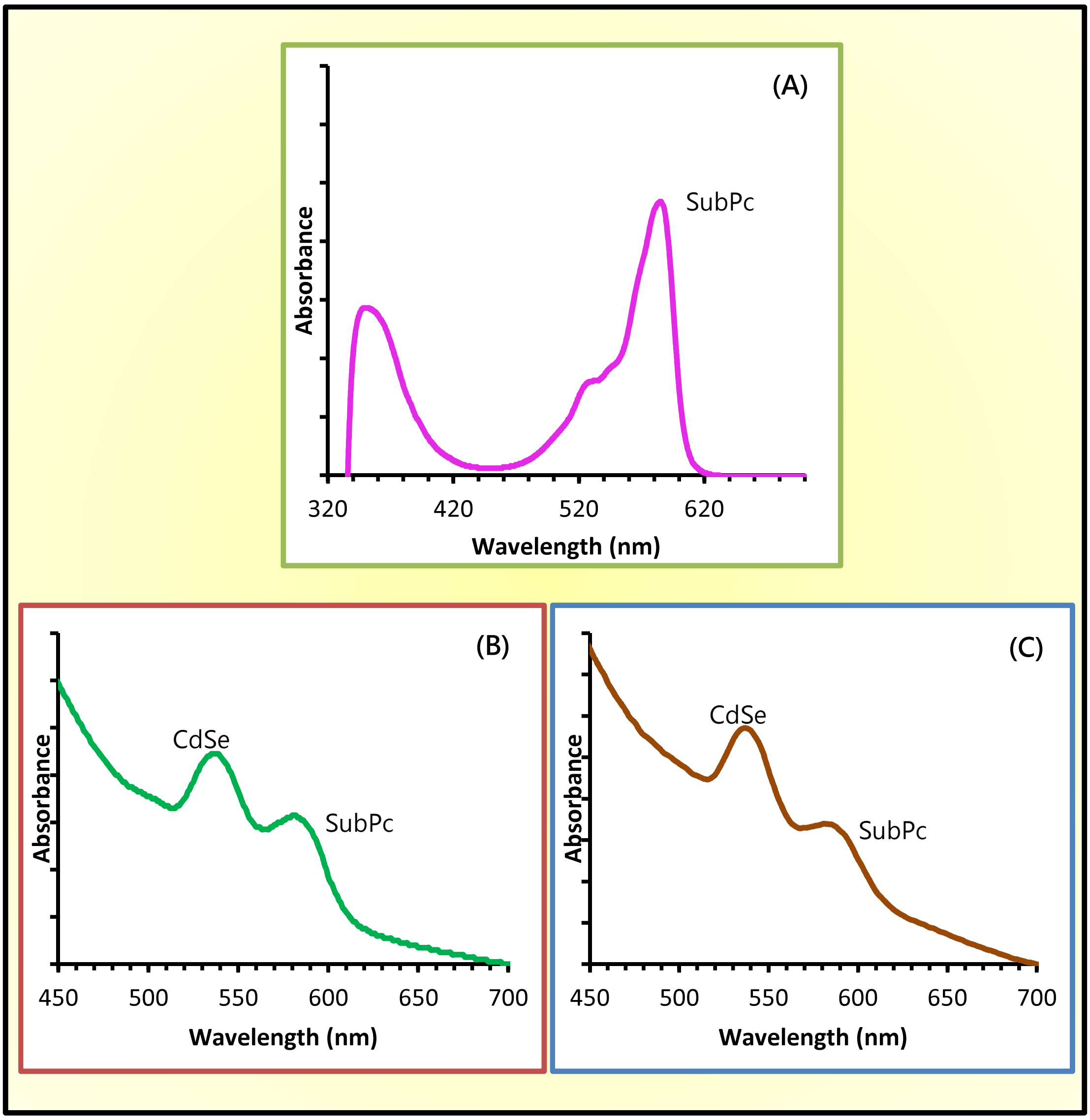

Figure 4.11. UV-Visible spectra of (A) filtrate + 1st washing, (B) 2nd washing and (c) isolated complex.

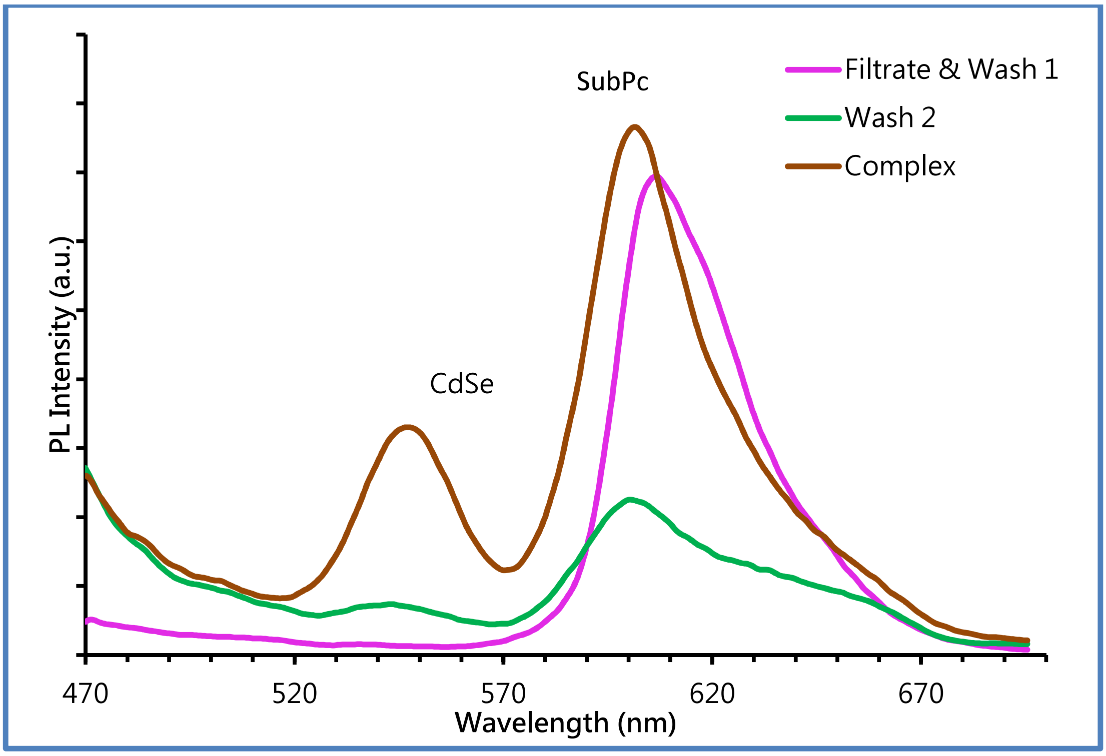

Figure 4.12. Photoluminescence spectra of filtrate + 1st washing, 2nd washing and the complex.

Calculations of [SubPc] / [CdSe] Ratio:

(i) Complex in Wash 2--

$A_{SubPc} / A_{CdSe} = \varepsilon_{SubPc} [SubPc] L / \varepsilon_{CdSe} [CdSe] L,$

Where, ε = molar absorptivity; L = path length

Or, 0.062/0.089 = 76413 [SubPc] / 89669.35 [CdSe]

$\therefore$ [SubPc] / [CdSe] = 0.8 ≡ 1

(ii) Similarly in the Isolated Complex--

[SubPc] / [CdSe] = 0.7 ≡ 1

(iii) From Filtrate & Wash 1--

Initial amount of SubPc = 3.29 x 10^{-6} moles (16.5 times excess of Cdse)

SubPc washed out (filtrate & wash 1) = 3.06 x 10^{-6} moles

SubPc left back in the complex = (3.29-3.06) x 10^{-6} moles

= 0.23 x 10^{-6} moles

Initial amount of CdSe = 2 x 10^{-7} moles

∴ [SubPc] / [CdSe] = 0.23 x 10^{-6} / 2 x 10^{-7} = 1.15 ≡ 1

The average number of one SubPc attached to one CdSe matches very well among all the above three cases (within experimental error). To confirm ourselves that the isolated complex is a representative sample, three more washings were continued and in every case the same features of CdSe and SubPc absorption peaks were observed.

When the outcome of this washing experiment was compared with the titration curve in Figure 4.7, it can be seen that there is an excellent agreement between the two results. The rising titration curve starts to form a short asymptotic plateau from mole ratio 0.5 to 1.5, which signifies that at that region the QDs starts to get coordinatively saturated. The average of this plateau region (x = 0.5, 1, 1.2, 1.5), which denotes the saturation point, is 1.05 ≡ 1, agrees well with the above findings.

Similar results were also obtained from NMR titration (*vide* Section 4.6.10). Thus, we can assume, that *one SubPc molecule is attached to one CdSe QD*, to form a *nano*assembly in the current work.

4.6.7 Are Nanoassemblies formed? Calculation of Association Constant (K)

The SubPc molecule is expected to bind to the CdSe QDs through its peripheral meta-pyridyl rings attached to the alkyne bond. It is expected that it would replace the monodentate stabilizing surfactants (oleylamine, may be TBPO – refer Chapter 3) with its multiple pyridyl groups to form a more stable chelate complex. If such a nanoassembly is formed, then it is also possible to determine the association constant (K) between the SubPc ligand and the QDs.

This model assumes that the QDs get coordinatively saturated in the complex with SubPc : QD at 1:1 ratio, thus a bimolecular reaction is in effect. In many porphyrin systems, Poisson distribution was considered, where bimolecular reaction was not confirmed.[4] Our model assumes a dynamic equilibrium is set up between the uncomplexed CdSe particles (Q), the complex (QL) and the uncomplexed SubPc molecules (L).

$$Q + L \overset{K}{\rightleftarrows} QL$$

$K = [QL] / [Q] [L]$ .... (1)

$= [QL] / [Q] ([L^*]-[QL])$, where $[L^*]$ = added concn. of SubPc .... (2)

At a high concn. of SubPc (high x values), $[L^*]>>[QL]$. Therefore, eqn (2) becomes,

$K = [QL\} / [Q] [L^*]$.................................... .... (3)

Now let α be the degree of association. By definition,

$\alpha = [QL] / ([Q \text{ uncomplexed}] + [Q \text{ complexed}])$

$= [QL] / ([Q] + [Q \text{ complexed}])$

$= [QL] / ([Q] + [QL])$, since $[Q \text{ complexed}] = [QL]$................. (4)

At higher ratio (x), using $K = [QL] / [Q] [L^*]$ from eqn (3) into eqn (4),

$\alpha = K [Q] [L^*] / ([Q] + [QL])$

$= K [L^*] / (1 + [QL] / [Q])$

$= K [L^*] / (1 + K [L^*])$.. (5)

According to He *et al.*,[34] Jhonsi *et al.*,[35] Kamat *et al.*,[36] the fluorescence intensity can be related to the degree of association, α by the following relation-

$I^{obs} = (1 - \alpha) I^0 + \alpha I'$,

where, I^{obs} = observed fluorescence of the complex, I^0 = fluorescence of initial QD (at x=0), and I' = fluorescence of the complexed QD.

Or, $I^{obs} = I^0 - \alpha I^0 + \alpha I'$

Or, $I^0 - I^{obs} = \alpha (I^0 - I')$............................(6)

Now, substituting the value of α from eqn (5) into eqn (6), we get,

$I^0 - I^{obs} = \{(K [L^*] / (1 + K [L^*])\} (I^0 - I')$

Or, $1 / (I^0 - I^{obs}) = (1 + K [L^*]) / \{K [L^*] (I^0 - I')\}$

$= 1 / \{K [L^*] (I^0 - I')\} + 1 / (I^0 - I')$

If the above quenching phenomenon is due to the association of CdSe and SubPc, forming nanoassemblies at 1:1 ratio, it would be expected that $1/(I^0 - I^{obs})$ would depend linearly on the reciprocal concentration of SubPc. The ratio of the intercept and the slope should yield the K value.

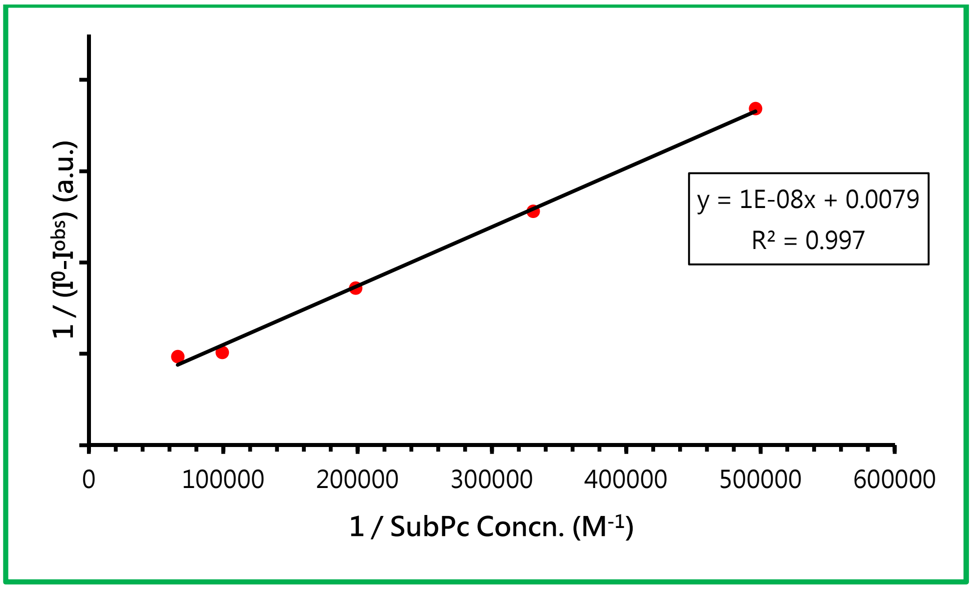

Figure 4.13. Dependence of 1/(I^0-I^{obs}) on 1/SubPc concn. in GQD.

Figure 4.13 shows that there is an excellent linear dependence ($R^2 = 0.997$). The K value was calculated to be 7.9 X 10^5 M^{-1}. The K value is either higher or comparable with porphyrin systems reported in literature.[29,34,35] The linear dependence and the high K value is also a proof that there is a strong association between the CdSe NPs and the SubPc ligand through the formation of chelate complex-probably the pyridyl nitrogen lone pair is donated to Cd vacant orbital.

4.6.8 Stern-Volmer Plot

A Stern-Volmer plot is a linear plot of I^0/I^{obs} vs. concentration of the quencher (SubPc here) [L], with an intercept = 1. The Stern-Volmer equation is-

$I^0 / I^{obs} = 1 + K_{SV} [L]$

A linear Stern-Volmer plot is generally indicative of a single class of fluorophore (CdSe), which are equally accessible to the quencher (SubPc). If two fluorophore populations are present, and one class is not accessible to the quencher, then the Stern-Volmer plots deviate from linearity toward the x-axis. This result is frequently found for the quenching of tryptophan fluorescence in proteins by polar or charged quenchers; these molecules do not readily penetrate the hydrophobic interior of proteins, and only those tryptophan residues on the surface of the protein are quenched.[37]

The linearity observed in the current experiment (Figure 4.14), thus might be an indication that the particles are appreciably monodisperse and non-aggregated, giving full exposure to the surface and the surface stabilizing ligands are equally well displaced by the SubPc molecule.

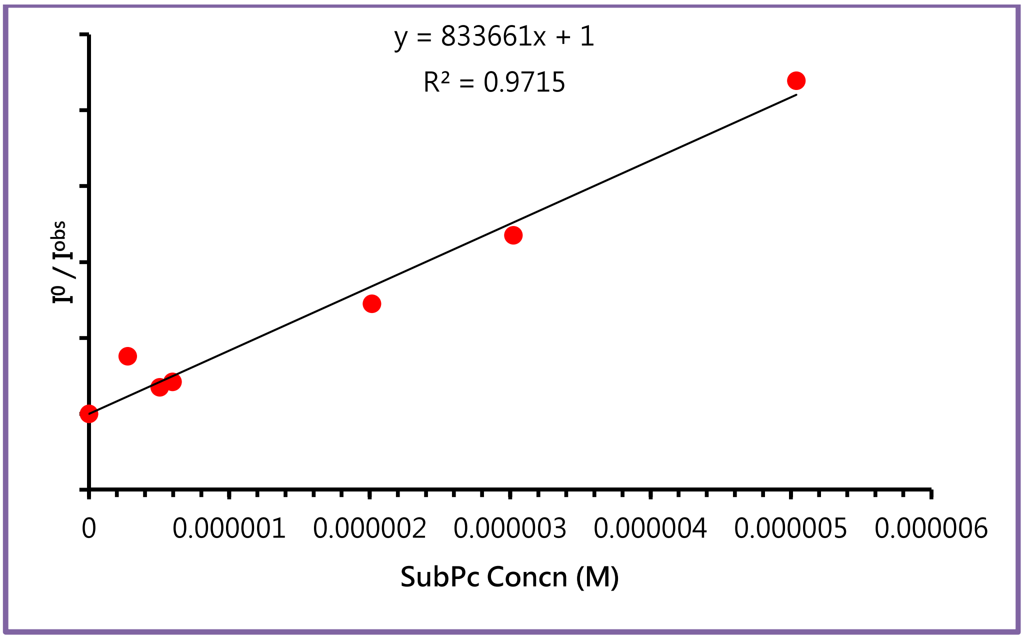

Figure 4.14. A Stern-Volmer plot of CdSe QD-SubPc pair.

4.6.9 Critical Förster Radius & Donor-Acceptor Distance

FRET, sometimes referred to as a spectroscopic microscope[38] or a molecular ruler[39] is very useful to determine molecular distances or to show whether or not molecular complexes are formed.[38] To determine the donor-acceptor intercenter distance (r), knowledge of the critical Förster Radius, R_0 becomes necessary. R_0 is given by the well-known relation:[37]

$$R_0^6 = 9000\,(\ln 10)\,\kappa^2\,Q_D\,J(\lambda)\ /\ 128\,\pi^5\,N\,n^4,$$

where, κ^2 = orientation factor (generally taken as 2/3), Q_D = quantum yield of the donor, $J(\lambda)$ is the overlap integral, N = Avogadro's number and n = refractive index of the medium (1.4 for CH_2Cl_2). The quantum yield of 2.68 and 3 nm CdSe QDs (GQD & OQD, respectively) was taken as unity (reported w.r.t. Rhodamine 6G) from the literature.[4,9,40]

R_0 calculated for the two types of CdSe are:

$$\text{OQD} = 59\ \text{Å} \quad \text{and} \quad \text{GQD} = 53\ \text{Å}.$$

The donor-acceptor separation distance (r), is related to the energy transfer efficiency (E) through the following equation:[7,37]

$$E = R_0^6 / (r^6 + R_0^6)$$

E is related to the fluorescence intensity through the relation:[37]

$$E = 1 - (I / I^0),$$

where, I = fluorescence intensity of donor in the presence of acceptor and I^0 = fluorescence intensity of donor in the absence of the acceptor.

The value of r is calculated for the highest mole ratio (x = 30), where CdSe is assumed to be completely quenched. The r values for the two types of CdSe QD are 3.7 nm (OQD) and 3.2 nm (GQD). The obtained r values for both OQD and GQD, are well within the typical FRET range of 0.5-10 nm,[38] and shows that the current CdSe-SubPc pair fulfills the pre-requisite for FRET.

4.6.10 NMR Titration to Identify CdSe-SubPc Nanoassemblies

To make the final conclusive remarks regarding the formation of CdSe-SubPc nanoassemblies and the number of SubPc attached per nanoparticle, a ^{1}H NMR study was initiated. It is difficult to get direct NMR spectra either of CdSe particles or the complex itself, probably due to reduced rotational freedom of SubPc, a variety of different microenvironments or different orientations of the attached molecules w.r.t. the particle surface. Therefore, we studied the decrease of the signal intensity of free SubPc molecules, due to the formation of nanoassemblies, with addition of CdSe QDs. The meta-pyridyl ring protons are studied, via their integration ratio w.r.t. an internal standard (ferrocene, normalized to 1, δ 4.2). Ferrocene was taken in such a quantity so that both SubPc and ferrocene show comparable proton integrals. Ferrocene was chosen as the internal standard because it is a solid and easy to weigh, it does not react with our system, shows no chemical shift or intensity change, and does not interfere with any sample peak.

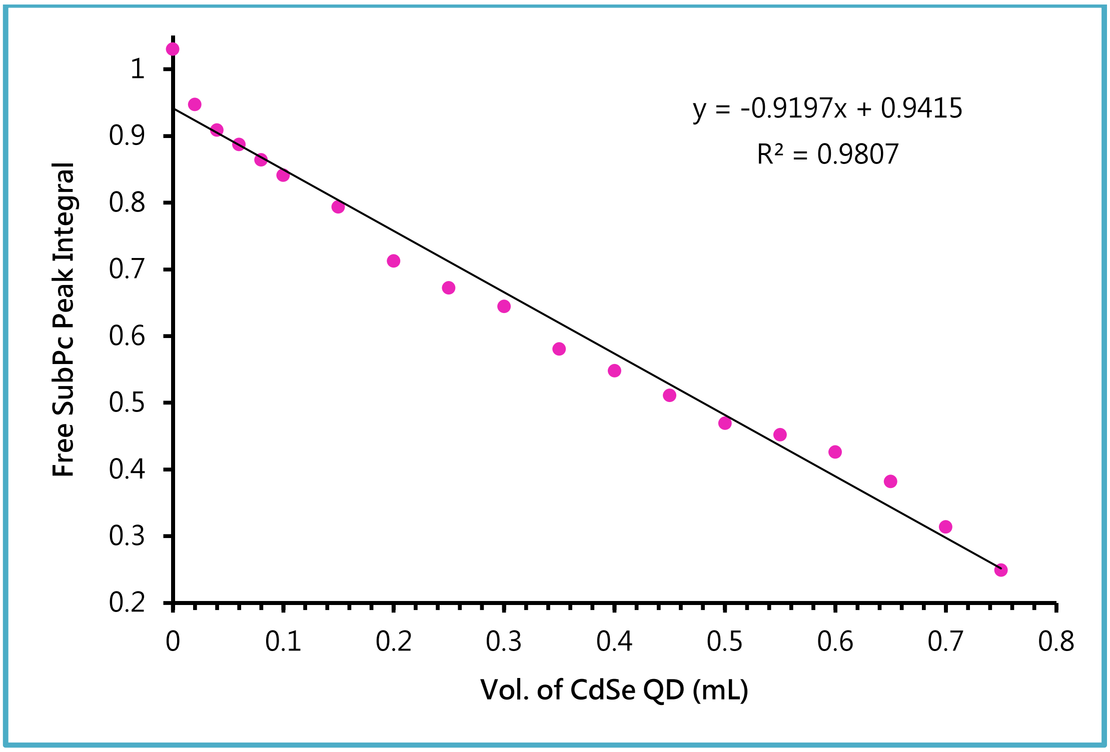

Figure 4.15. NMR titration of SubPc with CdSe QD.

Figure 4.15 shows the titration curve of a fixed amount of SubPc with increasing amount of CdSe added directly into the NMR tube. To capture the initial effect, the first 5 additions were made 20 µL each and the subsequent 13 additions were 50 µL each. The graph shows that the pyridyl ring integral decreases steadily in a linear fashion with increasing addition of CdSe QD. For a visual relish, Figure 4.16 is also included, with overlaid selected spectra, all scaled to the same intensity of the ferrocene peak for easy visual comparison. The meta pyridyl ring peaks are followed (red circle).

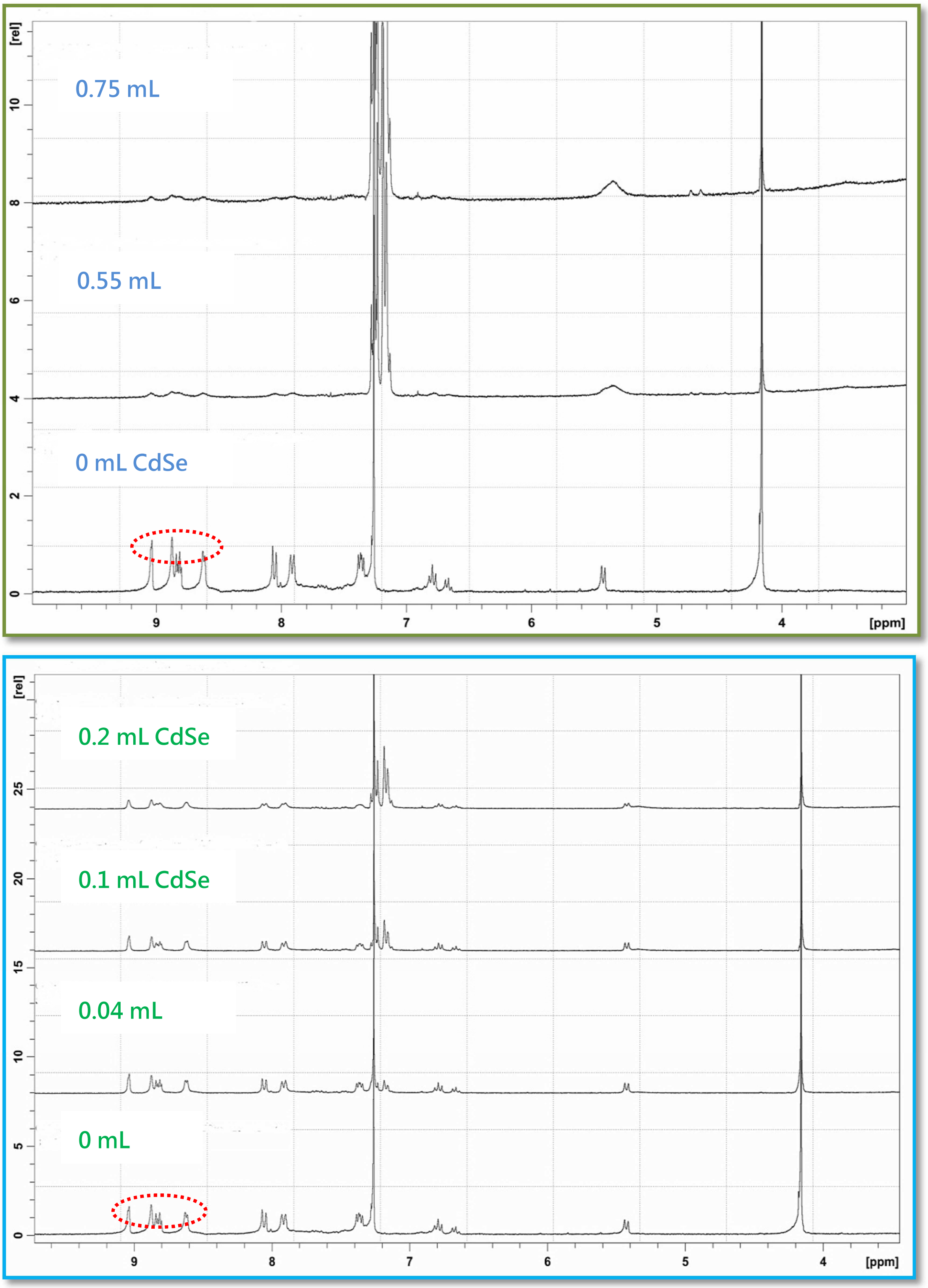

Figure 4.16. NMR titration of SubPc at various additions of CdSe QD.

From the knowledge of the amount of ferrocene taken and the integral values of the SubPc after each CdSe addition, it is possible to calculate how much SubPc has reacted with every known addition of QD, which in turn, allows us to estimate the no. of SubPc per CdSe QD. The average of all 19 additions returns a value of: Number of SubPc per QD = 1.08 ≡ 1, which is the same as obtained from other separate experiments. The systematic decrease of the signals of free SubPc implies that they are increasingly bonded to the CdSe surface.

Even addition of a 317 fold excess tributylphosphine (w.r.t. SubPc) to the NMR tube (with sonication) does not restore the SubPc peak intensity to its initial value, instead only a 15% increase is seen.

If the NMR tube is left undisturbed over a period of time, the free SubPc peak again starts to decrease and reaches the minimum as observed during the titration. This suggests that SubPc forms a thermodynamically more stable complex through chelation and even if it gets replaced by excess TBP, over a period of time it binds back to the nanoparticles, thereby decreasing the free SubPc peak in the tube. These observations also rule out any assumption that the decrease of integral values of SubPc is due to any decomposition or sample loss in some way.

Table 4.1 compares the number of SubPc per QD obtained from fluorimetric titration, NMR Studies and washing experiment by UV-Visible spectroscopy, which agree very well with each other.

Table 4.1. Comparison of no. of SubPc per QD obtained from different experiments

Parameter	Fluorimetry	NMR	UV-Visible
No. of SubPc per QD	1.05 ≡ 1	1.08 ≡ 1	(i) 0.8 ≡ 1 (ii) 0.7 ≡ 1 (iii) 1.15 ≡ 1

The NMR experiments unequivocally prove that a stable nanoassembly has formed between the CdSe NP and the SubPc molecules, through the three anchoring meta-pyridyl groups in a 1:1 ratio.

4.6.11 An Unusual Behavior of ZnSe QDs toward SubPc Molecules

Since no optical studies (UV-Vis and Fluorescence) could be performed on ZnSe-SubPc system, an NMR study, similar to that of CdSe, was conducted. Surprisingly, it was found that there was no decrease of any SubPc peak with addition of ZnSe QDs (Figure 4.17). This indicates that there is no apparent bonding between SubPc and the ZnSe quantum dots. Zn^{2+}, being harder Lewis acid than Cd^{2+} is expected to bind more strongly with the nitrogen atom (of the meta- pyridyl ring of SubPc) but such bonding is not observed in this case.

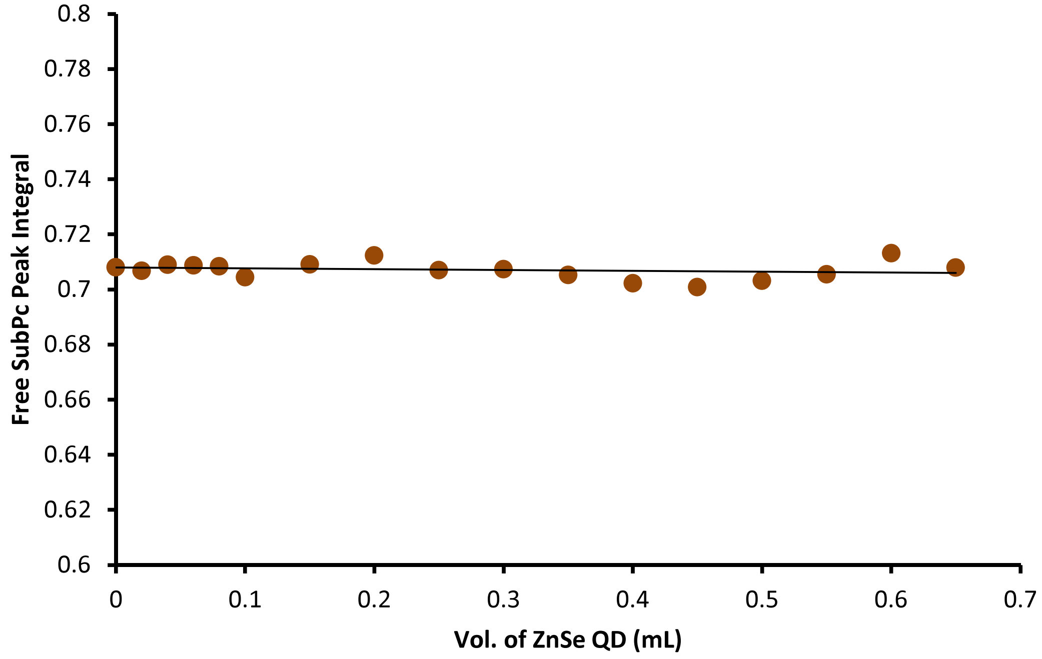

Figure 4.17. NMR titration of SubPc with ZnSe QDs.

Though the reason for such a behavior of ZnSe toward SubPc is not clearly understood, it might be possible that ZnSe is more prone to aerial hydrolysis and oxidation (bond energy: Zn-Se[41] = 136 KJ mol^{-1}) and a Zn-O bond (bond energy: Zn-O[41,42] = 284.1 KJ mol^{-1}) is formed in the process. The Zn-O being much stronger than a Zn-N bond (bond energy: Zn-N[43,44] = 153 KJ mol^{-1}), formation of a Zn-N bond at the expense of a Zn-O bond is less likely to occur.

4.7 CONCLUSIONS

To conclude, an efficient donor-acceptor system has been built with the CdSe QD-SubPc pair for the first time. The energy flow occurs primarily through a FRET mechanism from the QD to the SubPc, showing a decrease of QD luminescence and a simultaneous increase of the SubPc emission. A stable complex is formed between the QD and SubPc, with a comparable or higher association constant than previously reported for porphyrin systems. *The number of SubPc molecules attached per QD was found to be 1* from different techniques. The donor-acceptor distance calculated is well within the range of FRET. NMR studies showed a decrease of free SubPc peak signal intensity on consecutive additions of CdSe QDs, and supported the formation of a stable QD-SubPc complex. However, ZnSe QDs, did not show any evidence of ligand binding.

4.8 EXPERIMENTAL

4.8.1 General Procedures

Cadmium selenide & zinc selenide quantum dots (synthesized in-house, *vide* Chapter 3), tri-substituted and unsubstituted subphthalocyanines (kindly provided by Prof. Andy Cammidge, School of Chemistry, UEA), ferrocene (Aldrich, 98%), tri-butyl phosphine (Aldrich, 97%), $CDCl_3$ (Cambridge Isotope Laboratories, 99.8%), CH_2Cl_2 (Aldrich, 99.5%), Acetone (Aldrich, 99.9%) were used as received.

Dichloromethane was dried over calcium hydride. Acetone was dried over molecular sieves and degassed by several freeze–thaw cycles. Deuterated solvents were stored over activated 4 Å molecular sieves and degassed by several freeze–thaw cycles.

4.8.2 Instrumentation

^{1}H NMR spectra were recorded using a Bruker Avance DPX300 spectrometer at ambient temperatures with 32 scans and pulse delay of 10 ns. Peaks were referenced to solvent peak at δ 7.26 for $CDCl_3$ (δ 0.0 for Me_4Si) - positive values are toward high frequency (downfield).

UV-visible spectra were recorded on a Hitachi U-3010 spectrophotometer, using a quartz cuvette (1 cm or 0.1 cm path length as required).

Steady-state photoluminescence was measured using a Perkin Elmer LS 55 fluorescence spectrometer using quartz cuvette.

4.8.3 Fluorimetric Titration of QDs with SubPc

To study the quenching effect of CdSe QDs with SubPc through fluorimetric titration, 12 glass vials were prepared each with a fixed amount of CdSe and SubPc added at different molar ratios (x) in dichloromethane. All vials were made up to the same final volume of 5 mL. The fluorimetric titration was done at 450 nm excitation wavelength and slit width 5 nm. A typical recipe for OQD is given below in Table 5.2 showing the constituents in each vial.

Table 4.2. Preparation of sample vials with different SubPc : CdSe ratio for fluorimetric titration (All volumes measured by syringes).

Molar Ratio (X)	Volume of CdSe (1.27×10^{-5} M) (mL)	Volume of SubPc (3.45×10^{-5} M) (mL)	Volume of CH_2Cl_2 (mL)	Total Volume of the Solution (mL)
0	0.3	0	4.70	5
0.1	0.3	0.01	4.69	5
0.3	0.3	0.03	4.67	5
0.5	0.3	0.06	4.64	5
1.0	0.3	0.11	4.59	5
1.2	0.3	0.13	4.57	5
1.5	0.3	0.17	4.53	5
4	0.3	0.44	4.26	5
6	0.3	0.66	4.04	5
10	0.3	1.1	3.60	5
20	0.3	2.2	2.50	5
30	0.3	3.3	1.40	5

4.8.4 UV-visible Study of Filtrate and Washings of QDs to Determine the Number of SubPc Molecules Per QD

To a 25 mL 2 neck round-bottomed flask, containing a stirrer bar and wrapped in aluminum foil, was added a freshly prepared solution of CdSe quantum dots in dicholoromethane (10 mL, 2 x 10^{-5} M). Then SubPc (2.6 mg, 3.29 x 10^{-6} moles) was added to it. The amount of SubPc taken was 16.5 fold excess of CdSe particles. The solution was stirred for 2.5 h at room temperature and the complex was then precipitated with methanol (20 mL). After centrifugation, the filtrate was placed in a 100 mL volumetric flask. The precipitate was washed with acetone (5 mL) and the first washing, which shows the pink color of SubPc, was added into the volumetric flask. At this point, the volumetric flask was made up to 100 mL. The precipitate was again washed with 5 mL acetone (second washing) and the acetone layer appeared faintly reddish (no purple coloration of free SubPc). UV spectrum of this second washing was recorded and both the peaks of CdSe and SubPc were found. The final complex was dissolved in a $CH_2Cl_2/CHCl_3$ mixture (4:11, 15 mL) and the UV spectrum recorded. Photoluminescence studies were also carried out.

4.8.5 NMR Studies of CdSe QD and SubPc

To a NMR tube, containing SubPc (1 mg) was added a solution of ferrocene (0.28 mg) in $CDCl_3$ (0.4 mL). An initial spectrum of this mixture was run without any addition of CdSe QD. A freshly prepared solution of CdSe QD in $CDCl_3$ (2.27 mM) was then progressively added to the NMR tube and NMR spectra were recorded after each addition. The first five additions were 20 µL each, and the next thirteen additions were 50 µL each. After 18 additions of CdSe, tributyl phosphine (0.1 mL, 0.4 mmol) was added to the tube, sonicated and NMR spectra recorded.

Manuscript for Publication from Chapter 4 is in Preparation

REFERENCES

(1) Kanelidis, I.; Vaneski, A.; Lenkeit, D.; Pelz, S.; Elsner, V.; Stewart, R. M.; Rodríguez-Fernández, J.; Lutich, A. A.; Susha, A. S.; Theissmann, R.; Adamczyk, S.; Rogach, A. L.; Holder, E. *J. Mater. Chem.* **2011**, *21*, 2656.

(2) Milliron, D. j.; Alivisatos, A. p.; Pitois, C.; Edder, C.; Fréchet, J. m. j. *Adv. Mater.* **2003**, *15*, 58–61.

(3) Jańczewski, D.; Tomczak, N.; Liu, S.; Han, M.-Y.; Vancso, G. J. *Chem. Commun.* **2010**, *46*, 3253.

(4) Orlova, A. O.; Maslov, V. G.; Stepanov, A. A.; Gounko, I.; Baranov, A. V. *Opt. Spectrosc.* **2008**, *105*, 889–895.

(5) Dayal, S.; Li, J.; Li, Y.-S.; Wu, H.; Samia, A. C. S.; Kenney, M. E.; Burda, C. *Photochem. Photobiol.* **2008**, *84*, 243–249.

(6) Mitchell, G. P.; Mirkin, C. A.; Letsinger, R. L. *J. Am. Chem. Soc.* **1999**, *121*, 8122–8123.

(7) Jhonsi, M. A.; Renganathan, R. *J. Colloid Interface Sci.* **2010**, *344*, 596–602.

(8) Moeno, S.; Idowu, M.; Nyokong, T. *Inorg. Chim. Acta* **2008**, *361*, 2950–2956.

(9) Schmelz, O.; Mews, A.; Basché, T.; Herrmann, A.; Müllen, K. *Langmuir* **2001**, *17*, 2861–2865.

(10) Lihitkar, N. B.; Singh, S. B.; Singh, J.; Srivastava, O. N.; Naik, R. H.; Kulkarni, S. K. *Chem. Phys. Lett.* **2009**, *483*, 227–232.

(11) Nyk, M.; Palewska, K.; Kepinski, L.; Wilk, K. A.; Strek, W.; Samoc, M. *J. Lumin.* **2010**, *130*, 2487–2490.

(12) Aldana, J.; Wang, Y. A.; Peng, X. *J. Am. Chem. Soc.* **2001**, *123*, 8844–8850.

(13) Pathak, S.; Choi, S.-K.; Arnheim, N.; Thompson, M. E. *J. Am. Chem. Soc.* **2001**, *123*, 4103–4104.

(14) Querner, C.; Reiss, P.; Bleuse, J.; Pron, A. *J. Am. Chem. Soc.* **2004**, *126*, 11574–11582.

(15) Wang, M.; Oh, J. K.; Dykstra, T. E.; Lou, X.; Scholes, G. D.; Winnik, M. A. *Macromolecules* **2006**, *39*, 3664–3672.

(16) Sharma, R.; Holland, G. P.; Solomon, V. C.; Zimmermann, H.; Schiffenhaus, S.; Amin, S. A.; Buttry, D. A.; Yarger, J. L. *J. Phys. Chem. C* **2009**, *113*, 16387–16393.

(17) Kim, S.; Bawendi, M. G. *J. Am. Chem. Soc.* **2003**, *125*, 14652–14653.

(18) Sudeep, P. K.; Emrick, T. *ACS Nano* **2009**, *3*, 4105–4109.

(19) Luo, X.; Liu, P.; Truong, N. T. N.; Farva, U.; Park, C. *J. Phys. Chem. C* **2011**, *115*, 20817–20823.

(20) Geissbuehler, I.; Hovius, R.; Martinez, K. L.; Adrian, M.; Thampi, K. R.; Vogel, H. *Angew. Chem. Int. Ed.* **2005**, *44*, 1388–1392.

(21) Sill, K.; Emrick, T. *Chem. Mater.* **2004**, *16*, 1240–1243.

(22) Mattoussi, H.; Mauro, J. M.; Goldman, E. R.; Anderson, G. P.; Sundar, V. C.; Mikulec, F. V.; Bawendi, M. G. *J. Am. Chem. Soc.* **2000**, *122*, 12142–12150.

(23) Narayanan, S. S.; Sarkar, R.; Pal, S. K. *J. Phys. Chem. C* **2007**, *111*, 11539–11543.

(24) Binder, W. H.; Sachsenhofer, R.; Straif, C. J.; Zirbs, R. *J. Mater. Chem.* **2007**, *17*, 2125.

(25) Dayal, S.; Lou, Y.; Samia, A. C. S.; Berlin, J. C.; Kenney, M. E.; Burda, C. *J. Am. Chem. Soc.* **2006**, *128*, 13974–13975.

(26) Hone, D. C.; Walker, P. I.; Evans-Gowing, R.; FitzGerald, S.; Beeby, A.; Chambrier, I.; Cook, M. J.; Russell, D. A. *Langmuir* **2002**, *18*, 2985–2987.

(27) Samia, A. C. S.; Chen, X.; Burda, C. *J. Am. Chem. Soc.* **2003**, *125*, 15736–15737.

(28) Zenkevich, E.; Cichos, F.; Shulga, A.; Petrov, E. P.; Blaudeck, T.; Von Borczyskowski, C. *J. Phys. Chem. B* **2005**, *109*, 8679–8692.

(29) Zenkevich, E. I.; Blaudeck, T.; Shulga, A. M.; Cichos, F.; Von Borczyskowski, C. *J. Lumin.* **2007**, *122-123*, 784–788.

(30) Frasco, M. F.; Vamvakaki, V.; Chaniotakis, N. *J. Nanopart. Res.* **2010**, *12*, 1449–1458.

(31) Kuçur, E.; Boldt, F. M.; Cavaliere-Jaricot, S.; Ziegler, J.; Nann, T. *Anal. Chem.* **2007**, *79*, 8987–8993.

(32) Striolo, A.; Ward, J.; Prausnitz, J. M.; Parak, W. J.; Zanchet, D.; Gerion, D.; Milliron, D.; Alivisatos, A. P. *J. Phys. Chem. B* **2002**, *106*, 5500–5505.

(33) Yu, W. W.; Qu, L.; Guo, W.; Peng, X. *Chem. Mater.* **2003**, *15*, 2854–2860.

(34) He, X.; Zhou, Y.; Zhou, Y.; Zhang, M.; Shen, T. *J. Colloid Interface Sci.* **2000**, *225*, 128–133.

(35) Jhonsi, M. A.; Kathiravan, A.; Renganathan, R. *SpectroChim. Acta A* **2008**, *71*, 1507–1511.

(36) Kamat, P. V. *J. Phys. Chem.* **1989**, *93*, 859–864.

(37) Lakowicz, J. R. *Principles of Fluorescence Spectroscopy*; 3rd ed.; Springer: New York, 2006.

(38) Clegg, R. M. *Laboratory Techniques in Biochemistry and Molecular Biology, (FRET and FLIM techniques)*; Gadella, T. W. J., Ed.; Elsevier: Amsterdam; London, 2009; Vol. 33.

(39) Stryer, L. *Annu. Rev. Biochem.* **1978**, *47*, 819–846.

(40) Orlova, A. O.; Gubanova, M. S.; Maslov, V. G.; Vinogradova, G. N.; Baranov, A. V.; Fedorov, A. V.; Gounko, I. *Opt. Spectrosc.* **2010**, *108*, 927–933.

(41) Lange, N. A. *Lange′s Handbook of Chemistry.*; Speight, J. G., Ed.; 16th. ed.; McGraw-Hill Professional: Maidenhead, 2004.

(42) Fanfair, D. D.; Korgel, B. A. *Chem. Mater.* **2007**, *19*, 4943–4948.

(43) Airoldi, C.; Silva, M. L. C. P.; Chagas, A. P. *J. Chem. Soc., Dalton Trans.* **1986**, 1913–1916.

(44) Patiño, R.; Campos, M.; Torres, L. A. *Inorg. Chem.* **2007**, *46*, 9332–9336.

CHAPTER 5 SIGNIFICANCE AND FUTURE SCOPE OF THE CURRENT RESEARCH: A CRITICAL ANALYSIS

5.1 BACKGROUND AND AIM OF THE RESEARCH

The synthesis of novel nanostructures and nanoassemblies is a primary focus in today’ s nano research. It has been shown that different semiconductor nanostructures in the form of dots, rods, wires and other hybrid nanoassemblies can be utilized for a wide range of applications such as – in solar cells, sensors, light emitting devices, drug delivery, bio-imaging, photodynamic therapy and many more in the field of electronics, medicine, physical- and bio- sciences, catalysis and engineering.

In this research, III-V (InP) and II-VI (CdSe, ZnSe) semiconductor based nanostructures and nanocomposites have been synthesized, characterized and their properties investigated. The main objective of this research was two-fold — (a) to investigate the potential of phosphido based single molecule precursors to indium phosphide (III-V) nanostructures, and (b) to develop novel hybrid nanoassemblies derived from CdSe or ZnSe (II-VI) quantum dots and nano-sized macrocycles, in this case suitably functionalized subphthalocyanines (SubPcs).

5.2 THE KEY FINDINGS

In the first part of this research, attempts have been made to use single-molecule precursors $[X_2In(\mu\text{-}PR_2)]_2$ (X = Me, CH_2Ph; R = CMe_3, $SiMe_3$) to generate nano-dimensional InP through thermal degradation. $[(PhCH_2)_2InP(SiMe_3)_2]_2$, was also reported as a new single molecule precursor. The important findings related to this part are —

i) Thermolysis of the di-tert-butyl precursors always led to In^0.

ii) The trimethylsilyl precursors formed In^0 only in presence of hexadecylamine, but in the absence of the amine could form InP nanoparticles.

iii) Thermolysis of $[(PhCH_2)_2InP(SiMe_3)_2]_2$ gave either InP nanoparticles or nanowires, depending on the presence or absence of stearic acid respectively.

iv) Thermolysis of $[(PhCH_2)_2InP(SiMe_3)_2]_2$ provided a simple and rapid method for the synthesis of InP nanowires, for the first time, without the need of any protic co-reagents or surfactants.

v) The wires were grown using the *hot injection technique* and their formation relied on the *SLS* mechanism.

vi) This research reported for the first time that the lengths of the nanowires can be conveniently controlled by adjusting only the injection temperature and wires could be grown at a temperature as low as 160 °C.

vii) The indium metal at the base of each wire, an obvious outcome of the SLS mechanism, can be easily removed under mild non-corrosive conditions without damaging the nanowires.

The second part of the thesis describes attempts to couple group II-VI (CdSe, ZnSe) quantum dots with subphthalocyanine (SubPc) to form hybrid nanoassemblies. The SubPc, which was chosen, carried pendant pyridyl moieties for coordination to the nanoparticle surfaces. The important findings of this part of the research are —

i) ZnSe did not show any ligand binding, whereas, CdSe formed a stable complex, with an association constant either larger than or comparable to previously reported values for other macrocycles.

ii) The QD : ligand ratio was found to be 1:1 and was determined by a number of independent experimental methods (UV, PL, NMR spectroscopy, quenching studies).

iii) The CdSe-SubPc formed an efficient donor-acceptor system in terms of photophysical properties, and energy flow within such systems was found to occur primarily through FRET mechanism from the QD (decreased luminescence) to the SubPc (increased emission).

5.3 RESEARCH SIGNIFICANCE AND SUCCESS

Some of the results of the current research are of great significance for some potential future applications. In its first part, this research reported for the first time the new precursor, $[(PhCH_2)_2InP(SiMe_3)_2]_2$, which can generate both nanoparticles and nanowires. This would allow one to generate preferentially the dot or wire structure from the same precursor in a fast and simple way. This precursor would also allow generating nanowires at a low temperature without using any other co-reactant or surfactant. This part of the research also demonstrates the means to control the lengths of the nanowires easily, which is not reported in the literature to-date.

In the second part of the research, it has been shown that subphthalocyanine can bind effectively with CdSe QDs in a ratio of QD : SubPc equal to 1:1. This 1:1 ratio is particularly of great significance w.r.t. bio-labeling and bio-imaging and has not been reported convincingly by any other earlier research. The SubPc molecules can also be functionalized further at its axial position (-OPh group) to generate hierarchical hybrid nanoassemblies.

5.4 FUTURE SCOPE OF THE RESEARCH

The current work opens up several new avenues for further research and has potential future applications. The InP nanowires formed here, can be employed for photovoltaic studies. The wires can be subjected to doping and tested for their electrical conductivity properties. The long wires are sufficiently long to qualify as interconnects and designing of solar cells. They can also be grafted onto conducting polymers for applications in plastic electronics. It would be interesting to find out the lowest temperature at which the wires could be grown with a supply of In^0 seeds from some external sources. The diameter of the wires can also be controlled by adding seeds of In^0 nanoparticles of desired diameter from outside. It would also be important to identify the thermal decomposition products of the dibenzyl precursors, which should throw light on the mechanism of the precursor decomposition. Studies could also be done in presence of light and check whether the decomposition temperature can be further lowered. InP nanowires can also be grown out of Au^0 seeds, so that they can be attached to suitable substrates via thiol linkages to form interesting structures.

In the second part of the research, the QD : SubPc ratio of 1:1 can be utilized for bio-labeling. One antibody per CdSe QD can be attached via a SubPc linker molecule, which would be very important for cell-imaging. The –OPh group in the SubPc molecule can also be suitably substituted and two different QDs can be joined together via SubPc linker, say through click chemistry. This would give rise to several exciting hybrid nanoassemblies.

THIS PAGE IS
INTENTIONALLY
LEFT BLANK